INFLUENCE OF PORE TYPES ON THE PETROPHYSICAL PROPERTIES OF CARBONATE ROCKS AND SEISMIC MONITORING OF CO_2 IN CARBONATES

A Thesis

by

ANA CRISTINA FIGUEROA

Submitted to the Office of Graduate and Professional Studies of
Texas A&M University
in partial fulfillment of the requirements for the degree of

MASTER OF SCIENCE

Chair of Committee,	Yuefeng Sun
Committee Members,	Michael Pope
	I. Yucel Akkutlu
Head of Department,	Michael Pope

August 2019

Major Subject: Geology

Copyright 2019 Ana Cristina Figueroa

ABSTRACT

Carbonate rocks are a significant component of future petroleum endeavors, but due to complex pore geometries display a lower average recovery factor in comparison to sandstone reservoirs. To recover residual oil and gas in these reservoirs, CO_2 enhanced oil recovery (EOR) is required. The theoretical results of this quantitative study are designed to provide a better understanding of the influence of carbonate rock pore types on seismic monitoring of CO_2 flooding in carbonate reservoirs.

This research shows how carbonate rock pore types influence the petrophysical properties, as rocks with the same porosity can have very different velocities. Rock physics models, like the Sun (2000) model, were used to quantify the carbonate rock pore types. The elastic parameter, frame flexibility factor, provide a structural representation of the pore. High frame flexibility factors correlate with rocks that have more grain coupling and contacts, such as intercrystalline and microporosity samples. Low frame flexibility factors relate to a rigid rock frame, present in cemented and moldic pore types.

CO_2 flooding causes a decrease in Vp and bulk modulus, the largest change occurring in microporous rocks. Average microporosity samples had about a -13% Vp change for CO_2 gas, whereas it was a -11% Vp change for CO_2 liquid. Of the petrophysical properties, the largest percent change was for the bulk modulus of microporosity pores, with a -32% change for CO_2 gas and -26% change for CO_2 liquid. CO_2 liquid flooding causes an increase in Vs due to the density effect. The CO_2 flooding effect percent changes were higher for CO_2 gas-saturated than for CO_2 liquid-saturated samples. Samples used had the same porosity of about 40%, as well as similar mineralogy, therefore the changes in pore types caused the changes in CO_2 flooding. For

CO_2 gas, the percent changes in the CO_2 flooding effect display a negative change for all properties except density and impedance, where the change was positive. The CO_2 flooding effect percent changes for CO_2 liquid, shows a negative change for all properties except Vs, where the change was positive. The changes that occur with CO_2 flooding are due to the density effect associated with the CO_2 phase changes.

The results of this thesis provide significant conclusions that could be used as a guide for future researches on time-lapse seismic monitoring of carbonate rocks following CO_2 sequestration. An effective rock physics model can better determine and aid in understanding the effects carbonate rock pore geometries have on seismic monitoring of CO_2 sequestration in carbonate rock reservoirs.

DEDICATION

I would like to dedicate this thesis to my beautiful daughter, Olivia, who provided me the motivation and love I needed to finish this research.

ACKNOWLEDGEMENTS

There are many people who have contributed to my education and supported me in achieving my goals. I would first like to thank Dr. Sun, for his support and patience during my research. I truly appreciate the kindness Dr. Sun has always shown me, and with his help I have improved greatly throughout my graduate career. I would also like to thank my committee members, Dr. Pope and Dr. Akkutlu, for their additional guidance, participation, and support throughout the course of this research.

I am so thankful for the friends and colleagues I met during my time at Texas A&M University, it made my time at A&M a great and truly treasured experience. I am especially thankful for the Department of Geology and Geophysics' faculty and staff, who have always treated me like family and always believe in me. Special thanks to Suzanne Rosser – one of my biggest supporters throughout my undergraduate and graduate career – I am extremely grateful and blessed to have crossed paths with you. Thanks to Trisha Fike for making graduate school less of an obstacle and always being there to help. Thank you to Cathy Bruton for the constant support I needed to get through graduate school.

Thanks to my mother and father for their continuous encouragement and love. This accomplishment would not have been possible without their unfailing support throughout the years and through the process of researching and writing this thesis. Thank you to my sisters, Paulina and Mariana, for always reminding me that I had a thesis to finish. Thank you to my best friend and "twin," Haley Gold, for always being there for me throughout the years. Thank you to my niece, Natalie, who always brings joy to any situation. Thank you to my extended family for their well wishes and prayers, especially my Abuela Maria Eugenia who constantly prays for me

to finish school. Thanks to my daughter, Olivia, whose smile and laughter was the motivation I needed to get through tough times. Lastly, I would like to thank God for blessing me with the friends, family, and educators who have helped me become who I am today.

CONTRIBUTORS AND FUNDING SOURCES

This work was supervised by a thesis committee consisting of advisor, Dr. Yuefeng Sun, Dr. Michael Pope of the Department of Geology and Geophysics, and Dr. I. Yucel Akkutlu of the Department of Petroleum Engineering.

The data analyzed was provided by Professor Yuefeng Sun. All work conducted for the thesis was completed by the student, under the advisement of Dr. Yuefeng Sun of the Department of Geology and Geophysics.

Graduate study was made possible in part by the Texas Aggie Graduate Grant from Texas A&M University, the Mr. and Mrs. W. Dustin Marshall ’75 Fellowship from the Berg-Hughes Center for 2017-2018, the UNOCAL Fellowship from the College of Geosciences for 2018-2019, the Graduate Scholarship from the Department of Geology and Geophysics for 2018-2019, and the Pregnant and Parenting Scholarship from the Pro-Life Aggies Organization for 2018-2019. Its content is solely the responsibility of the authors and do not necessarily represent the official views of the awarding offices.

NOMENCLATURE

Vp	P-Wave Velocity
Vs	S-Wave Velocity
P	Pressure
T	Time
ρ	Density
ρ_m	Solid Matrix Density
ρ_{fl}	Fluid Density
Ø	Porosity
K	Bulk Modulus
$\overline{K}$	Effective Frame Bulk Modulus
K_{fl}	Fluid Bulk Modulus
K_s	Solid Matrix Bulk Modulus
$K_Ø$	Pore Space Stiffness
K_{dry}	Dry Rock Bulk Modulus
K_m	Mineral Bulk Modulus
K_d	Normalized Bulk Modulus
K_{Gass}	Gassmann-Predicted Bulk Modulus
k	Ratio of Pore Space Stiffness Over Mineral Modulus
μ	Shear Modulus
μ_s	Solid Matrix Shear Modulus
f, f_μ	Frame Stiffness Factors

γ, γ_μ	Frame Flexibility Factors
c	Ratio of γ_μ / γ
V_f	Velocity in Saturated Fluid
V_m	Velocity in Rock Matrix
GBB	Great Bahamas Bank
EOR	Enhanced Oil Recovery

TABLE OF CONTENTS

Page

LIST OF FIGURES

Page

LIST OF TABLES

Page

1. INTRODUCTION

1.1 Motivation and Significance

Carbonate rocks are a significant component of future petroleum endeavors, as they account for approximately 60% of the world’s oil and 40% of the world’s gas reserves (Schlumberger, 2007). Carbonate rocks, however, display lower average recovery factor values of about 20-35% in comparison to sandstone reservoirs due to complex pore geometries in carbonate rocks (Mammadova, 2011). To recover oil in these reservoirs, advanced Enhanced Oil Recovery (EOR) techniques, like high pressure CO_2 injection to recover residual oil and gas, is required. This is prominent in the oil industry as nearly three quarters of hydrocarbons in place are not recoverable by conventional methods (Wang and Nur, 1989). EOR techniques also are crucial in keeping economical production rates for an effective exploration and recovery. This thesis focuses on the popular EOR technique, CO_2 sequestration, where residual oil and gas are recovered by a high-pressure injection of CO_2. The injected CO_2 responds to variations in rock pore type geometries, which is monitored through seismic imaging.

Petrophysical properties, such as porosity and permeability, of carbonate rocks are influenced by carbonate rock pore types and the changes in pore geometries. The heterogeneities in carbonate rock pore types make characterization of carbonate reservoir properties difficult. Thus, carbonate rocks require an accurate rock-physics model to make them predictable for oil and gas exploration. Using the mathematical models, Gassmann (1951) and Sun (2004) determined that porosity of carbonate rocks may be predicted using acoustic properties. Studying modern carbonates as an analog will aid in the understanding of individual pore geometries, as well as the understanding of known reservoirs such as the Permian Basin. This thesis addresses the effect of carbonate rock pore types on petrophysical properties and the influence of carbonate rock pore type variations on the seismic monitoring with carbon dioxide flooding, so as to predict variations in rock properties.

1.2 Importance

The following indicates the importance of this research:

1. Properly understand the geology of a carbonate reservoir through the study of carbonate rock pore types
2. Knowing carbonate rock pore types influence oil and gas production and recovery
3. Production data can be more accurately predicted for a company performing a CO_2 EOR
4. Utilizing a rock physics model to better understand variations in carbonate rock properties for creating an effective characterization of carbonate rocks and potential carbonate rock reservoirs.

1.3 Statement of Problem

Carbonate rock pore types are altered by chemical reactions and diagenesis that permanently change a carbonate reservoir, so it is vital to study the influence different fluids, like carbon dioxide, will have on carbonate rock pore types. This study investigates how petrophysical properties of carbonate rocks are influenced by carbonate rock pore types, and how the different pore types affect seismic monitoring of CO_2 sequestration of carbonate rocks. The heterogeneities in carbonate rock pore types make characterization of carbonate reservoir properties difficult. Thus, carbonate rocks require an accurate rock-physics model to make them predictable for oil and gas exploration. Using the mathematical models created by Gassmann

(1951) and Sun (2000), we may be able to determine a relation between CO_2 flooding, pore types in carbonate rocks, and variations in rock properties.

1.4 Research Objectives

The objective of this research will be to address the following:

1. How do carbonate rock pore types influence the petrophysical properties?
2. Can knowledge of carbonate rock pore types be used to predict seismic monitoring of CO_2 sequestration?
3. How can better carbonate rock pore type knowledge improve production with CO_2 EOR?

1.5 Previous Research Results

Several rock physics models were introduced focusing on acoustic properties in carbonate rocks. The correlation between velocity and pore size, as well as the study of problems associated with the elastic behavior of carbonate rocks was conducted by Hamilton et al. (1956). A qualitative rock physics model (Anselmetti and Eberli, 1993) related porosity and pore types to acoustic velocities in carbonate rocks, acknowledging the effect of porosity and pore types on variations of acoustic properties. Other previous studies on acoustic properties focus on siliciclastic rocks, which are not applicable in carbonate rocks.

The effect of CO_2 sequestration on the seismic properties of carbonate reservoir rocks was studied by Mammadova (2011), where Sun’s (2000) model was used to correlate variations in acoustic velocities to lithology, porosity, and pore types in carbonate reservoirs. The results of this study indicate that there was a decrease in the porosity of CO_2-saturated carbonate rocks as shear wave velocity increased. Mammadova successfully correlated Sun’s (2004) formation flexibility factor (γ) to the type of carbonate rock pore type, with a high formation flexibility factor (γ) value indicating a highly cemented pore with low porosity. A clear relationship between acoustic velocity and depositional environments was established, where shallow water carbonate rocks have higher velocities and velocity contrasts than deeper water carbonate rocks (Mammadova, 2011). Shallow water carbonate rocks having a higher content of metastable minerals and coarser grain sizes in shallow platform and reef deposits, further stimulating diagenetic processes. The research completed by Mammadova (2011) provided significant preliminary results that will be used as a guide for this research on time-lapse seismic monitoring of carbonate rocks following CO_2 injection at depth.

1.6 History of CO_2 Sequestration and Benefits

Laboratory research on the use of carbon dioxide to increase oil recovery started in the 1950s. A patent for an oil-recovery method with CO_2 was awarded in 1952 to Whorton and Brownscombe (Stalkup, 1978). In the early 1970s, Enhanced Oil Recovery (EOR) began after a gas processing facility in west Texas injected CO_2 into a nearby oil field to boost oil recovery. With the rising oil price in the 1970s, EOR techniques such as carbon dioxide miscible flooding became key methods for secondary recovery.

As a result, different CO_2 sequestration techniques and different injection processes were developed. Examples of techniques include a continuous injection of water and gas, alternating between water and gas, or injecting pure, supercritical CO_2. These techniques result in either a miscible flood (MMP) or an immiscible flood, dependent on pressure. The overall efficiency of CO_2 EOR was announced in 2005 by Secretary Samuel W. Bodman, as the Department of Energy (DOE)-funded CO_2 sequestration project was able to successfully double the oil field recovery rate – increasing production 5 MBO per day, as well as sequestering five million tons of carbon dioxide (Preston, et al., 2005).

Benefits of using CO_2 as the fluid injected into a reservoir include increased oil recovery, as well as the sequestration of the greenhouse gas, CO_2, as a means for reducing man-made CO_2 emissions. This is due to a large portion of the injected CO_2 remaining in place in depleted reservoirs, this is a low-cost way of permanently reducing greenhouse gas emissions.

2. AREA OF RESEARCH AND DATASET

2.1 Data Acquired

This research uses publicly available data from the Unda and Clino cores on the Great Bahamas Bank carbonate platform, that were collected by the Bahamas Drilling Project (Ginsburg, 2001). The Unda and Clino cores were drilled on the western flank of the Bahamas platform located 8.5 km apart from each other and reach depths of about 442 and 667 meters below seafloor, respectively. The western flank of the carbonate platform is a low-angle, prograding slope margin. The Unda core was drilled into mostly topsets whereas the Clino core was drilled into or through inclined foresets. The Unda well reaches Middle Miocene carbonate rocks (the oldest drilled sediments in the Great Bahama Bank), whereas the Clino well only reaches Late Miocene sediments. A total of 89 samples were collected from the two core borings, but only 46 samples will be used in this study with brief descriptions of their lithologies. Petrophysical data with lithological descriptions, as well as compressional-wave and shear-wave velocities of the samples, were collected and are included in the dataset (Anselmetti and Eberli, 1993).

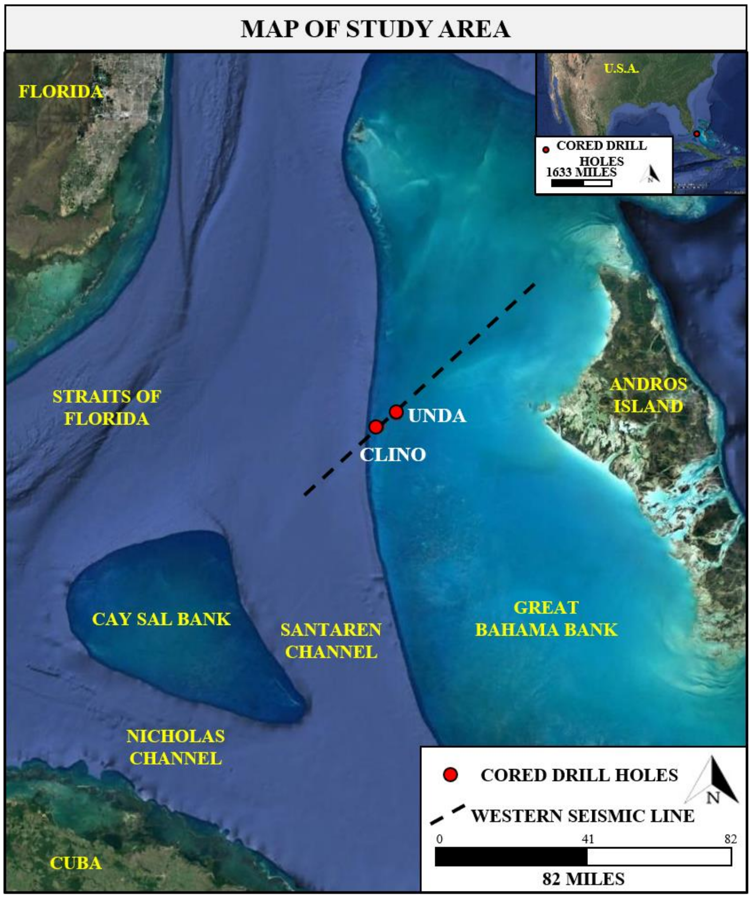

Figure 1. Location map of Clino and Unda cores in relation to Great Bahama Bank.

2.2 Methodology

This study integrates both geology and geophysics through the use of rock physics models. This is completed through the following methods:

1. Characterization and identification of different carbonate rock pore types based on 46 samples collected from the cores of Unda and Clino in the Great Bahamas Bank
2. Identifying elastic properties of pore geometries using rock physics models
3. Analysis of the influence of the carbonate rock pore types on CO_2 sequestration through seismic monitoring

By understanding the regional geologic background of the area to create qualitative and quantitative interpretations, these interpretations can be used to identify carbonate rock types and their influence on elastic properties. The application of rock physics models will be used to further quantify the carbonate rock pore types. The Sun model (2000) introduced the elastic parameter, known as frame flexibility, which provides a characterization of the internal pore structure and its relation to the elastic properties in carbonate rocks.

The main part of this study investigates how different carbonate rock pore types influence seismic monitoring of carbon dioxide. Using the Gassmann equation, the fluid substitution model is derived to estimate the elastic moduli of a rock with CO_2 flooding and compare that to an initially water-wet rock. This influence will be studied in synthetic seismic models, through the geophysical Hampson-Russell Software, that have undergone inversion to look at the differences in impedance values in relation to pore types and the geology of the research area. The measured and calculated P-wave velocities and densities are replaced in synthetic logs for specific samples, representative of that pore type. Previous studies on petrophysical properties of rocks focus on siliciclastic rocks, which are unlike complex carbonate pore types geometries creating a challenge for understanding carbonate rocks.

2.3 Regional Geology

The Great Bahamas Bank (GBB) is an isolated carbonate platform located in the Atlantic Ocean, southeast of Florida and northeast of Cuba. The various depositional environments on the GBB make it one of the most extensively studied areas in the world, as it is a modern analog for ancient isolated carbonate platforms. This area is comprised of Late Jurassic through Miocene carbonate rocks, which is appealing to petroleum geologists producing hydrocarbons from rocks of the same age and similar latitudes in areas such as southern United States, Mexico, and the Middle East (Meyerhoff and Hatten, 1974).

The precursor to the GBB isolated carbonate platform formed in warm, shallow water during the Late Jurassic through various dynamic processes. Repeated tectonic segmentation caused by the collision between the North American plate with Cuba involved rifting and reactivation of tectonic movements, followed by successive pulsed progradation to form the modern Great Bahamas Bank (Eberli and Ginsburg, 1989). Core studies on the Great Bahamas Bank and seismic data indicate progradation on the banks since the Miocene. In the Late Cretaceous, the Great Bahamas Banks consisted of two small banks separated by the Straits of Andros. The Bahamian basement is relatively unknown, due to a lack of deep boreholes ever reaching the true crystalline basement. However, it is hypothesized that the basement is similar in composition to the basement recovered from both Cuba and Florida, which is igneous and metamorphic in origin (Carew and Mylroie, 1997).

During the early Tertiary, the carbonate banks grew vertically with some slight progradation on the western portion of Andros Bank (Eberli and Ginsburg, 1989). In the Middle Miocene, progradation on the western margins filled the Bimini Embayment. A combination of basinal aggradation and bank-margin progradation merged the two smaller banks together, creating the modern GBB. The geometries of the prograding sequences indicate that the pulses of progradation were sea-level controlled, although the progradation of both straits occurred at different times (Eberli and Ginsburg, 1989).

The Bahamas consist of an archipelago of scattered islands on two major banks, the Little Bahama Bank and the GBB, separated by Northeast and Northwest Providence Channels. Two deep troughs, the Tongue of the Ocean and Exuma Sound, surround the GBB (Carew and

Mylroie, 1997). The GBB carbonate platform is rimmed by either coral reefs, ooid shoals, or coralgal sands where the water current is strong. The inner area of the Bahamas platform consists of pelletal or lime muds where water current is calmer (Harris, 1986). The elevated topography on most major islands on GBB consist of eolianite dune ridges (Carew and Mylroie, 1997).

The western flank (Figure 2) of the GBB is a low-angle, prograding carbonate platform due to sea-level fluctuations (Melim et al, 2001). Various methods were used to study the subsurface geology of the Bahamas, including seismic methods and scientific drilling. During the Bahamas Drilling Project, the Unda and Clino cores were drilled on the western portion of the GBB and record its depositional successions there (Eberli et al., 1997). In the Clino core, three principal sections are determined: (1) seven units capped by a subaerial exposure horizon located in the upper platform section, (2) reefal unit with upward progression, and (3) slope sediments consisting of fine-grained skeletal and non-skeletal grains, with intervals of coarse-grained skeletal sands (Melim et al, 2001). The Clino core penetrated 677.27 meters below the mud pit (bmp), whereas Unda penetrated 452.94 meters bmp. The Unda core (Figure 2) consists of three successions of alternating shallow-water platform and reefal deposits with coarse sand-sized deeper water slope deposits (Melim et al, 2001).

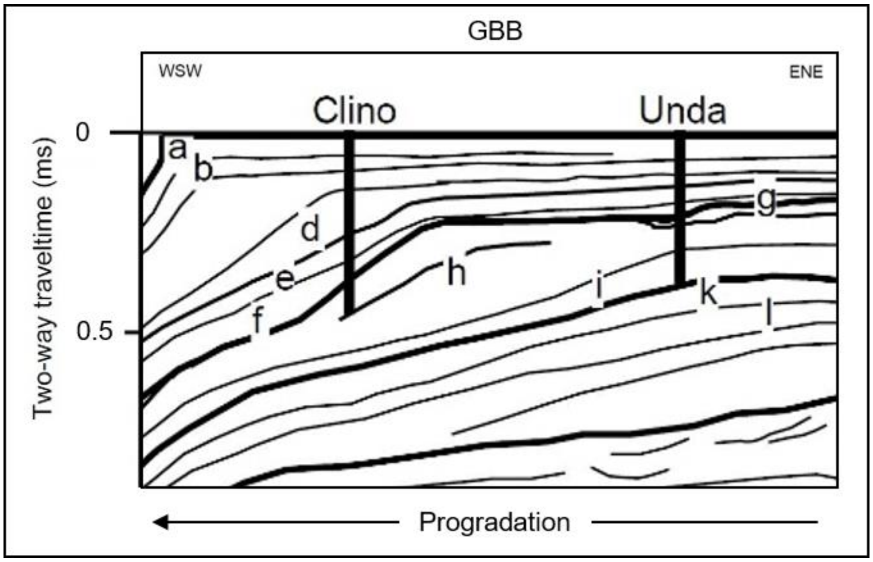

Figure 2. Seismic line with interpreted seismic line sequences – Clino and Unda cores penetrate the western prograding margin of the Northwest Great Bahamas Bank (modified from Eberli et al., 1997).

3. GEOLOGICAL ANALYSIS OF ACOUSTIC PROPERTIES

3.1 Introduction

Each of the 46 core sample descriptions from the Clino and Unda cores include: depth in meters, porosity, permeability in millidarcies, percentage of calcite composition, percentage of aragonite composition, percentage of dolomite composition, P-wave velocity (Vp), S-wave velocity (Vs), identified carbonate pore types, and notes on dolomitization. Well logs for the Unda and Clino cores also were collected from the previous Bahamas Drilling Project.

The Clino and Unda cores were taken from the prograding section of the western platform margin. The cores and seismic data show that pulse progradation occurred as laterally stacked sequences, controlled by sea-level changes. Periods of rapid sea level rise and possible backstepping of platform and reef deposits, are recorded by the intervals of deeper-water sediments (Anselmetti and Eberli, 1993).

The top of the Unda core with the top of the section being Pleistocene and the bottom being Middle Miocene (Figure 3). The Unda core is located 10 km west of the modern platform edge and is characterized by three successions of reef-to-platform, shallow-water deposits. The Clino core is located 8.5 km west-southwest of the Unda core and characterized by a single interval of shallow-water reef-platform sediments overlying a thick succession of slope sediments. The Clino core's top is Pleistocene and its bottom section is Late Miocene. Four different pore types are identified in the Bahamas dataset, including: cement, intercrystalline, microporosity or mud, and moldic pores.

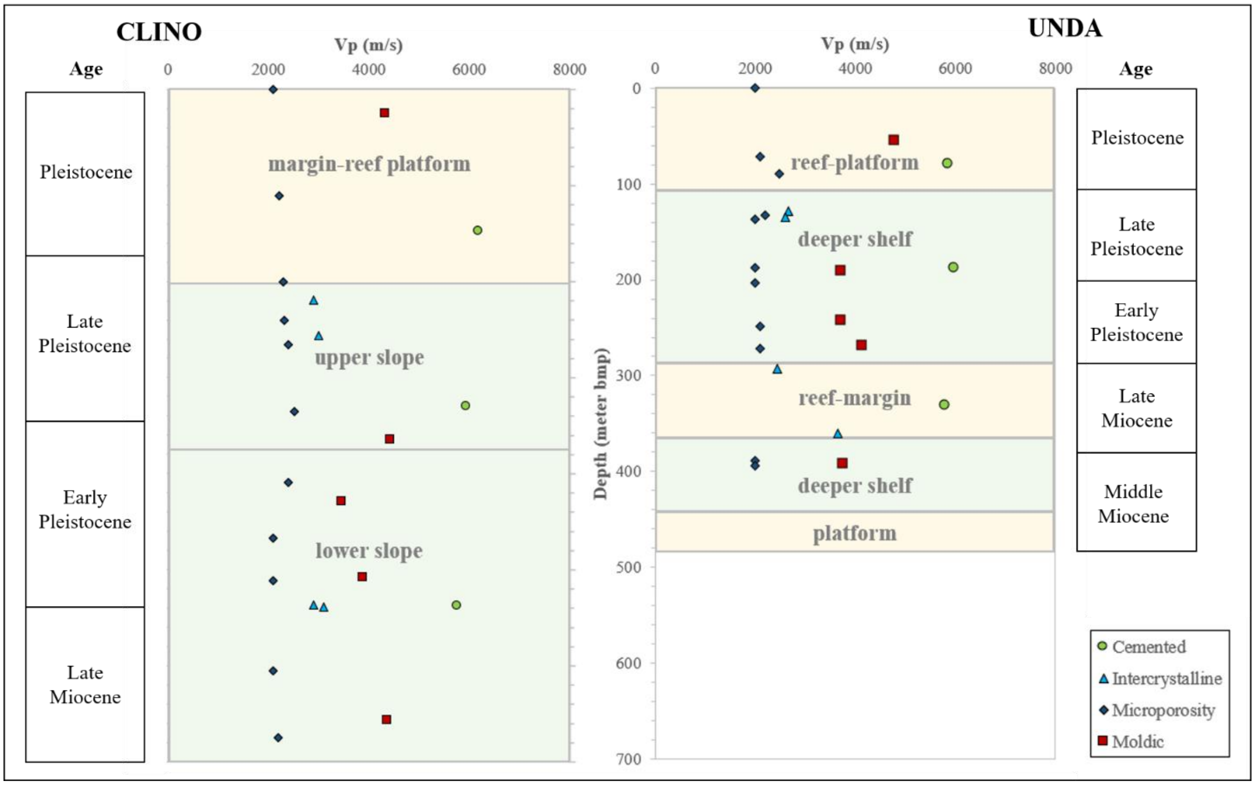

Figure 3. Vp with depth, depositional environment, and age with pore types identified for Clino and Unda cores (modified from Anselmetti and Eberli, 1993).

3.2 Mineralogy Analysis

The mineral composition of the Bahamian samples consists of varying proportions of high-Mg calcite, aragonite, and dolomite, all of which have very similar physical properties. There are four pore types identified in these samples: 1) cemented, 2) intercrystalline, 3) microporous, and 4) moldic pores. Utilizing the ternary diagram of the mineralogy of the samples (Figure 4) generally samples with a higher percentage of dolomite consisted of intercrystalline pores and samples with a higher percentage of aragonite had more microporosity pores. Overall, the data shows limited variability in mineralogy (Figure 4) and there is not a strong relationship between mineralogy of the samples and their pore type.

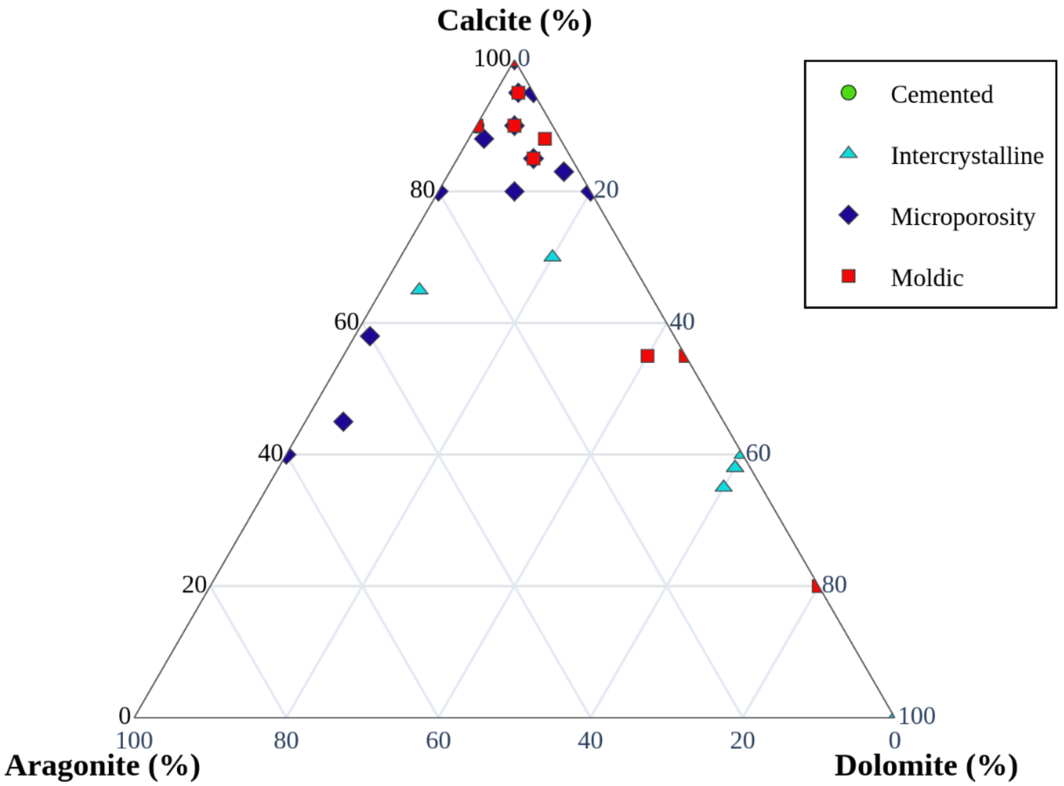

Figure 4. The variations in mineralogy in a ternary plot of aragonite, dolomite, and calcite showing the relative compositions of corresponding carbonate pore types of the 46 samples from the Unda and Clino cores located in the GBB.

Samples comprised of the same mineralogical composition (Table 1) from the same Unda core have very different pore types and acoustic wave velocities. Unlike siliciclastic rocks, carbonate rocks are less influenced by the mineral content of the rock and therefore the mineralogy of carbonate rocks do not cause large velocity contrasts like in siliciclastic rocks (Anselmetti and Eberli, 1993). This is shown with the two rock samples from the Unda core that are both compose of 100% calcite. The Unda core sample at 187 meters has a Vp of 5953 m/s and Vs of 3187 m/s, whereas the sample from the same well at 72 meters has a Vp of 2000 m/s and Vs of 1000 m/s. The sample with the higher velocity is a cemented calcite with a total porosity of 14% and the second sample has abundant micropores of calcite with a total porosity of 46%.

Depth (m)	Porosity	Mineralogy	Vp (m/s)	Vs (m/s)	Pore Type
78	14%	100% Calcite	5818	2930	Cemented
187	14%	100% Calcite	5953	3187	Cemented
72	46%	100% Calcite	2000	1000	Microporosity
90	46%	100% Calcite	2010	1050	Microporosity
54	32%	100% Calcite	4755	2186	Moldic

Table 1. Samples from the Unda core with the same 100% calcite mineralogy, and different velocities and pore types.

Therefore, the mineralogy does not correlate with pore type or velocity of the samples and has little influence on variations in acoustic velocity. Mineralogy should only be taken into account when discussing the possibility of diagenesis.

3.3 Velocity Analysis

For the 46 samples analyzed in this thesis, both the compressional wave velocity (Vp) and shear wave velocity (Vs) were measured at 10 MPa confining pressure and 2 MPa pore fluid pressure (Anselmetti and Eberli, 1993). The resulting effective pressure of 8 MPa was appropriate for receiving good signal responses without damaging the rocks (Anselmetti and Eberli, 1993). The Clino and Unda cores were taken from the prograding section of the platform margin. The cores and seismic show pulsed progradation occurred as laterally stacked sequences, controlled by sea-level changes (Eberli and Ginsburg, 1989).

The measured velocities of these samples were at an effective pressure of 8 MPa with P-wave velocity ranging from 2000 to 6200 m/s (an average Vp of 4100 m/s) and S-wave velocity ranging from 910 to 3300 m/s (an average Vs of 2105 m/s). Comparing the Unda and Clino cores, the velocity averages (for both Vp and Vs) are higher for the Unda core due to the penetration of three separate higher-velocity shallow water successions in the Unda core, unlike the Clino core which only perforated one shallow-water deposit (Mammadova, 2011).

There is no relationship between depth/age and velocity trends for the Clino and Unda cores. There is a correlation between depositional environments and velocity distributions, with higher velocities occurring for shallow-water platform deposits than deeper-water deposits. This is due to diagenetic alterations taking place at shallow depths faster than compaction (Anselmetti and Eberli, 1993). This is understood as the varied depositional environments have different lithologies, therefore affecting the responses to diagenetic alterations. Knowing shallow water sediments are coarser than deep water sediments, rapid diagenetic alterations occur in shallow water units because coarse grains allow higher fluid flow and higher concentrations of metastable minerals, like aragonite, during deposition. The opposite is true for deep water sediments, as deep-water units undergo less diagenetic alterations and have lower-velocity zones (Mammadova, 2011).

As mentioned earlier, the variations in mineralogy do not influence the acoustic velocities in carbonate rocks. Porosity is the main factor controlling acoustic wave velocities, but carbonate rocks with the same porosity can have different velocities due to the geometries of the pore types (Figure 5). This velocity-porosity crossplot displays an inverse correlation, where an increase in porosity creates a decrease in Vp and Vs. Large variations occur at porosities greater than 30%, where values stray above the best-fit curves.

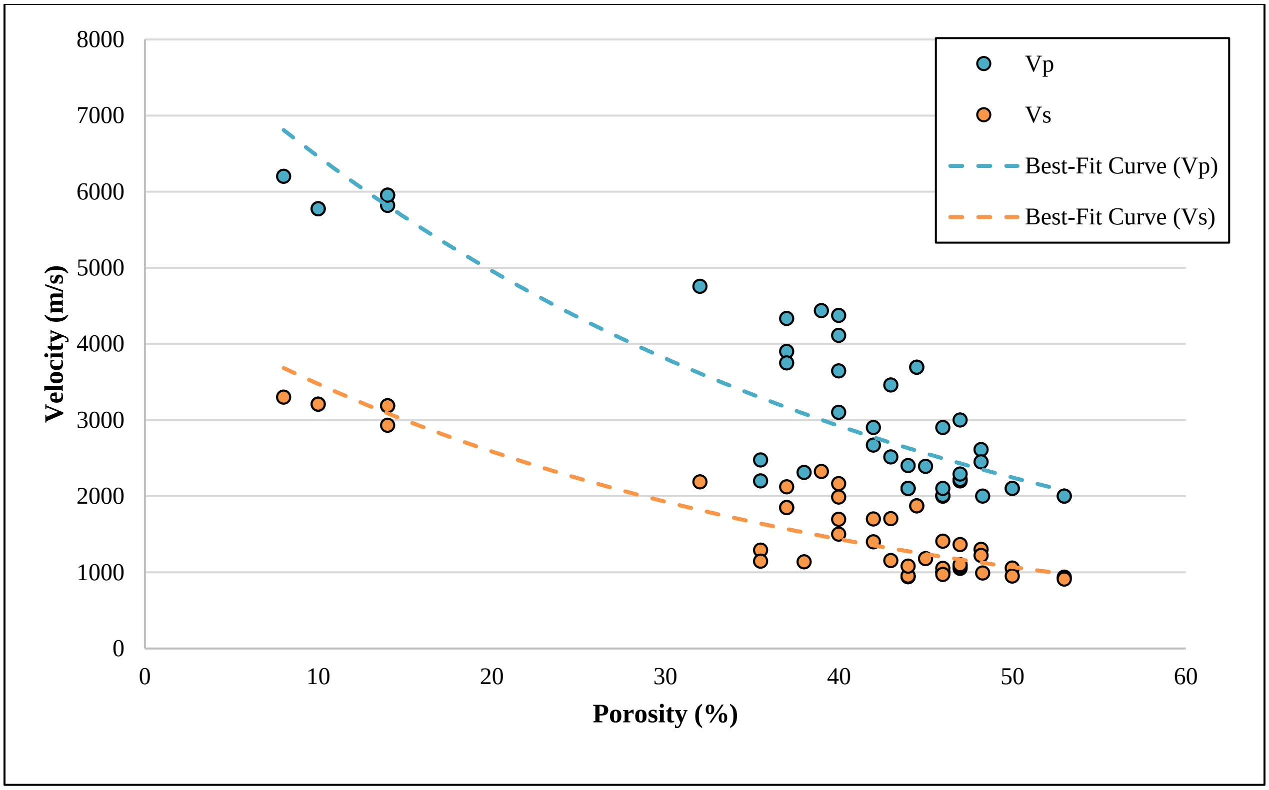

Figure 5. Porosity versus velocity for the Bahamas dataset, where Vp and Vs depict an inverse correlation with increasing porosity. There is a large scatter around the exponential best-fit trendline with higher porosities.

A "time-average formula" is used as a reference curve providing a linear relationship between velocity and porosity (Wyllie, 1958). This equation is:

$$\frac{1}{V} = \frac{\emptyset}{V_F} + \frac{1-\emptyset}{V_M} \tag{3-1}$$

where V is the velocity measured, V_F is the velocity in saturating liquid, V_M is the velocity in rock matrix, and $\emptyset$ is the volumetric porosity. Wyllie's equation has been used for years due to its simplicity, but the comparison of the measured P-wave velocity to Wyllie's theoretical equation shows underestimated velocities for the Bahamian carbonate rocks (Figure 6).

The velocity-porosity diagram (Figure 6) shows that cemented pore types has having high velocities with low porosities, whereas the microporosity pores have low P-wave velocities and generally high porosities. This depicts the overall negative trend that as porosity increases, the P-wave velocity decreases for the pore types. Looking at the individual pore types, moldic pores have a positive departure from the general trend, whereas intercrystalline and microporosity pores show a negative trend due to their relatively low velocities. Variations in acoustic velocities must take pore geometries into account for carbonate rocks.

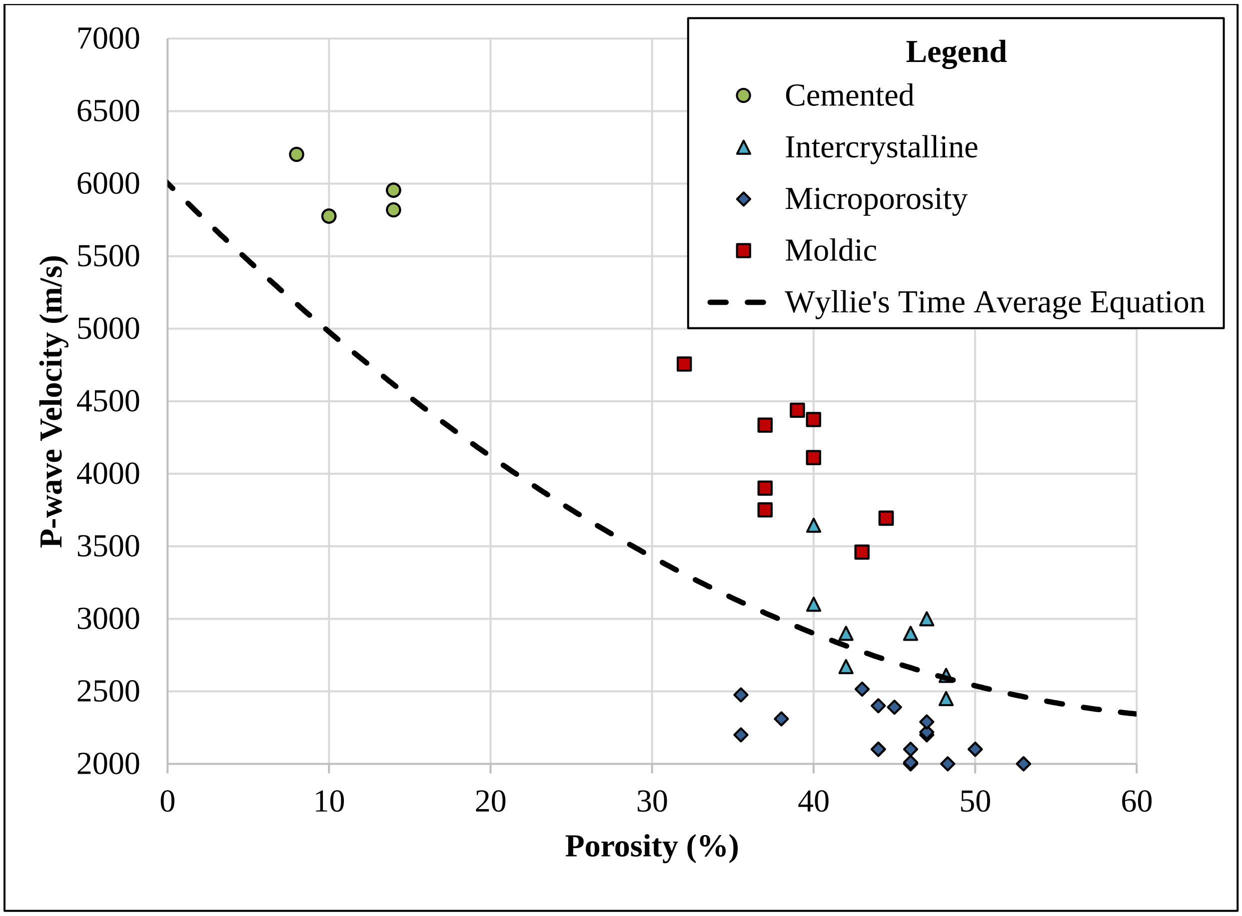

Figure 6. Porosity-velocity crossplot of all four pore types (cemented, intercrystalline, microporosity, and moldic) with Wyllie’s time average equation line (dashed line).

3.4 Porosity and Pore Types

Pore and pore systems in carbonate rocks are complex, both physically and in original development or genetically (Choquette and Pray, 1970). Data collected from the Unda and Clino cores show total plug porosities range from 8% to 53%. There are four different pore types that have been identified in this thesis: (1) cemented, (2) intercrystalline, (3) microporosity, and (4) moldic. Higher porosities occur in skeletal grainstone and packstone beds, except for intervals that are highly cemented (Mammadova, 2011). Intervals with higher concentrations of dolomite have porosities between 40-50%. Moldic pores have a total porosity ranging between 30% and 45%. Pore types with the same porosity and similar mineralogy have different velocities due to pore types, as depicted in Table 2. The samples in Table 2 will be used for modeling fluid substitutions in seismic monitoring in later chapters.

Sample	Depth (m)	Porosity	Vp (m/s)	Vs (m/s)	Pore Type
A	133	46%	2200	1145.83	Microporosity
B	203	53%	2000	990	Microporosity
C	268	40%	4110	2163	Moldic
D	293	40%	2450	1220	Intercrystalline
E	365	39%	4436	2323	Moldic
F	467	38%	2100	941.704	Microporosity
G	536	40%	2900	1407.77	Intercrystalline
H	657	40%	4373	1987	Moldic
I	675	44%	2200	1050	Microporosity

Table 2. Different pore types for porosity around 40%, with different velocities associated. Samples provided alphabetical letter based on depth, with A starting with the lowest depth and I the highest depth.

The pore types in the Clino and Unda core samples were originally classified by Anselmetti and Eberli (1993) using the Choquette and Pray (1970) classification of pore types. The pores in the Clino and Unda cores are both primary and secondary pore types, which is characterized by the time of porosity formation. For this thesis, primary pore types include microporosity and cemented pores, whereas secondary pore types are moldic and intercrystalline pores.

3.4.1 Cemented Pore Types

Highly cemented, low porosity pore types have plug porosities of 8-14% and are located in upper slope and reef-platform intervals of Clino and Unda cores. These packstone to grainstone sediments often are partially filled with blocky calcite cements (Figure 7), sometimes sealing the primary porosity completely (Melim et al, 2001).

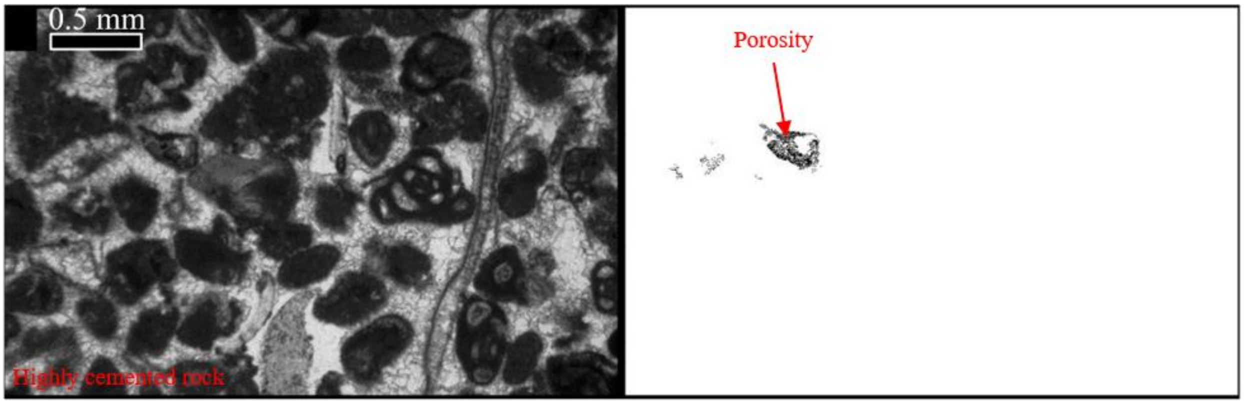

Figure 7. Left: Photomicrograph of a sample from the Unda drill hole at 358 meters bmp (below mud pit) with low-porosity cemented lithology and a plug porosity of 3%. The mainly skeletal grainstone is cemented with a blocky calcite that almost completely fills the former interparticle pore space. Right: Binary pore image from image analyses (porosity = black, solid phase = white) (modified from Anselmetti and Eberli, 1999).

The velocity-porosity diagram (Figure 8) of cemented pores forms a cluster above the upper end of the time-average equation trendline. These cemented pores have high velocities and low porosities.

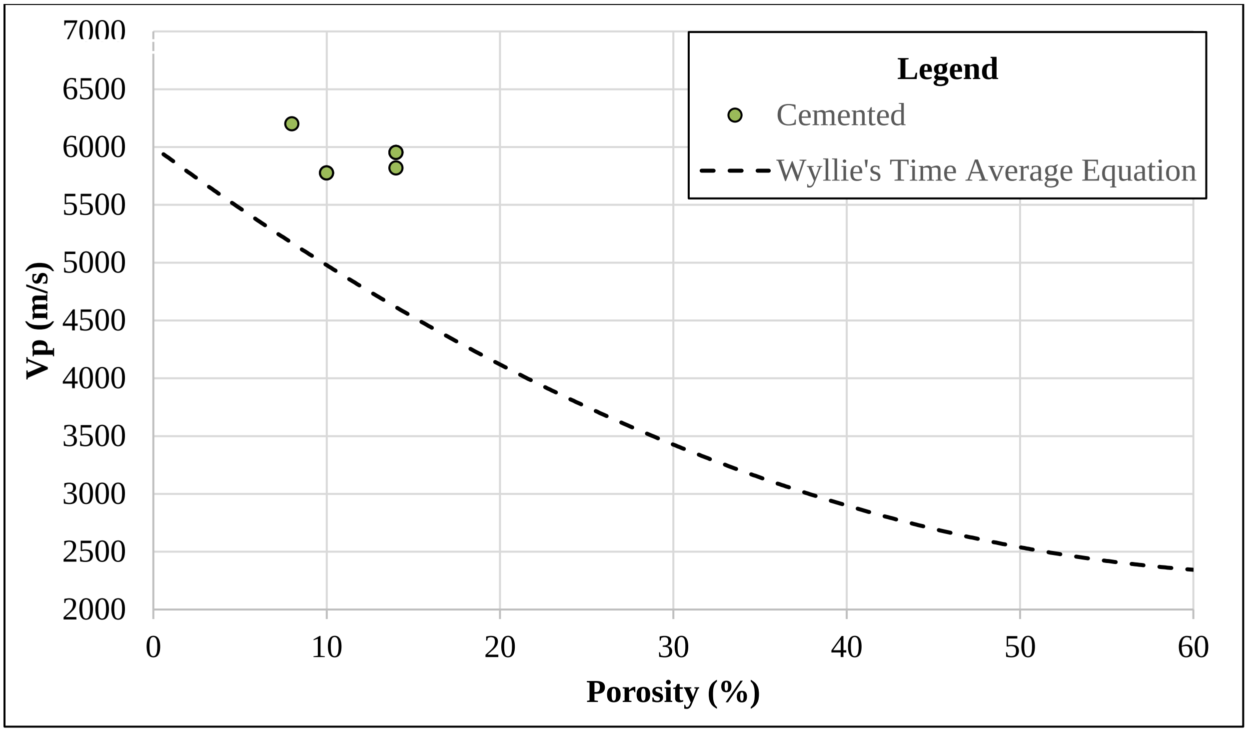

Figure 8. Velocity-porosity graph of highly cemented, low porosity carbonate rocks, in relation to Wyllie's time-average equation trendline.

3.4.2 Intercrystalline Pore Types

Intercrystalline porosity has plug porosities of 40-48.2% and it occurs in several intervals of the Clino and Unda cores. Intercrystalline pores occur in Clino between 530 and 580 meters, and in Unda between 250 and 350 meters (Melim et al, 2001). This porosity occurs through the dolomitization process (Figure 9), where minerals are crystallized to form dolomite rhombohedra from original skeletal-peloidal grainstone (Mammadova, 2011).

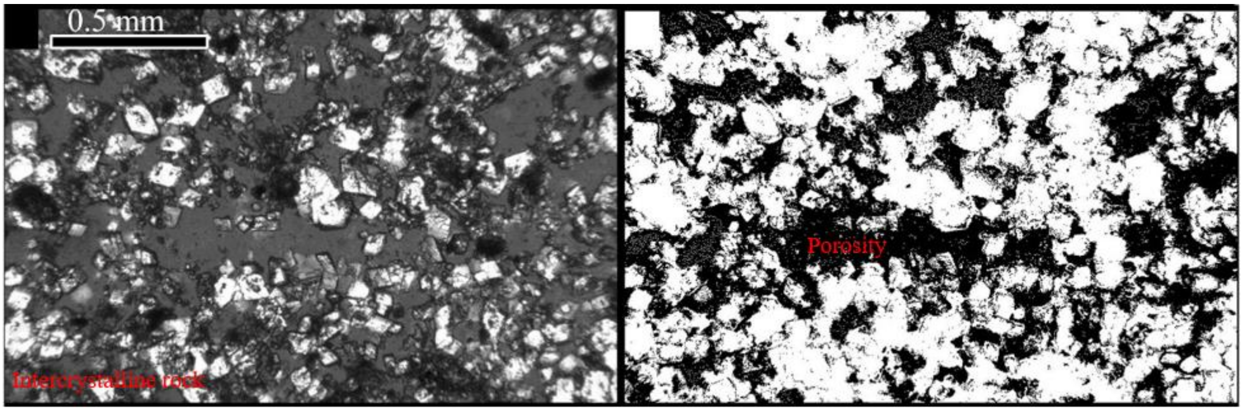

Figure 9. Left: Photomicrograph of a sample from the Unda drill hole at 286 meters bmp (below mud pit) with intercrystalline porosity and a plug porosity of 49%. The sediment is completely altered to microsucrosic dolomite (100% dolomite) from skeletal-peloidal grainstone. Right: Binary pore image from image analyses (porosity = black, solid phase = white) (modified from Anselmetti and Eberli, 1999).

The velocity-porosity diagram (Figure 10) of intercrystalline pores forms a cluster around the lower end of the time-average equation trendline. These intercrystalline pores have low velocities with high porosities.

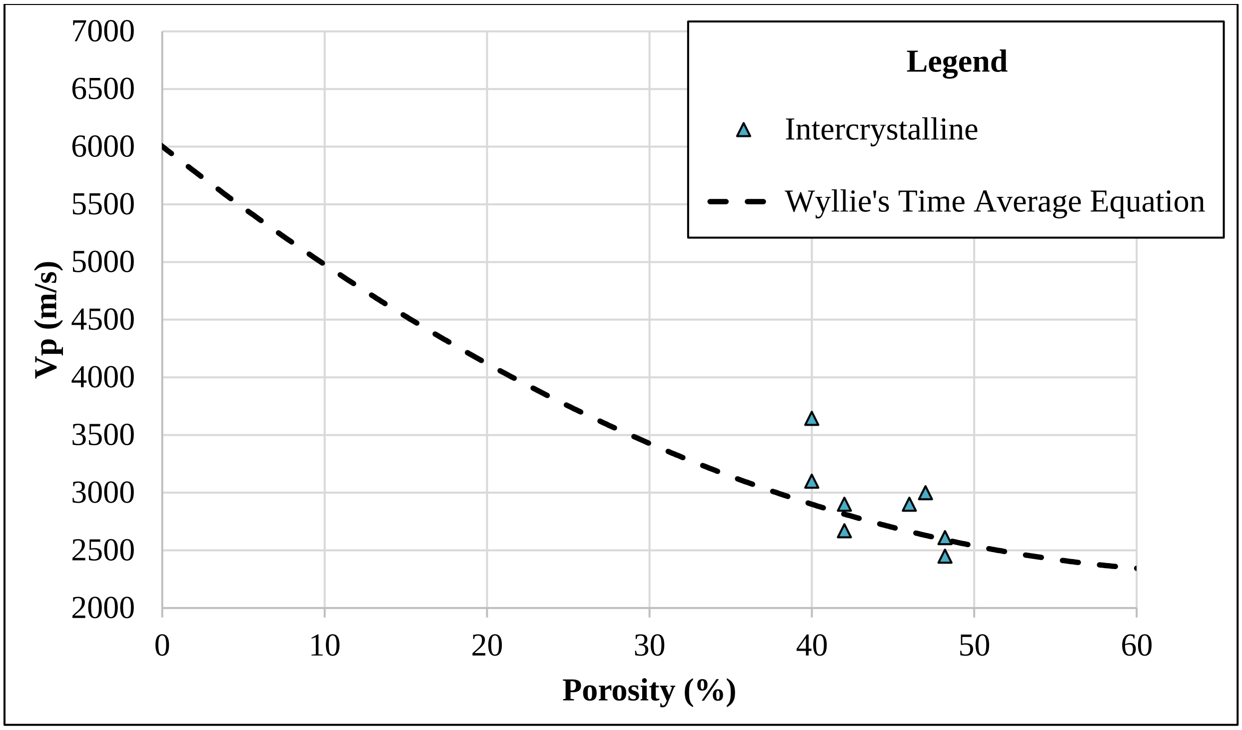

Figure 10. Velocity-porosity graph of intercrystalline carbonate rocks, in relation to Wyllie's time-average equation trendline.

3.4.3 Microporosity Pore Types

Microporosity pore types have plug porosities of 35.5-53% and occur in intervals of Clino and Unda cores containing a high percentage of lime mud (micrite). This pore type is confined to slope intervals in the Clino core, although it occurs in both the Clino and Unda core. These micropores are less than 10 µm in size and are concentrated carbonate mud (Mammadova, 2011).

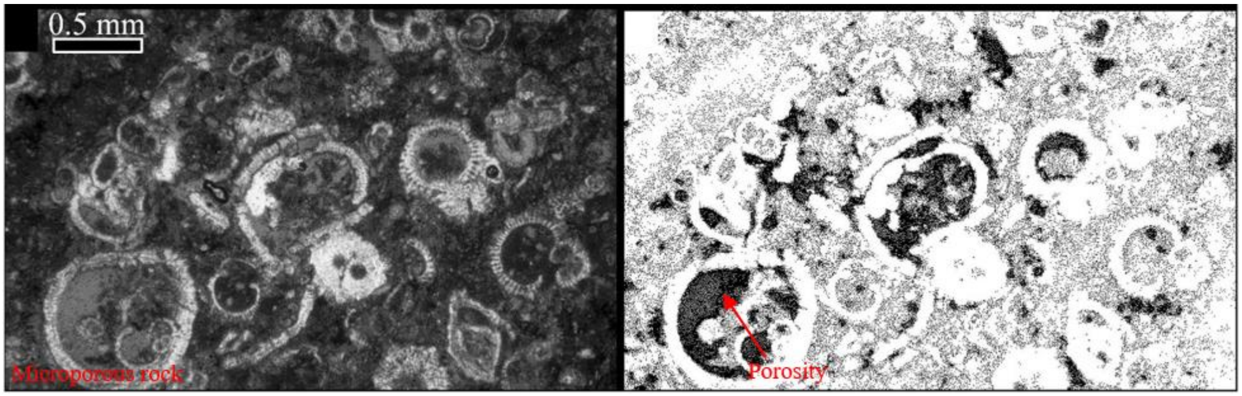

Figure 11. Left: Photomicrograph of a sample from the Clino drill hole at 510 meters bmp (below mud pit) with high microporosity and a plug porosity of 35%. The slope deposit is rich in globigerinids (foraminiferans comprised of marine plankton) and micritic (lime mud) matrix, has almost no diagenetic alterations, and little compaction visible. Right: Binary pore image from image analyses (porosity = black, solid phase = white) (modified from Anselmetti and Eberli, 1999).

The velocity-porosity diagram (Figure 12) of microporosity pores is similar to intercrystalline pore types, where the values form a cluster near the lower end of the time-average equation trendline; however, all of the microporosity values are below the trendline. These microporosity pores have negative trend where decreasing velocity correlates with increasing porosity, as this pore type has low velocities with high porosities.

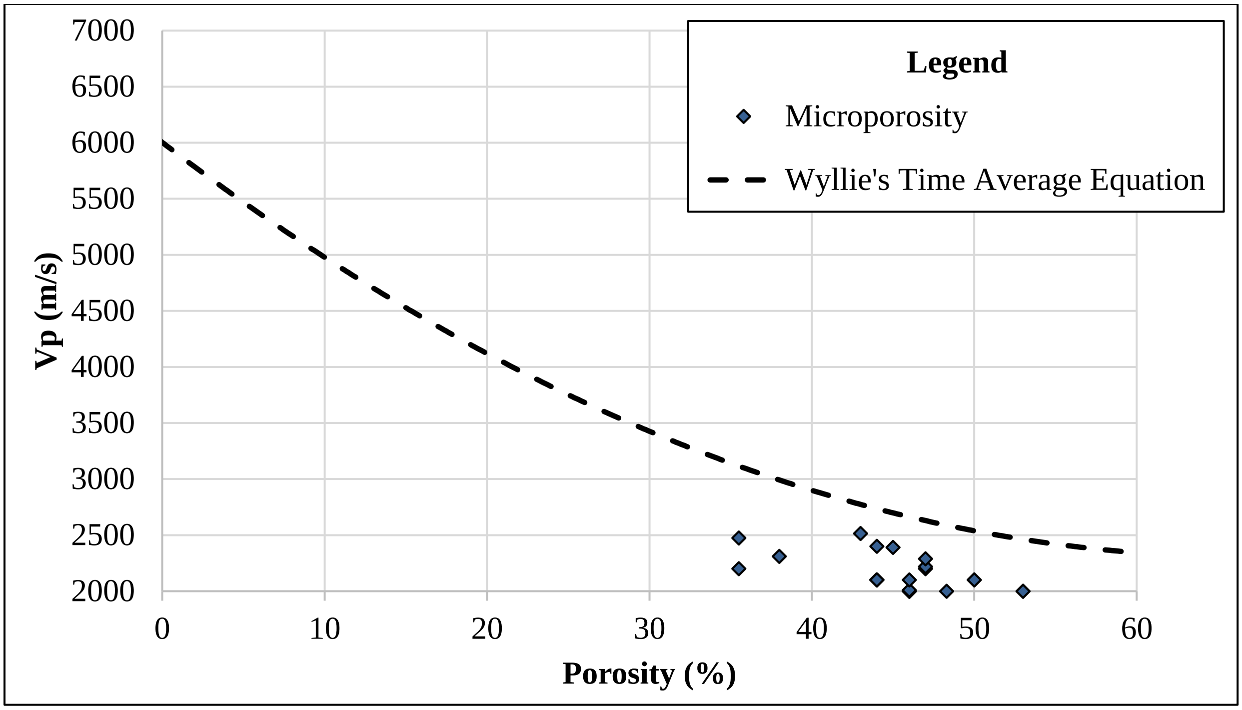

Figure 12. Velocity-porosity graph of microporosity carbonate rocks, in relation to Wyllie's time-average equation trendline.

3.4.4 Moldic Pore Types

Moldic pore types have plug porosities of 32-44.5% and permeability variations due to pore connectivity. This porosity is a result of the dissolution of metastable mineral grains, like aragonite and high-Mg calcite, and can occur at any time during the cementation of the interparticle pore space (Anselmetti and Eberli, 1993). Moldic porosity is the most common pore type throughout the Clino and Unda cores (Melim et al, 2001). In the shallow-water facies, moldic pores include corals, bivalves, gastropods, *Halimeda* sp., peloids, and ooids. Deep-water facies include rounded moldic pores interpreted to have been aragonitic peloids and angular pores that were skeletal fragments (Melim et al, 2001).

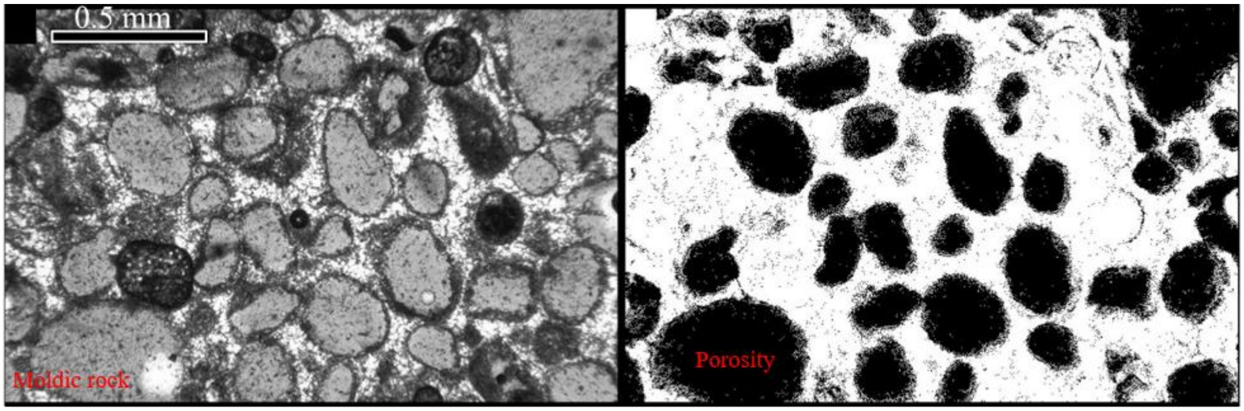

Figure 13. Left: Photomicrograph of a sample from the Unda drill hole at 65 meters bmp (below mud pit) with moldic porosity and a plug porosity of 37%. All components of this grainstone were dissolved during and after cementation of the interparticle pore space. Right: Binary pore image from image analyses (porosity = black, solid phase = white) (modified from Anselmetti and Eberli, 1999).

The velocity-porosity diagram (Figure 14) of moldic pores forms a cluster above the time-average equation trendline. Moldic pores have a positive departure from the general trend, unlike intercrystalline and microporosity pores that show a negative trend due to their relatively low velocities. These moldic pores are generally around the 40% porosity value with differing velocities.

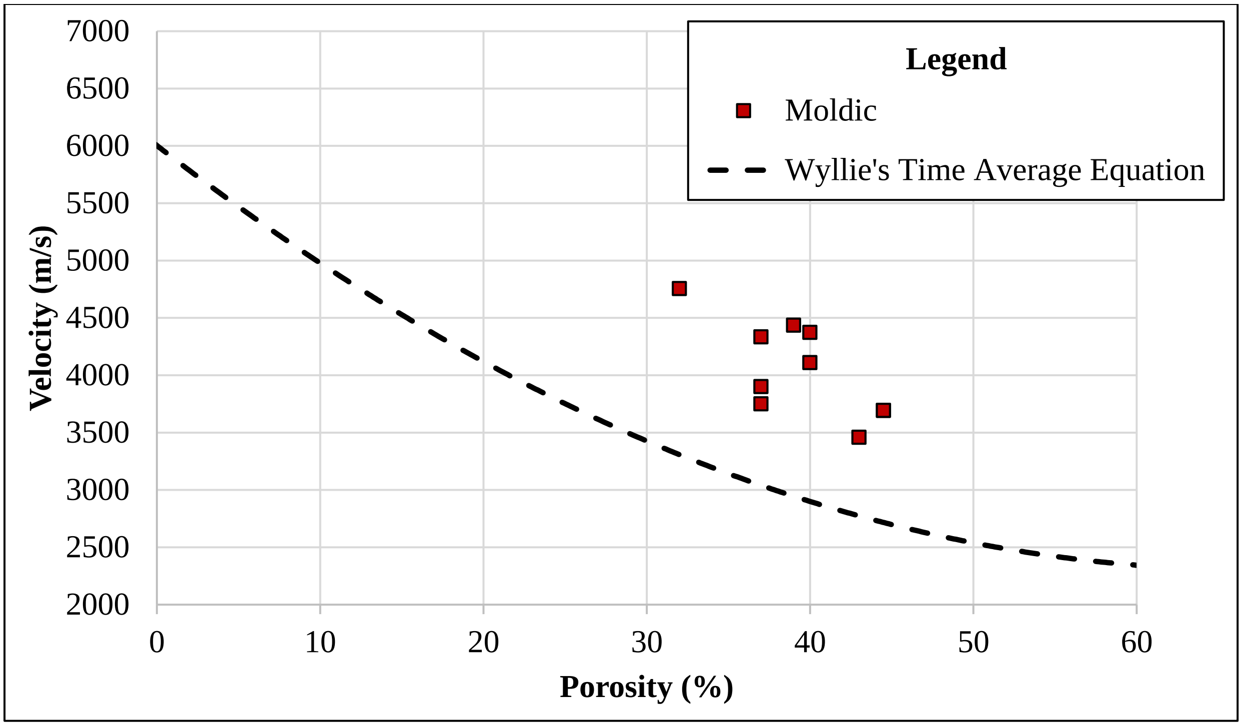

Figure 14. Velocity-porosity graph of moldic carbonate rocks, in relation to Wyllie's time-average equation trendline.

3.5 Permeability and Density

In carbonate rocks, permeability is a function of grain size and pore type (Melim et al, 2001). The complex heterogeneity in carbonate rocks, caused by the variability of depositional patterns and variety of diagenetic changes, affects the distribution and nature of pore types, which in turn affects the permeability (Melim et al, 2001). Pore geometries defined by the pore type, pore size, and pore connectivity, define the pore space available for fluid flow. The measurement of the rock's ability to transmit fluids is known as permeability.

Permeability was provided for all 46 samples and ranges from 0.0001 to 5000 millidarcies (mD). The logarithmic plot of permeabilities versus porosity (Figure 15) shows a general positive correlation. The highest permeabilities are related to intercrystalline pores, whereas low permeabilities correspond to cemented pores. Lower permeabilities also occur in samples with microporosity, despite their high porosities. Some moldic pores can have low permeability, despite high porosity, due to a lack of pore connectivity. Permeability in carbonate rocks is a function of pore size and connectivity, not porosity.

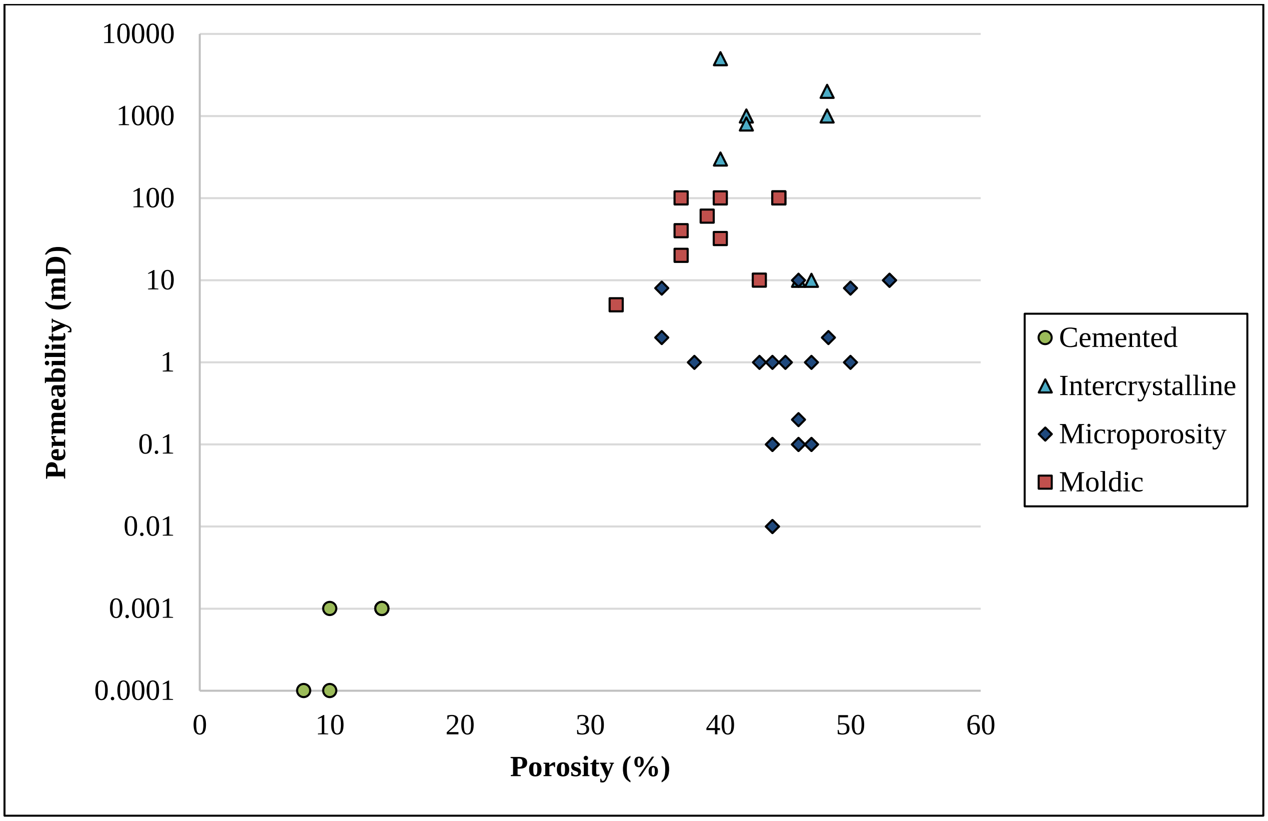

Figure 15. Logarithmic plot of permeability with porosity showing a positive correlation.

After coring, both cores were logged with downhole tools to collect density measurements, as well as other property measurements. Density was provided for all 46 samples and ranges from 1.84 to 2.65 grams per cubic centimeter (g/cc or g/cm^3). The plot of porosity versus measured density shows a general negative correlation (Figure 16). The highest densities have the greater abundance of the cemented pores, whereas the lowest densities correspond to abundant microporosity. In general, density increases and porosity decreases in relation to depth and pressure increasing. This is because as pressure increases with depth and the sediments are compacted as the grains will shift to reach a denser packing. Additionally, diagenetic processes, such as cementation, work to fill the pore space and increase density.

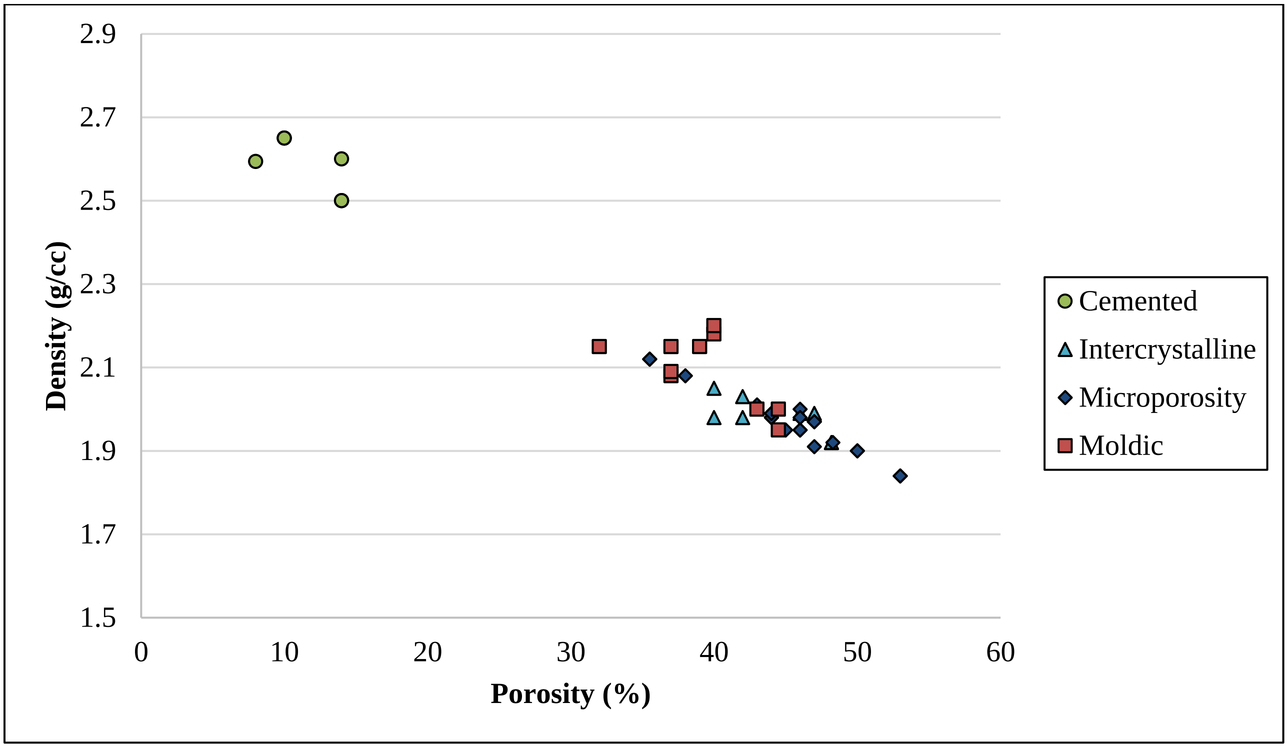

Figure 16. Porosity versus density for the carbonate pore types showing a negative correlation.

3.6 Elastic Properties

Seismic waves include the primary wave or pressure wave (P-wave), and the secondary wave or shear wave (S-wave). These waves have their own velocities (Vp for P-wave or compressional velocity and Vs for S-wave or shear velocity), which is dependent on the bulk (K) and shear (μ) moduli properties. The bulk modulus is the rock's ability to resist changes in volume, whereas the shear modulus is the rock's ability to resist changes in shape – both are in the units gigapascal (GPa).

The equations for the Vp and Vs in relation to elastic properties are below:

$$V_p = \sqrt{\frac{K + \frac{4}{3}\mu}{\rho}} \tag{3-2}$$

and,

$$V_s = \sqrt{\frac{\mu}{\rho}} \tag{3-3}$$

where ρ is the density (g/cm^3), K is the bulk modulus, μ is the shear modulus, and V is the velocity (m/s).

The bulk and shear moduli for the 46 samples were calculated using the Vp and Vs (Equations 3.2 and 3.3, and the densities reported by Anselmetti and Eberli (1993) (Appendix B). The equations below are modified from Equations 3.2 and 3.3 to find the elastic moduli:

$$\mu = \rho {V_s}^2 \tag{3-4}$$

and,

$$K = \rho \left({V_p}^2 - \left(\frac{4}{3}\right) {V_s}^2 \right) \tag{3-5}$$

where K is the bulk modulus, μ is the shear modulus, ρ is the density (g/cm^3), Vp is the compressional wave velocity (m/s), and Vs is the shear wave velocity.

The results for both bulk and shear modulus are shown in Figures 17 and 18, respectively. Both elastic moduli show an inverse correlation with porosity, thus as porosity increases, the elastic modulus decreases. When you compare Figures 17 and 18 to the velocity-porosity crossplot

(Figure 6), high velocities correlate to high elastic moduli, and scatter around the exponential best-fit curves at porosities higher than 35%.

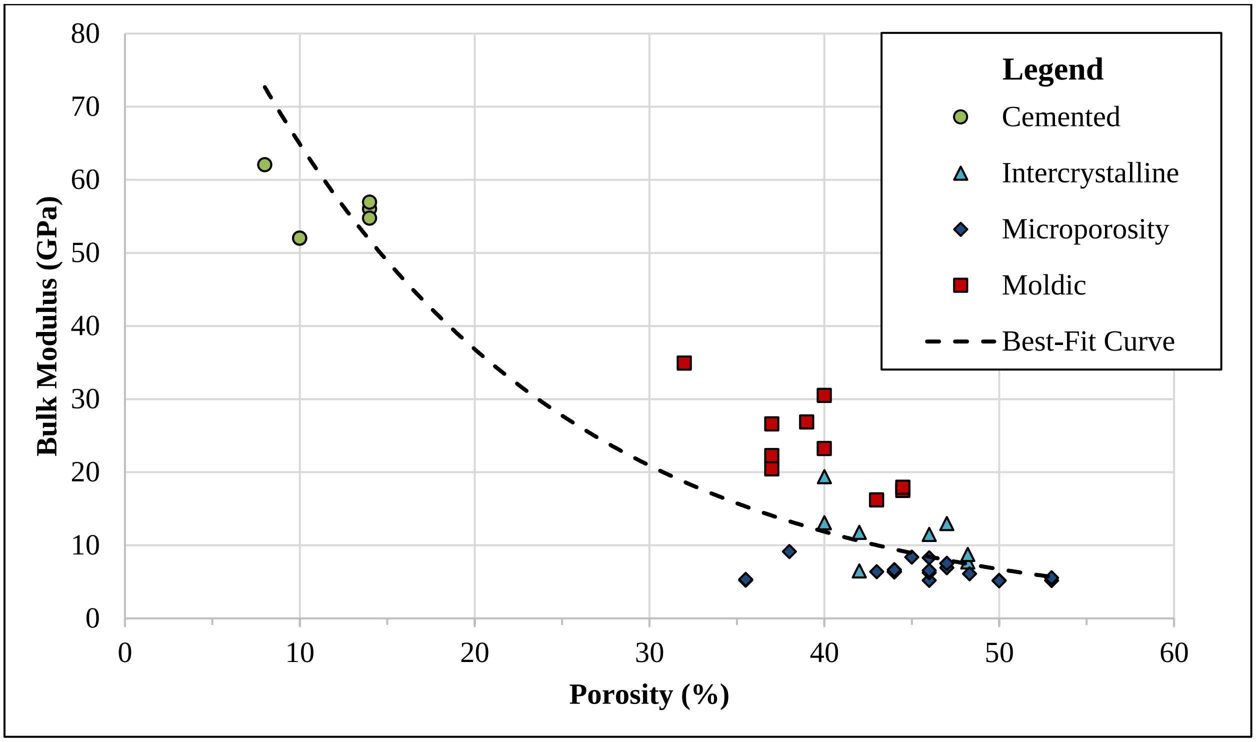

Figure 17. Porosity versus bulk modulus crossplot with pore types identified and an inverse correlation depicted.

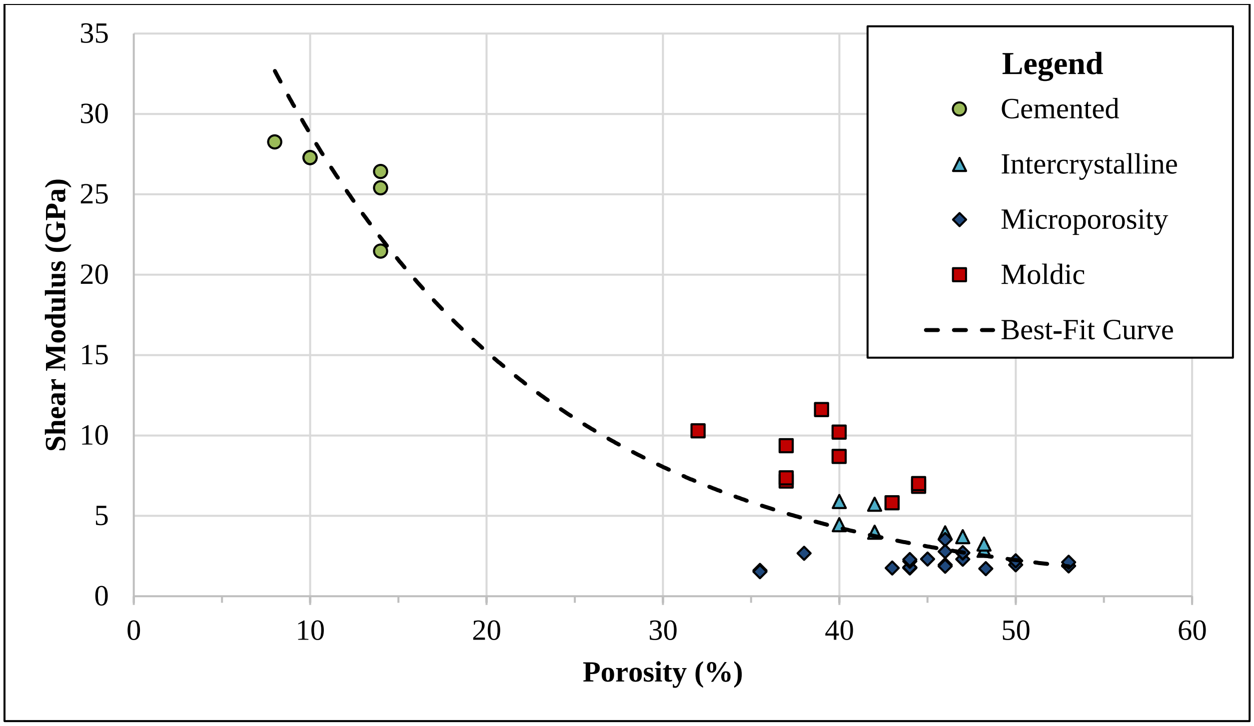

Figure 18. Porosity versus shear modulus crossplot with pore types identified and an inverse correlation depicted.

The four pore types identified show characteristic qualities of carbonate rocks in relation to elastic moduli and velocity. Pores with higher elastic moduli and higher velocities, like cemented pores and moldic pores, are due to a rigid rock framework composed of cement and micrite with better grain contacts. Intercrystalline and microporosity samples have no preferred orientation and are manipulated through applied stress. This absence of rigid framework and lack of cement or matrix, is why intercrystalline and microporosity pores produce low elastic moduli values and lower acoustic velocities.

3.7 Velocity Response to Diagenesis

Carbonate rock properties can be altered through diagenesis, and can undergo a variety of diagenetic alterations through their burial history. The studied samples have several diagenetic events that led to different pore types and patterns on the velocity-porosity diagram (Figures 20, 21, 22, and 23). The diagenetic evolution of four samples, consisting of a cemented pore, an intercrystalline pore, a microporosity pore, and a moldic pore, were inferred by Anselmetti and Eberli (1993) based on thin-section information. All samples start at deposition and end with the measured velocities, their final event in their diagenetic history, and are placed along the best-fit curve for all the samples (Figure 19).

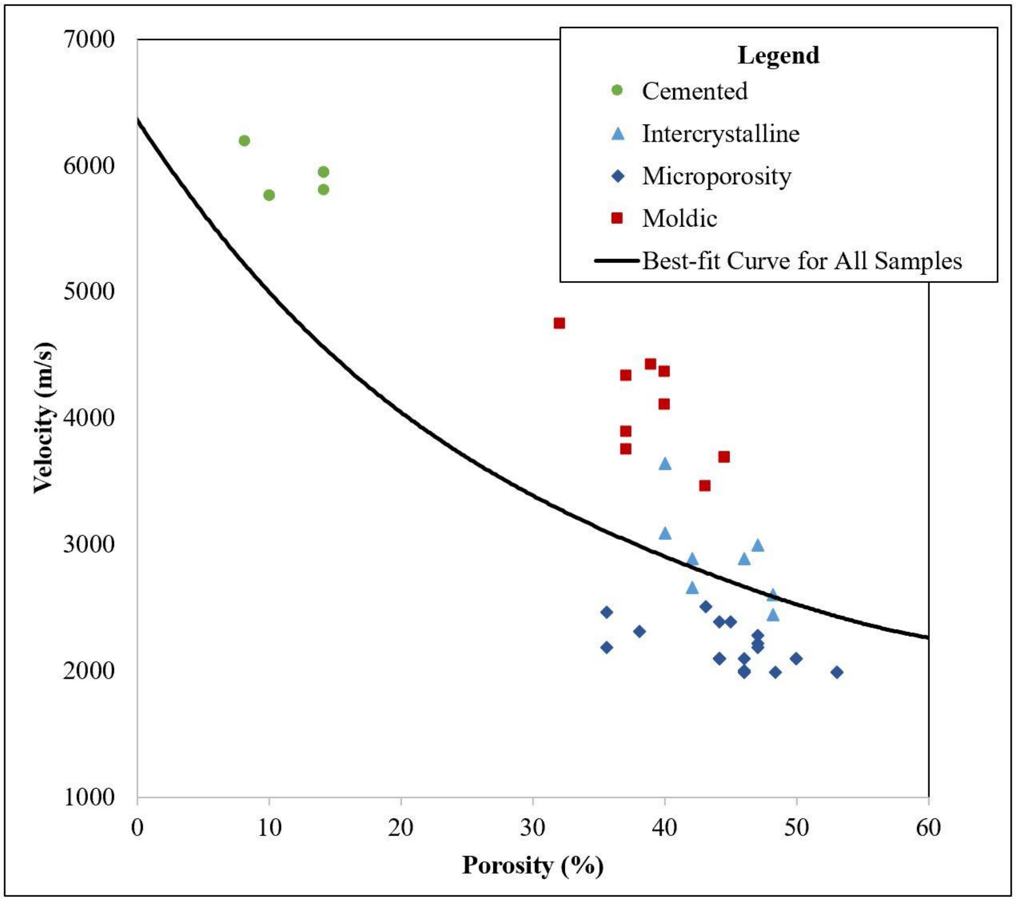

Figure 19. Porosity-velocity (Vp) crossplot with best-fit curve for all the samples with their major/most common pore types.

Figure 20 is a highly cemented grainstone sample from the Clino core at 351 meters with 9% porosity. The reduced porosity and increased velocity in the cemented sample is attributed to intense dolomitic cementation after dissolution of components. The complicated diagenetic history is depicted on the velocity-porosity diagram, with many curves representing the various diagenetic events and fabric alterations.

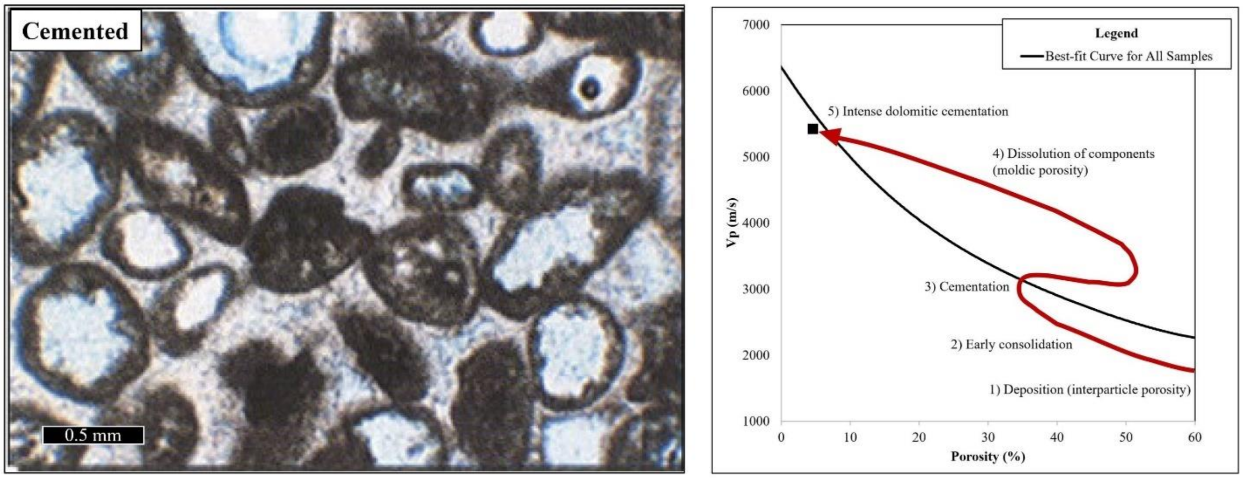

Figure 20. Inferred velocity-porosity paths for Bahamas sample (right) shown in photomicrograph (left). The black square in the velocity-porosity diagram (right) marks the measured velocity and porosity values for the sample. This is a highly cemented, low porosity sample from the Clino core at 351 meters, with porosity = 9%, Vp = 5661 m/s, and Vs = 3158 m/s (modified from Anselmetti and Eberli, 1993 and Massaferro et al., 2002 and Mammadova, 2011).

Figure 21 is a sucrosic dolomite (with relicts of red algae) intercrystalline sample from the Unda core at 322 meters in depth with a porosity of 46%. Lower velocities than the best-fit curve and increased porosities are attributed to the alteration of the depositional fabric in the intercrystalline porosity sample. The diagenetic history on the velocity-porosity diagram resulted in a curved arrow, due to the fabric destructive processes (dolomitization) and diagenetic events.

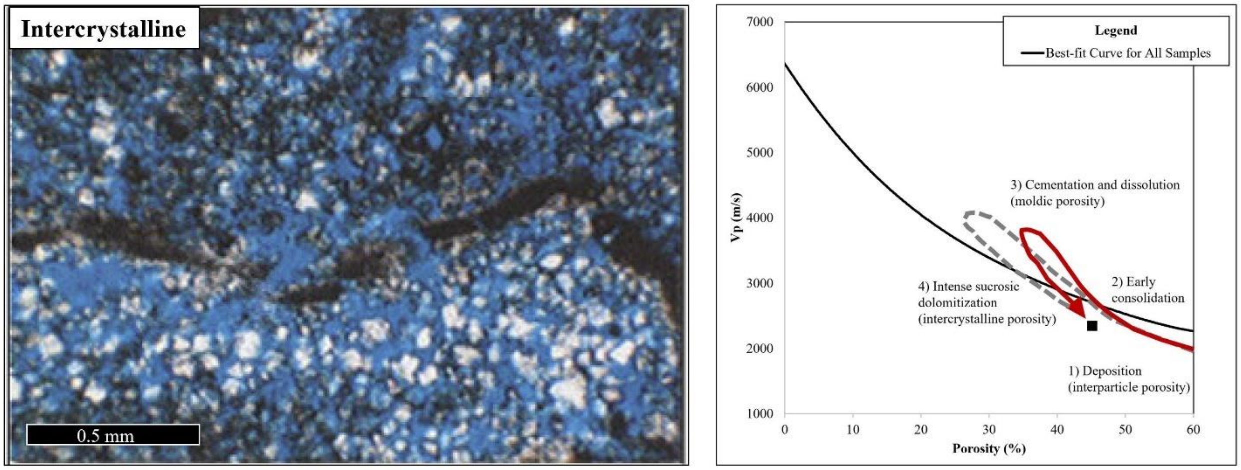

Figure 21. Inferred velocity-porosity paths (right) for sample shown in photomicrograph (left). The black square in the velocity-porosity diagram (right) marks the measured velocity and porosity values for the sample. This sample has intercrystalline porosity from the Unda core at 322 meters, with porosity = 46%, Vp = 2405 m/s, and Vs = 991 m/s (modified from Anselmetti and Eberli, 1993 and Massaferro et al., 2002 and Mammadova, 2011).

Figure 22, is a microporosity sample from the Clino core at 676 meters in depth, and with a porosity of 44%. This sample is comprised of peri-platform slope sediments with globigerinids, with most shells intact due to little compaction and some matrix recrystallization - despite the deep burial depth. A short arrow from deposition to present is shown on the velocity-porosity path, due to a limited diagenetic history (Anselmetti and Eberli, 1993).

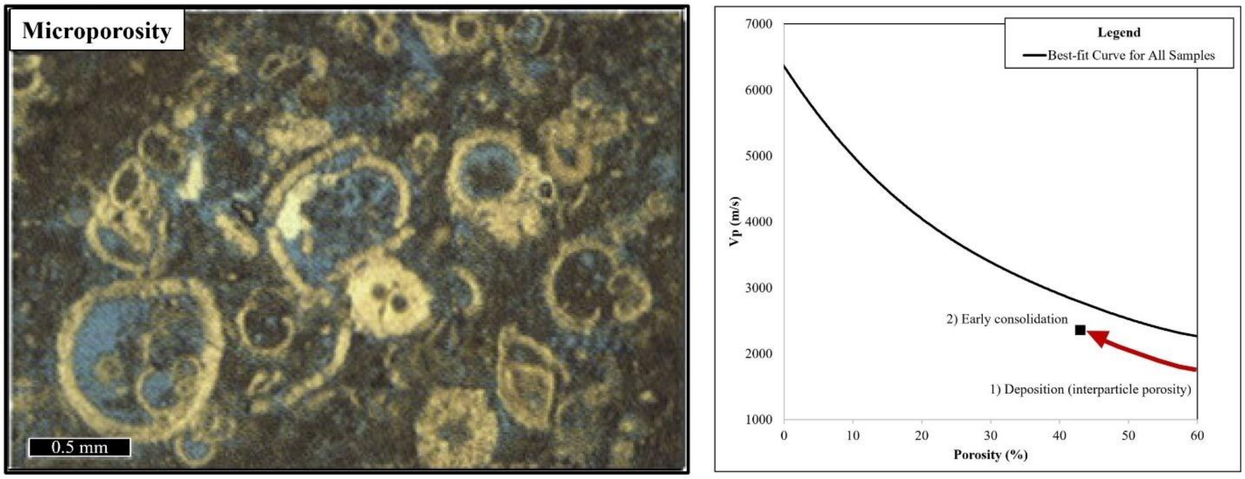

Figure 22. Inferred velocity-porosity paths for Bahamas sample shown in photomicrograph (left). The black square in the velocity-porosity diagram (right) marks the measured velocity and porosity values for the sample. This sample has abundant microporosity occurs in the Clino core at 676 meters depth, with porosity = 44%, Vp = 2478 m/s, and Vs = 1356 m/s (modified from Anselmetti and Eberli, 1993 and Massaferro et al., 2002 and Mammadova, 2011).

Figure 23, is a sample from the Unda core at 65 meters depth that contains a coarse moldic porosity which measured 37%. This sample was a former ooid-grainstone (oomoldic), where after early consolidation, the rock underwent blocky calcite cementation, and later dissolution of the ooid grains, resulting in moldic pore space. The diagenetic history on the velocity-porosity diagram resulted in a curved or “looped” arrow, due to the transformation of the ooid grainstone and five diagenetic stages.

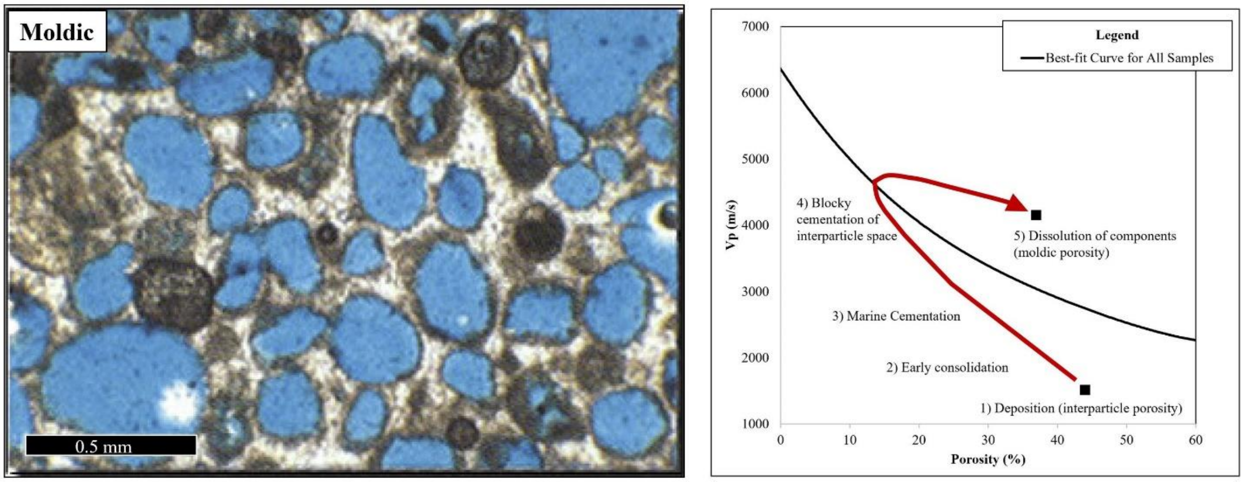

Figure 23. Inferred velocity-porosity paths (right) for Bahamas sample shown in photomicrograph (left). The black square in the velocity-porosity diagram (right) marks the measured velocity and porosity values for the sample. This sample has coarse moldic porosity from the Unda core at 65 meters, porosity = 37%, Vp = 4105 m/s, and Vs = 1640 m/s (modified from Anselmetti and Eberli, 1993 and Massaferro et al., 2002 and Mammadova, 2011).

The diagenetic processes control and alter the velocities of carbonate rocks before compaction, which is why the velocities of carbonate rocks show no clear correlation with increasing depth (Anselmetti and Eberli, 1993). The diagenetic history on the velocity-porosity diagrams correlate to diagenetic processes, and the direction of the path is dependent on the order and timing of the various diagenetic events (Anselmetti and Eberli, 1993).

3.8 Pressure Analysis

Anselmetti and Eberli (1993) studied velocity measurements determined under varying effective pressures to observe the pressure dependence of acoustic velocities. The results of this study showed that at low pressures, all the samples increased in velocity with increasing pressure. The velocities of rigid, dense samples were unaffected by higher pressures, where there was a large increase in velocities for slow, unconsolidated samples (Anselmetti and Eberli, 2001). All velocity-pressure traces of the Clino and Unda samples plotted (Figure 24) show a pattern with higher gradients for low-velocity, high-porosity samples and lower gradients for high-velocity, low-porosity samples. One noted characteristic of the samples, is that the velocities reached a maximum during increasing pressure and suddenly began to decrease above a critical pressure, due to the sample collapsing (Anselmetti and Eberli, 2001). The shear wave velocity is affected by the destroyed fabric, resulting in non-elastic behavior.

The velocity evolution of the four pore types (cemented, intercrystalline, microporosity, and moldic), is dependent on pore types and lithologies. As mentioned previously, highly cemented, low-porosity samples are unaffected by higher pressures, resulting in a pattern of minimal gradients on the velocity-pressure plot. Samples with intercrystalline porosity show an increase in velocity with increasing pressure (Mammadova, 2011). Microporosity samples also show an increase in velocities, as they are generally low-velocity. Depending on the pore size and connectivity, moldic pores show different behaviors as effective pressure is increased. The general trend being, that smaller moldic pores collapse more in the pressure vessel than the more rigid, coarse moldic pores that have a more minimal gradient (Mammadova, 201!).

The critical pressure where the velocity begins to decrease happens at different values dependent on lithology. Some samples of dense, hard rocks reached to the highest measured pressure of 100 MPa without any evidence of fabric destruction and completely preserving the porosity of partly cemented rocks (Anselmetti and Eberli, 1993). Samples of unconsolidated, soft rocks started showing signs of a decrease in velocity at 5 MPa, meaning that these carbonate rocks (especially most slope deposits and sucrosic dolomites) were buried without compaction (Anselmetti and Eberli, 1993).

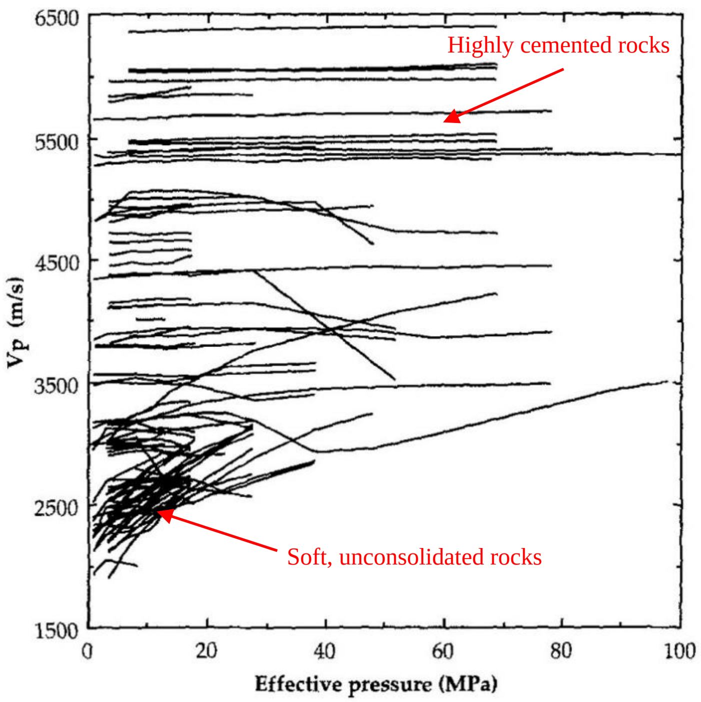

Figure 24. Velocity evolution of all the Clino and Unda samples at increasing effective pressures. Each trace represents the velocities at different pressures for one sample. Decreasing velocities at higher pressures mark a critical pressure at which the sample fractures and collapsed. The velocity gradient of unconsolidated, slow, high-porosity samples is higher than the rigid, fast, low-porosity samples that were unaffected by higher pressures and therefore, have a minimal velocity gradient change (modified from Anselmetti and Eberli, 1993).

3.9 Conclusion

This geological analysis aimed to address how carbonate rock pore types influence the petrophysical properties (e.g. mineralogy, porosity, permeability, density, velocity, pressure, and elastic moduli). The four pore types identified were: 1) cemented, 2) intercrystalline, 3) microporosity and 4) moldic.

The limited variability in mineralogy composition, showed no correlation to velocity contrasts. This is due to the similar physical properties among calcite, dolomite, and aragonite. There is no relationship between depth/age and velocity trends for the Clino and Unda cores. There is a correlation between depositional environments and velocity distributions. High velocities are exhibited for shallow-water deposits due to diagenetic alterations that occur at shallow depths.

Porosity is the main factor controlling acoustic wave velocities, but carbonate rocks with the same porosity can have different velocities due to the geometries of the pore types. Looking at individual pore types, cemented pores displayed low porosity, high velocity, low permeability, high density, and high elastic moduli. Microporous samples showed high porosity, low velocity, high permeability, low density, and low elastic moduli. Generally, density increases and porosity decreases with an increase in depth and pressure, because the grains shift into a denser packing with an increase in pressure with depth. Another explanation, is the possibility that diagenetic processes, like cementation, work to fill the pore space and increase density. The absence of rigid framework and lack of cement or matrix, is why intercrystalline and microporous rocks produce low elastic moduli values and lower acoustic velocities.

The diagenetic history correlates to diagenetic events, with the direction of the path dependent on the order and timing of events. The velocity-pressure plot shows higher gradients for low velocity, high porosity samples, and vice-versa.

4. ROCK PHYSICS MODELS

4.1 Introduction

Rock physics has become an integral part of petroleum exploration, as it provides a link between qualitative geological properties and quantitative geophysical measurements. The application of rock physics in the petroleum industry can improve reservoir characterization and reduce exploration risks. The complexity of carbonate rock pore geometries, however, makes the development of an accurate rock physics model difficult. A rock physics model that takes the carbonate rock pore types into account is essential in creating an effective characterization of carbonate rocks and potential carbonate rock reservoirs. This chapter covers basic rock physics principles and their application to the carbonate rock data collected from the Bahamas' Clino and Unda cores.

4.2 Wyllie's Time-Average Model

As mentioned previously, Wyllie's (1958) "time-average formula" is used as a reference curve providing a linear relationship between velocity and porosity.

This simplified empirical equation is:

$$\frac{1}{V} = \frac{\emptyset}{V_F} + \frac{1-\emptyset}{V_M} \tag{3-1}$$

where V is the velocity measured, V_F is the velocity in saturating liquid, V_M is the velocity in rock matrix, and $\emptyset$ is the volumetric porosity. Wyllie's equation has been used for years due to its simplicity, but the comparison of the measured P-wave velocity to Wyllie's theoretical equation shows underestimated velocities for the Bahamian carbonate rocks (Figures 6 and 25).

This inaccuracy (Figure 26) and underestimation of velocities is due to the fact that Wyllie’s equation does not account for velocity variations in carbonate pore types and diagenetic textures.

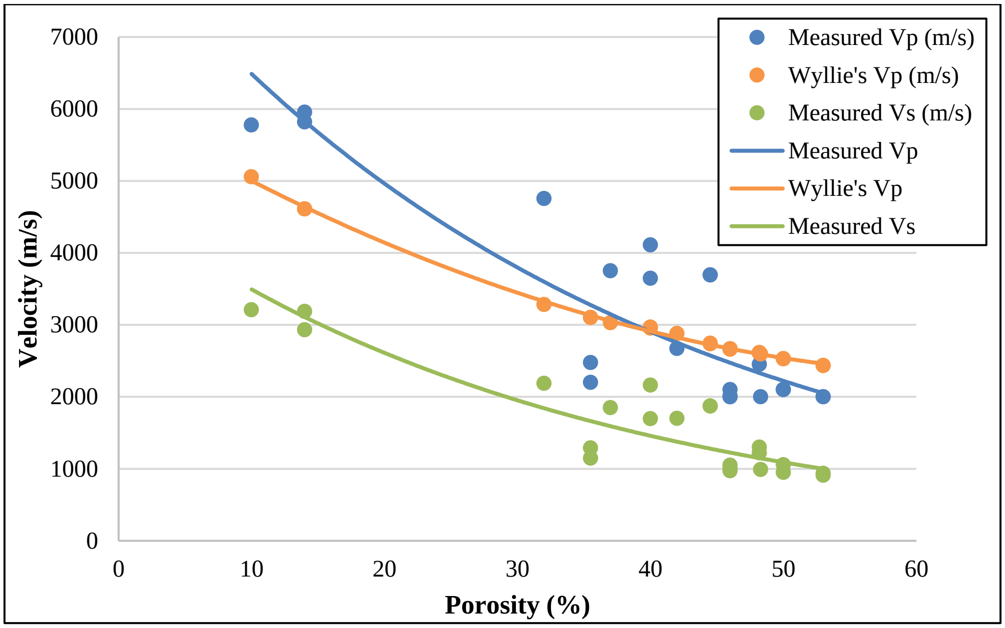

Figure 25. Porosity-velocity crossplot of the Bahamas dataset in comparison to Vp calculated with Wyllie's (1958) equation. Comparison of the measured P-wave velocity to Wyllie’s theoretical equation (1958) Vp calculations show underestimated velocities for the Bahamian carbonate rocks

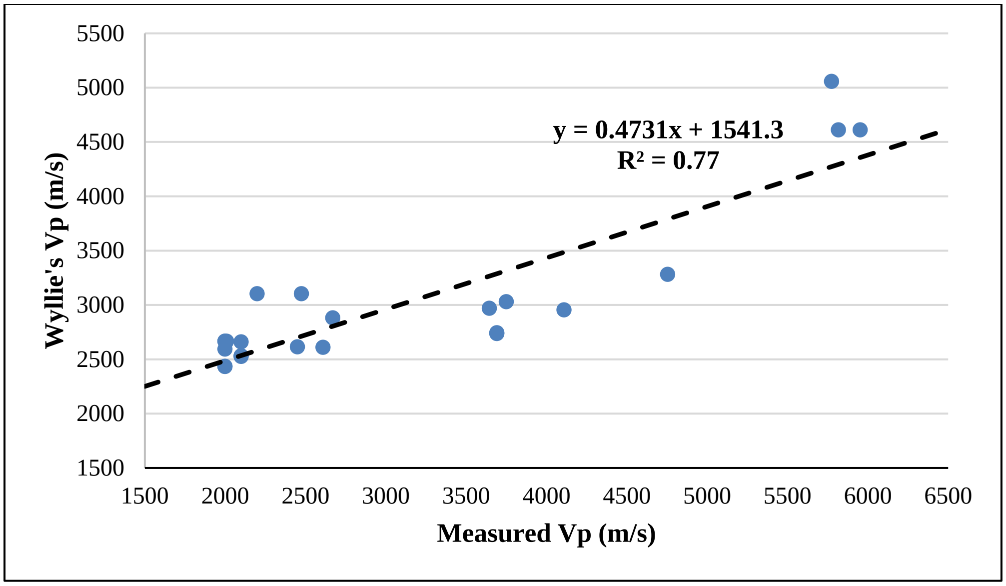

Figure 26. Diagram of measured Vp versus Wyllie's (1958) Vp displays the inaccuracy of this method as it has a correlation of 0.77, instead of 1.

4.3 Voigt and Reuss Bounds

4.3.1. Reuss Bound

The Reuss model (1929), an isostress model (sometimes called the isostress average), assumes the stress is uniform throughout the aggregate of crystals. The strain is expressed in terms of the given stress in an aggregate of crystals:

$$\frac{1}{M_r} = \sum_{i=1}^{n} \frac{\varphi i}{M_i} \qquad \textbf{(4-1)}$$

where M_r can represent either the bulk or shear modulus, φi is the volume fraction, and M_i is the modulus of the ith component. The effective medium is macroscopically isotropic. The calculated effective modulus using this model is the lower bound of the effective modulus.

4.3.2. Voigt Bound

The Voigt model (1928), an isostrain model (sometimes called the isostrain average), assumes that the strain is uniform throughout the aggregate of crystals. The stress in a single crystal in terms of the given strain is expressed:

$$M_v = \sum_{i=1}^{n} \varphi i \, M_i \qquad \textbf{(4-2)}$$

where M_v is the Voigt effective modulus representing either bulk or shear, φi is the volume fraction, and M_i is the modulus of the ith component. The calculated effective modulus using this model is the upper bound of the effective modulus.

4.3.3. Voigt-Reuss-Hill (VRH) Method

Knowing that the Voigt model is the upper bound and the Reuss model is the lower bound of the effective moduli, the Hill model (1952) combined both models into an empirical averaging relation. This model is expressed as:

$$M = \frac{1}{2}(M_v + M_r) \text{ where } M_r \leq M \leq M_v \qquad \textbf{(4-3)}$$

where M is the VRH effective modulus representing either bulk or shear, M_v is the Voigt effective modulus representing either bulk or shear, M_r is the Reuss effective modulus representing either bulk or shear.

The Voigt-Reuss-Hill (VRH) model gives an approximate value for the effective modulus, specifically useful in estimating the moduli of a rock matrix composed of different minerals – if data from a mineralogy analysis is available. This estimation of the solid matrix bulk moduli calculated from the VRH model is later used in the Gassmann equation to calculate the bulk modulus of a fluid-saturated porous medium. To calculate the effective moduli of a gas-saturated rock or the effective shear modulus of fluid-saturated (both liquid and gas) rock, the VRH model cannot be used. The calculated effective modulus using this model is an average between both upper and lower bounds.

4.3.4. Comparison of Voigt/Reuss/VRH Models

Various models can be used to estimate the velocity (Vp) and effective bulk modulus (Ke) of a formation, used to describe the reservoir's elastic properties from lithology and porosity. The range of the formation velocity is calculated by the upper and lower bounds of the Voigt and Reuss models. The Voigt bound iso-strain model is the upper bound, the Reuss iso-stress model is the lower bound, and the Voigt-Reuss-Hill (VRH) model is the average between both bounds. The Voigt, Reuss, and VRH models use the average acoustic properties of the percent composition of the material present. The average velocity and bulk modulus of each material present is multiplied by that material's composition.

The Voigt Model:

$$V_V = \sum_{n=1}^{n} V_n * (\%C_n) \tag{4-4}$$

and,

$$K_V = \sum_{n=1}^{n} K_n * (\%C_n) \tag{4-5}$$

where V is the P-wave velocity (m/s), K is the bulk modulus (GPa), and (%Cn) is the percent of the composition of the nth material for the Voigt model. The Voigt model is the upper bound of the effective modulus.

The Reuss model:

$$V_R = \sum_{n=1}^{n} (V_n * (\%C_n))^{-1} \tag{4-6}$$

and,

$$K_R = \sum_{n=1}^{n} (K_n * (\%C_n))^{-1} \tag{4-7}$$

where V is the P-wave velocity (m/s), K is the bulk modulus (GPa), and (%Cn) is the percent of the composition of the nth material for the Reuss model. The Reuss model is the lower bound of the effective modulus.

The Voigt-Reuss-Hill (VRH) model:

$$V_H = \frac{V_V + V_R}{2} \tag{4-8}$$

and,

$$K_H = \frac{K_V + K_R}{2} \tag{4-9}$$

where Vv is the Voigt model velocity (m/s), Vr is the Reuss model velocity (m/s), Kv is the Voigt model bulk modulus (GPa), and Kr is the Reuss model bulk modulus (GPa). The Voigt-Reuss-Hill model is the average of the effective modulus and both bounds. The VRH equation will be used for this research.

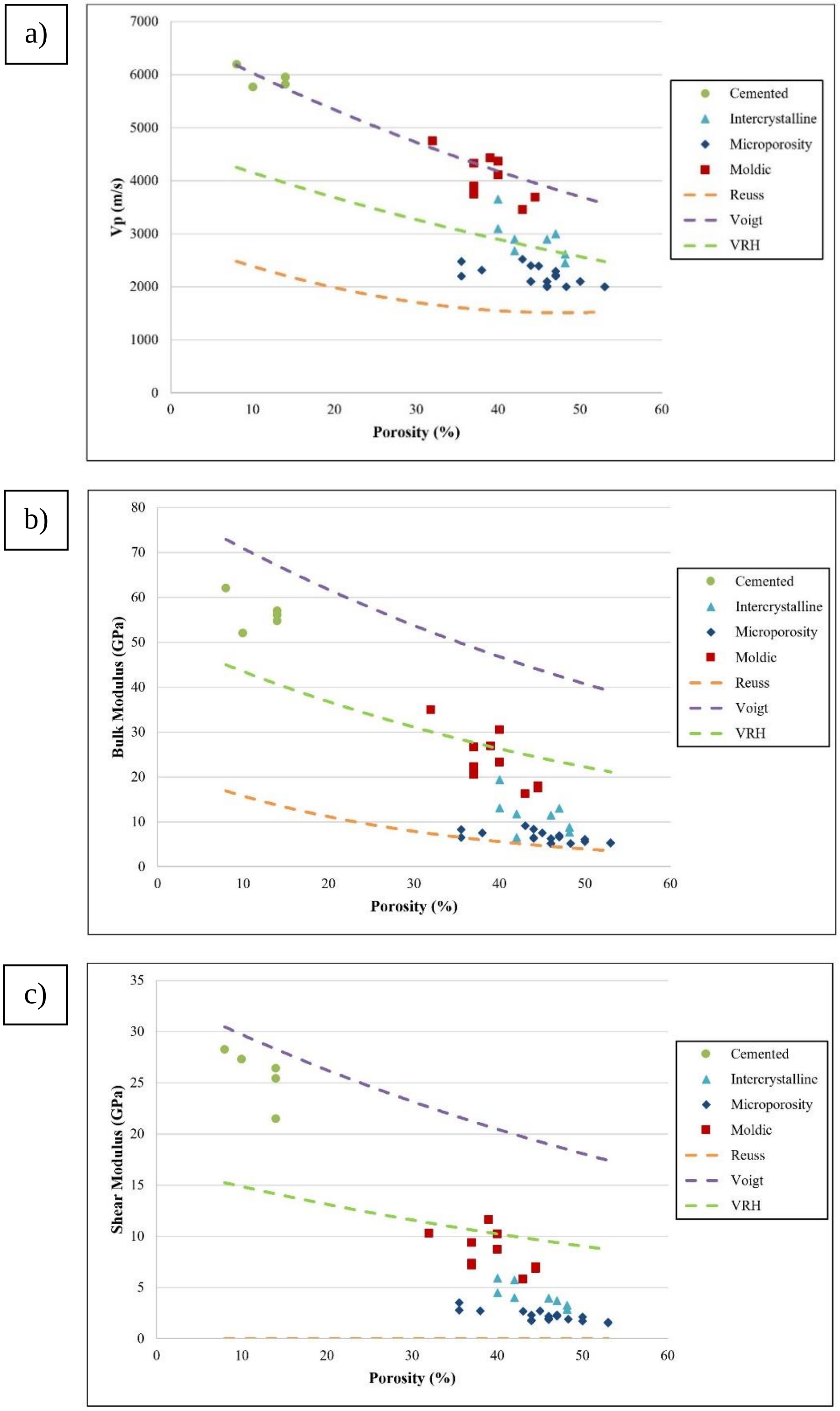

Figure 27. Comparison of Reuss, Voigt, and VRH models for all samples with carbonate pore types. (a) diagram of porosity-Vp with bounds (b) crossplot of porosity-bulk modulus with bounds (c) crossplot of porosity-shear modulus with bounds.

Figure 27 shows that the Reuss model is the lower bound, Voigt is the upper bound, and VRH is the average for both the Vp, bulk moduli, and shear moduli. Any data points not within the bounds could potentially have errors, but majority of the data points are between the bounds.

4.4 Gassmann Fluid Substitution Model

Using the modified Biot-Gassmann Equation (Gassmann, 1951; Biot, 1956) for fluid substitution modeling:

$$\frac{1}{C - C_m} = \frac{1}{\bar{C} - C_m} + \left(\frac{1}{C_{fl} - C_m}\right)\frac{1}{\emptyset} \quad \textbf{(4-10)}$$

where C is the compressibility of fluid-saturated rock, $\bar{C}$ is the compressibility of the dry rock frame, C_m is the compressibility of the mineral matrix, C_{fl} is the compressibility of the pore fluid, $\emptyset$ is the porosity of the rock.

The compressibility of the rock is the inverse of the rock's bulk modulus at a constant pore pressure. Knowing this, the bulk modulus equation was determined and written as below:

$$K = \frac{\emptyset\left(\frac{1}{K_{fl}} - \frac{1}{K_s}\right) + \frac{1}{\overline{K}} - \frac{1}{K_s}}{\frac{1}{K_s}\left(\frac{1}{\overline{K}} - \frac{1}{K_s}\right) + \emptyset\frac{1}{\overline{K}}\left(\frac{1}{K_{fl}} - \frac{1}{K_s}\right)} \quad \textbf{(4-11)}$$

where K is the bulk modulus, $\overline{K}$ is the effective frame bulk modulus, K_{fl} is the fluid bulk modulus, K_s is the solid bulk modulus, and $\emptyset$ is the porosity.

Manipulating this equation to find the effective frame bulk modulus in the equation below, using the same properties:

$$\bar{K} = \left[\frac{\emptyset\left(\frac{1}{K_{fl}} - \frac{1}{K_s}\right) - \frac{1}{K_s} + \frac{1}{{K_s}^2}}{\frac{K}{K_s} + \frac{K\emptyset}{K_{fl}} - \frac{K\emptyset}{K_s} - K} \right]^{-1} \tag{4-12}$$

where $\bar{K}$ is the effective frame bulk modulus, K_{fl} is the fluid bulk modulus, K_s is the solid bulk modulus, K is the bulk modulus, and $\emptyset$ is the porosity.

The applicability of Gassmann's equation in carbonate rocks is not well understood, due to assumptions the Gassmann equations is derived on. A major assumption for the Gassmann equation is that the shear modulus is independent of the pore fluid content:

$$\mu_{sat} = \mu_{dry} \tag{4-13}$$

where μ_{sat} is the saturated shear modulus and μ_{dry} is the dry shear modulus or "frame shear modulus". The reasoning behind this assumption is that since fluid theoretically has negligible resistance to shear change, the shear modulus for all fluids will be considered 0 GPa and therefore the velocity of the S-wave through a fluid will also be considered 0 m/s.

To find the bulk modulus of the mineral matrix or solid rock (inverse of the compressibility of the mineral matrix), the previously described Voigt-Reuss-Hill (VRH) average must be calculated knowing the mineralogy of the samples. The samples from the Clino and Unda cores are exclusively composed of calcite, aragonite, and dolomite. Equations (4-5) (4-7), and (4-9), can be rewritten as:

$$K_{Reuss} = \left[\frac{F_1}{K_1} + \frac{F_2}{K_2} + \frac{F_3}{K_3}\right] \tag{4-14}$$

$$K_{Voigt} = [F_1K_1 + F_2K_2 + F_3K_3] \tag{4-15}$$

$$K_{VRH} = \frac{1}{2}\left[K_{Reuss} + K_{Voigt}\right] \tag{4-16}$$

where F_1, F_2, F_3 are volumetric fractions of the three mineral components, and K_1, K_2, K_3 are the bulk modulus of calcite (76.8 GPa), aragonite (44.8 GPa), and dolomite (94.9 GPa).

4.5 Sun Model and Frame Flexibility Factors

The model introduced by Sun (2004, 2000) effectively quantifies the effect the pore structure and its connectivity have on the elastic properties of the rock. These key elastic parameters are known as "frame flexibility factors" and are used widely for carbonate reservoir characterization, as they characterize the effect of pore structure, grain contacts and grain coupling, cementation and pore connectivity on the flexibility and elasticity of a porous rock (Sun, 2004). A set of working formulas for this model are:

$$V_p = \sqrt{\frac{K + \frac{4}{3}\mu}{\rho}} \tag{3-2}$$

$$V_s = \sqrt{\frac{\mu}{\rho}} \tag{3-3}$$

$$\rho = (1 - \emptyset)\rho_s - \emptyset\rho_{fl} \tag{4-17}$$

$$K = (1 - \emptyset_k)K_s - \emptyset_k K_{fl} \tag{4-18}$$

$$\emptyset_k = \emptyset F_K \tag{4-19}$$

$$F_K = \frac{1 - (1 - \emptyset)f}{[1 - (1 - \emptyset)f]\frac{K_{fl}}{K_s} + \left(1 - \frac{K_{fl}}{K_s}\right)\emptyset} \tag{4-20}$$

Equation 4.20 is simplified to:

$$F_K = \frac{K_s - K}{\emptyset\left(K_s - K_{fl}\right)} \tag{4-21}$$

$$f = \frac{1 - \left(\frac{K_{fl}}{K_s} + \left(1 - \frac{K_{fl}}{K_s}\right)\emptyset\right)F_k}{(1-\emptyset)\left(1 - \frac{K_{fl}}{K_s}F_k\right)} \tag{4-22}$$

$$\mu = \mu_s(1-\emptyset)f_\mu \tag{4-23}$$

$$f = (1-\emptyset)^{\gamma-1} \tag{4-24}$$

$$f_\mu = (1-\emptyset)^{\gamma_\mu - 1} \tag{4-25}$$

$$\gamma = 1 + \left(\frac{\ln(f)}{\ln(1-\emptyset)}\right) \tag{4-26}$$

$$\gamma_\mu = 1 + \left(\frac{\ln\left(f_\mu\right)}{\ln(1-\emptyset)}\right) \tag{4-27}$$

$$c = \gamma_\mu/\gamma \tag{4-28}$$

where;

ρ - bulk density,

K - bulk modulus of the fluid saturated rock,

μ - shear modulus,

ρ_m - solid matrix density,

K_s - solid matrix bulk modulus,

μ_s - solid matrix shear modulus,

ρ_{fl} - fluid density,

K_{fl} - fluid bulk modulus,

$\emptyset$ - porosity,

f, f_μ - frame stiffness factors,

γ, γ_μ - frame flexibility factors or coupling coefficients,

c – ratio of γ_μ/γ.

The frame stiffness factors (f) are explicit functions of porosity, and it is assumed that γ and γ_μ are independent of porosity (Sun, 2004). The γ parameters known as the frame flexibility factor (Equations 4.26 and 4.27), under deformation, characterize the flexibility of the rock frame due to the presence of pore structures (Sun, 2004). Due to pore structures and porosity, the f parameters known as the frame stiffness factor (Equations 4.24 and 4.25), under deformation, describe the stiffness and rigidity of the rock frame (Sun, 2004). Generally, higher γ values are related to less grain contacts and grain coupling, but due to diagenesis altering the rock to create textures that result in high pore-connectivity and rigid rock frame with better grains contacts, this may result in lower γ values (Mammadova, 2011).

The frame flexibility values for all 46 Clino and Unda samples were calculated, as shown in Appendix C. Samples with lower frame flexibility factors have high acoustic wave velocities (Figures 28 and 29). Comparing Figure 28 to Figure 19 where pore types are identified on a velocity-porosity diagram, samples with the frame flexibility factors (γ, γ_μ) less than 4 are rocks with moldic porosity. Samples with flexibility factors greater than 4 usually are sucrosic dolomite with intercrystalline porosity, or microporosity rocks with high concentrations of lime mud, or highly cemented rocks.

In Figures 30 and 31, highly cemented, low porosity, high velocity samples show the lowest frame flexibility values, whereas high porosity, low velocity microporosity samples show the highest frame flexibility values. Frame flexibility is not influenced by porosity. From lowest to highest frame flexibility factor values, the order of the pore types is: cemented, moldic, intercrystalline, and microporosity. Higher value flexibility factors, like those in microporosity and intercrystalline pores, are contributed to a lack of cementation, resulting in an unconnected grain fabric (Mammadova, 2011). Lower frame flexibility values, like in moldic pores, are due to a rigid, solid framework and their level of grain connectivity.

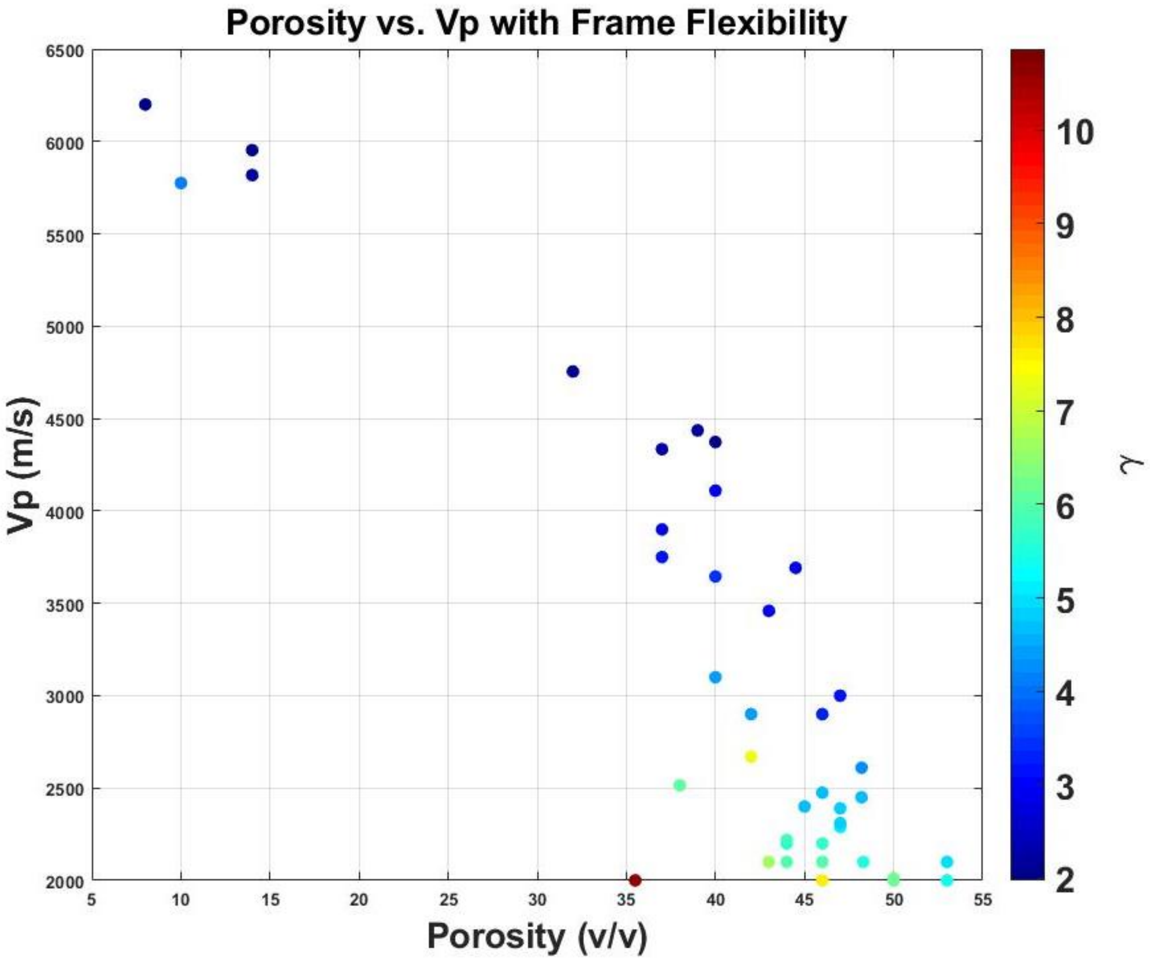

Figure 28. Velocity-porosity crossplot for compressional-wave velocity (Vp) with frame flexibility (γ).

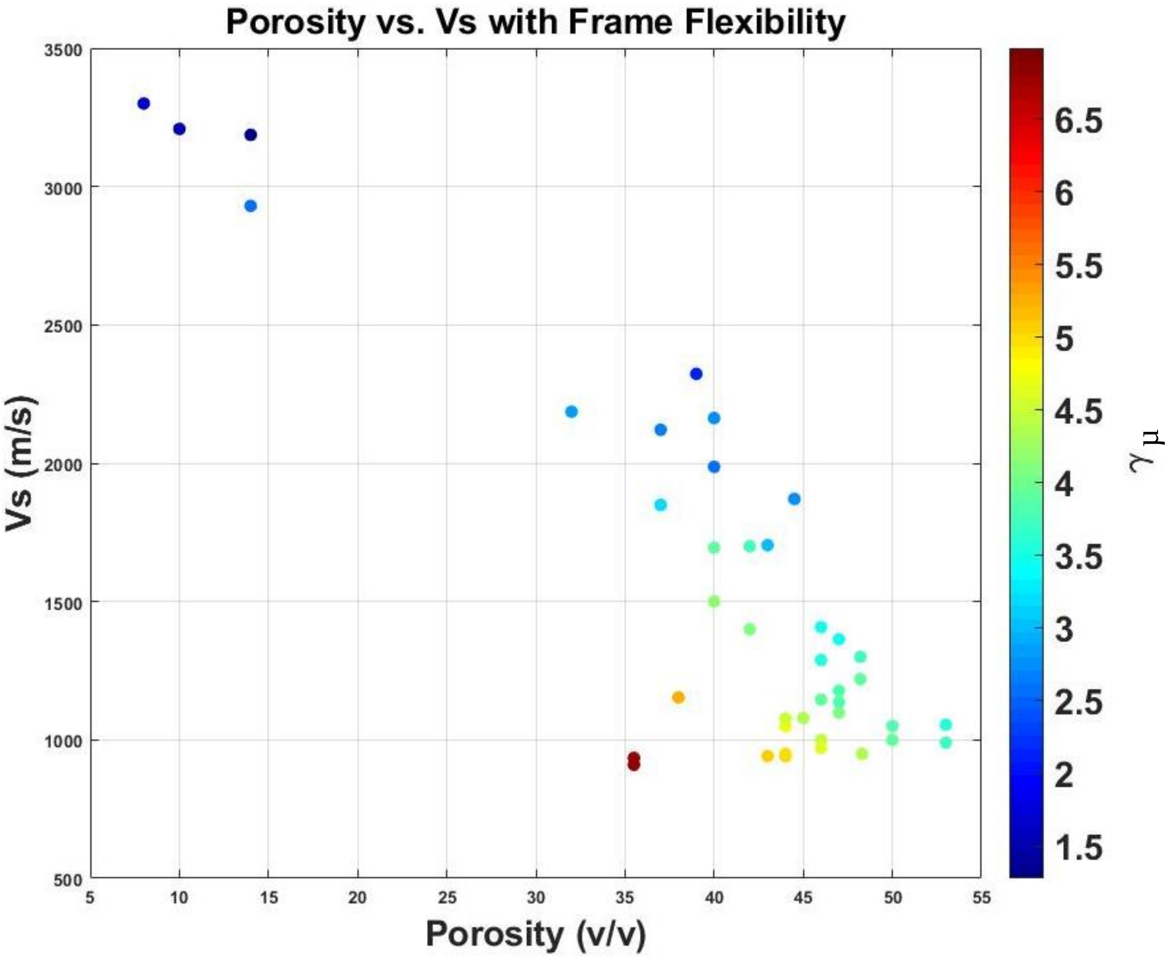

Figure 29. Velocity-porosity crossplot for shear-wave velocity (Vs) with frame flexibility (γ_μ).

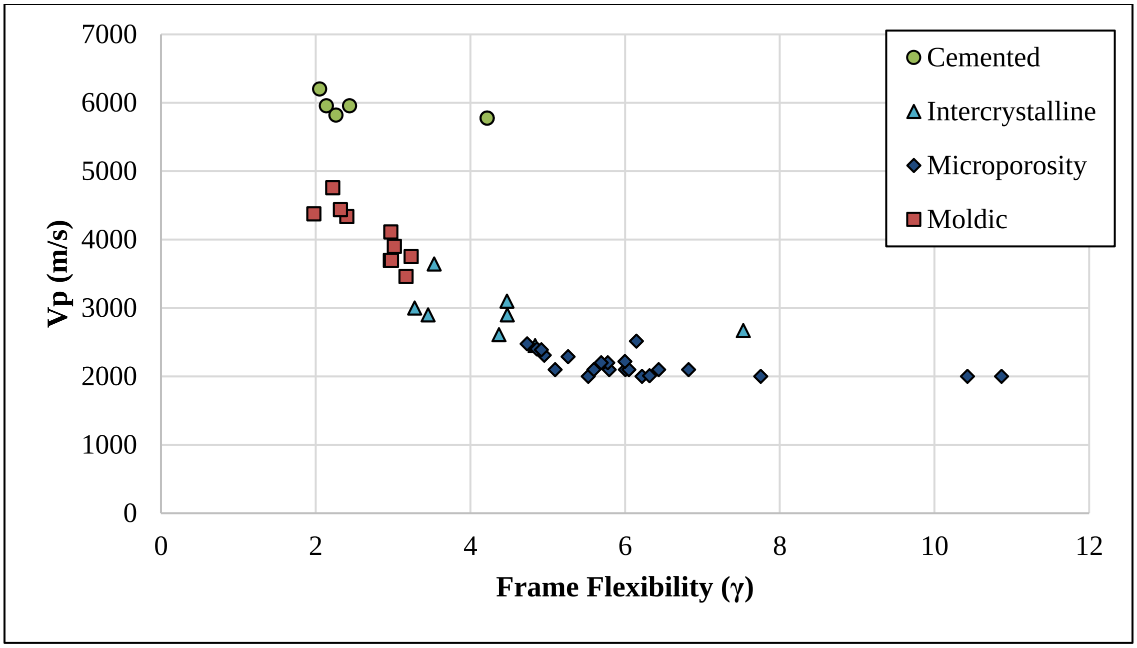

Figure 30. Diagram with frame flexibility factors (γ) versus P-wave velocity (Vp) and pore types identified.

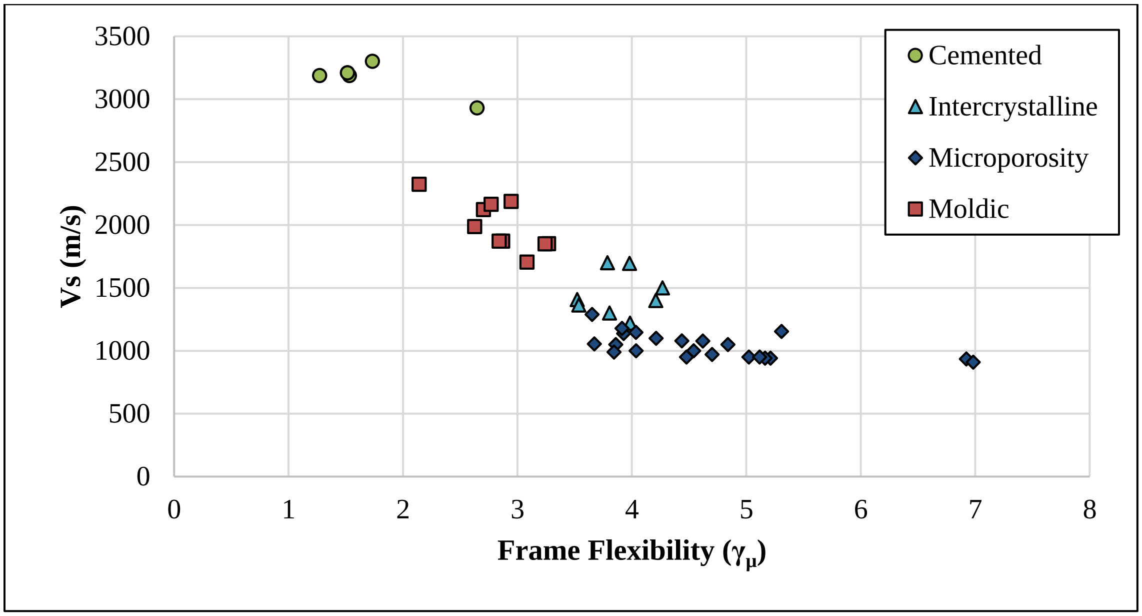

Figure 31. Diagram with frame flexibility factors (γ_μ) versus S-wave velocity (Vs) and pore types identified.

The same relationship, previously mentioned, occurs between elastic moduli, frame flexibility and pore types. Higher frame flexibility is shown in microporosity with low bulk and low shear modulus values, whereas lower frame flexibility is shown in cemented pores with high bulk and high shear modulus values (Figures 32, 33, 34, and 35). Overall, the relationship is low frame flexibility factor values are associated with low porosities, high velocities, high bulk modulus, and high shear modulus. The opposite is true for low frame flexibility factor values, they are associated with high porosities, low velocities, low bulk modulus, and low shear modulus.

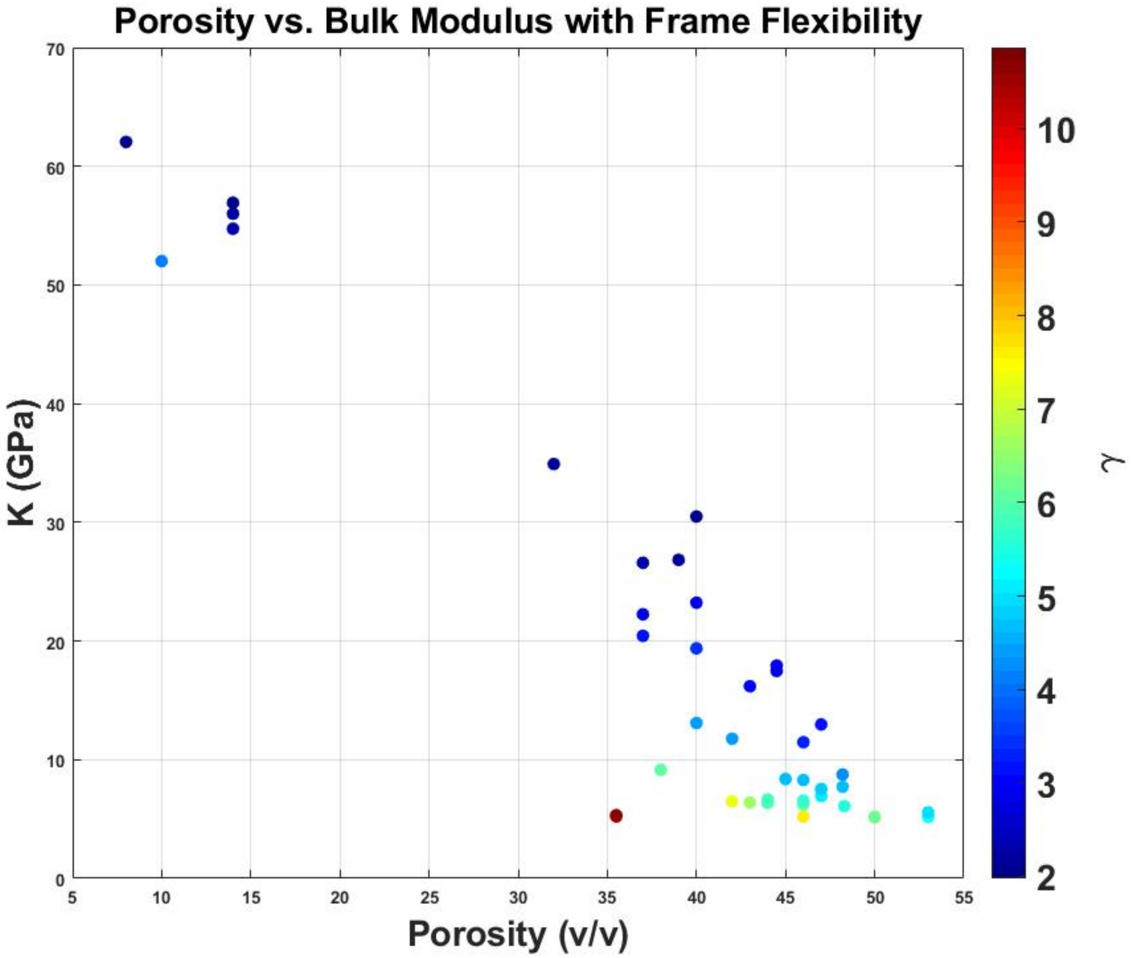

Figure 32. Bulk modulus-porosity crossplot with frame flexibility (γ).

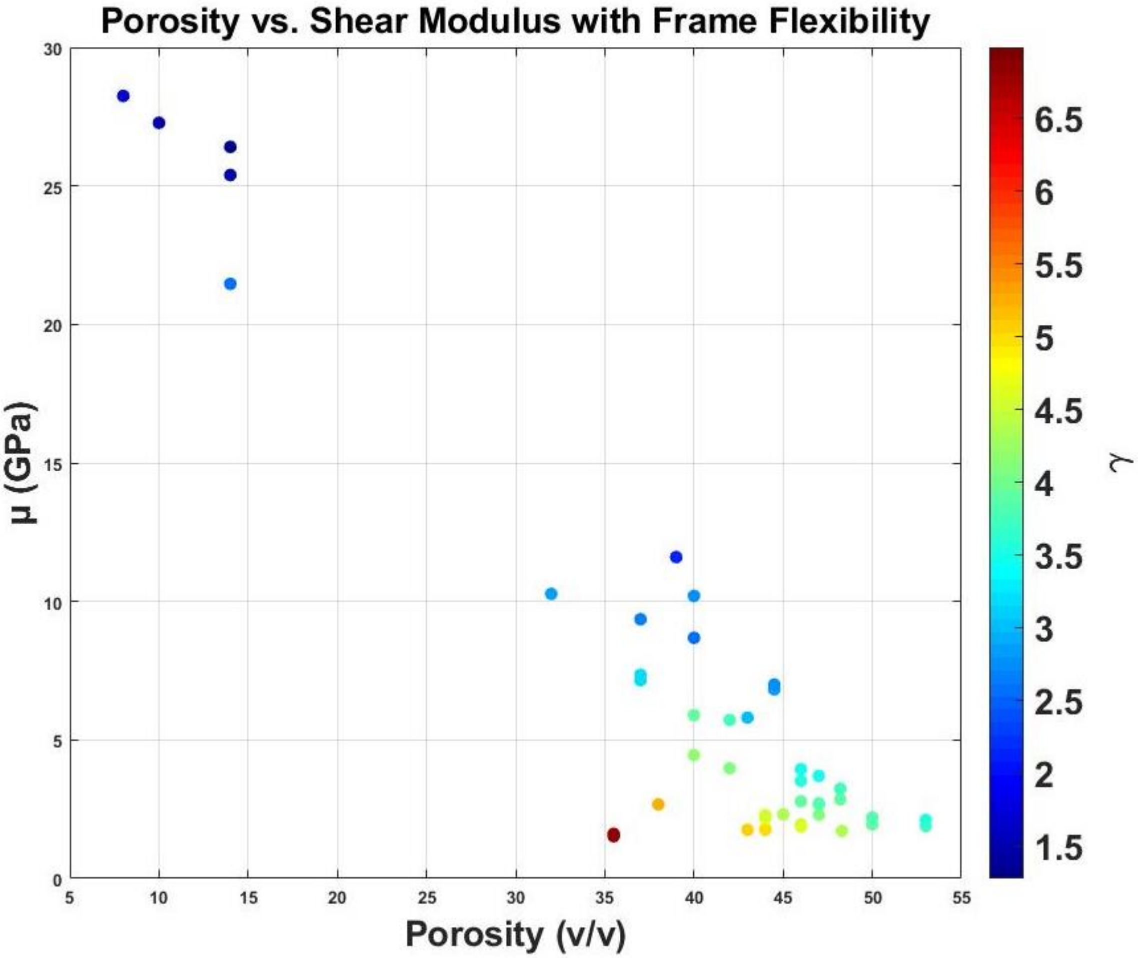

Figure 33. Shear modulus-porosity crossplot with frame flexibility (γ_μ).

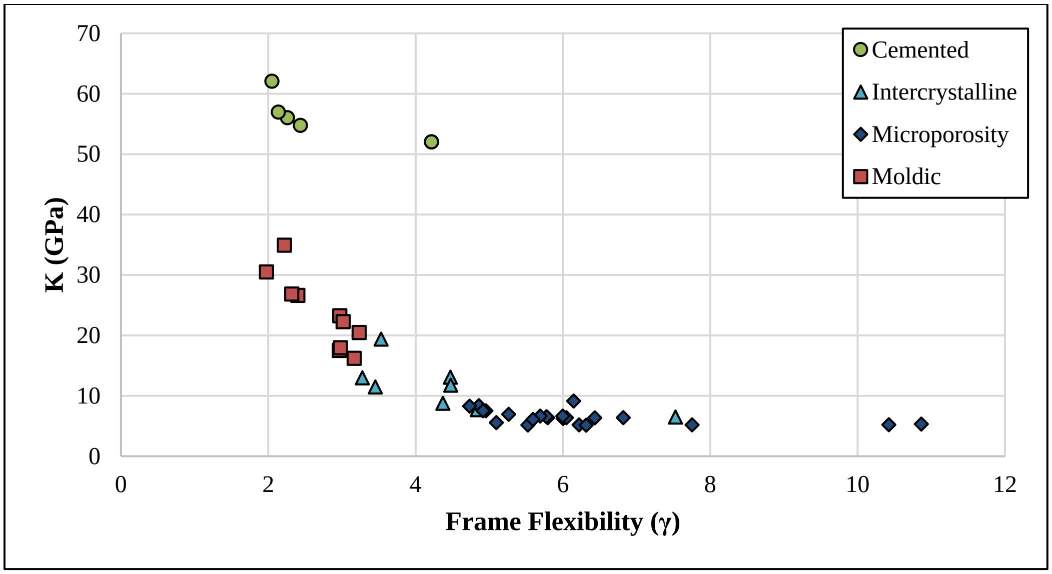

Figure 34. Diagram with frame flexibility factors (γ) versus bulk modulus (K) and pore types identified.

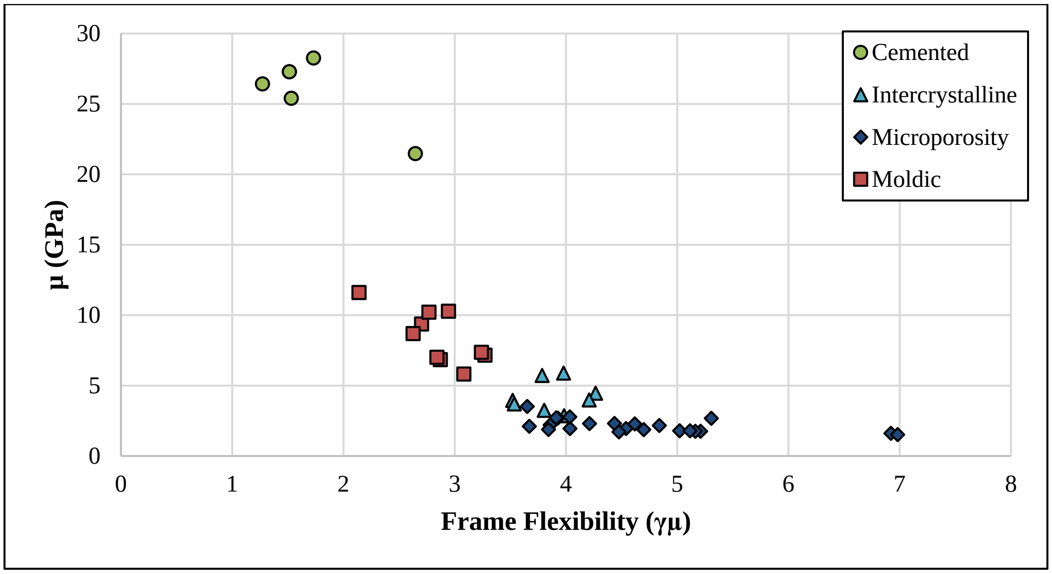

Figure 35. Diagram with frame flexibility factors (γ_μ) versus shear modulus (μ) and pore types identified.

Dependent on the pore structure and porosity, the f parameter describes the stiffness (f) and rigidity (f_μ) of the rock frame under deformation (Sun, 2004). Lower acoustic wave velocities, like in rocks with microporosity and intercrystalline porosity, are associated with lower frame stiffness/rigidity values. These lower values are characteristic of rocks that can deform easily under compression and shear motion. Knowing this, it is expected that higher stiffness (f) and rigidity (f_μ) values correlate with higher bulk and higher shear moduli.

An important part of Sun's model (2000, 2004) is the gamma ratio (Equation 4.28), which quantifies the shear deformation in relation to compressibility. This is essential in explaining why it's possible to have two different rocks with two different pore shapes, but the same frame compressibility – they may have a different resistance to shear motion (Sun, 2004). Using the data provided and appropriate equations, the gamma ratio was determined and plotted against porosity (Figure 36). The average gamma ratio is 0.8386 for the Bahamian samples. The majority of the samples cluster around the average, but some high velocity samples deviate farther away from the average (Figure 36). An average gamma ratio is useful in determining a pseudo-shear wave velocity (Vs) from a sonic (Vp) log where the Vs is not available (Sun, 2004).

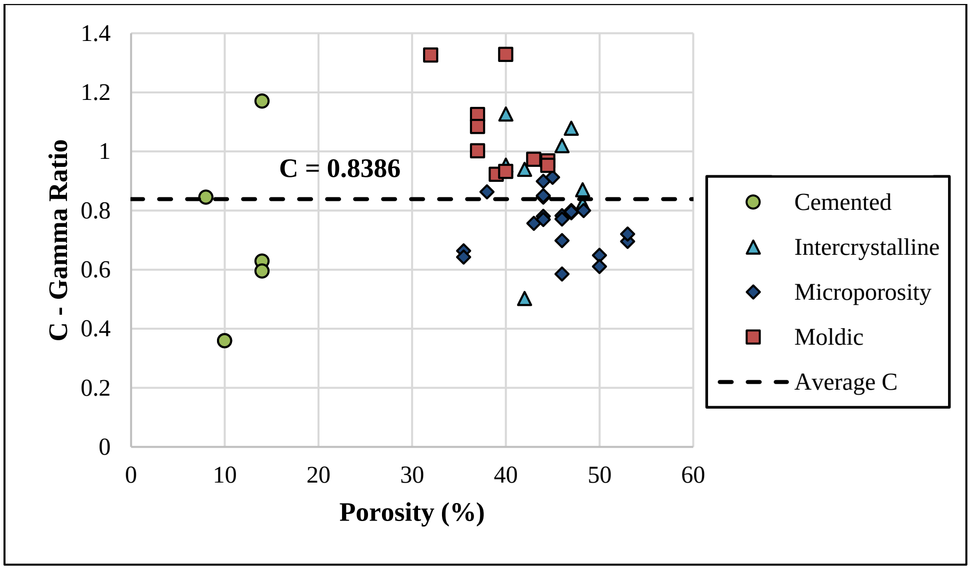

Figure 36. Gamma ratio versus porosity with C = 0.8386 as the average gamma ratio for the samples. The samples cluster around the average gamma ratio line (dashed line).

When the gammas ratio is compared to the velocity ratio, Vp/Vs, the same high velocity samples correspond to either very high or very low-end member velocity ratios (Figure 37). Using Figure 37, high acoustic velocity ratios correlate with high porosities with low permeabilities (e.g. some moldic porosity and microporosity).

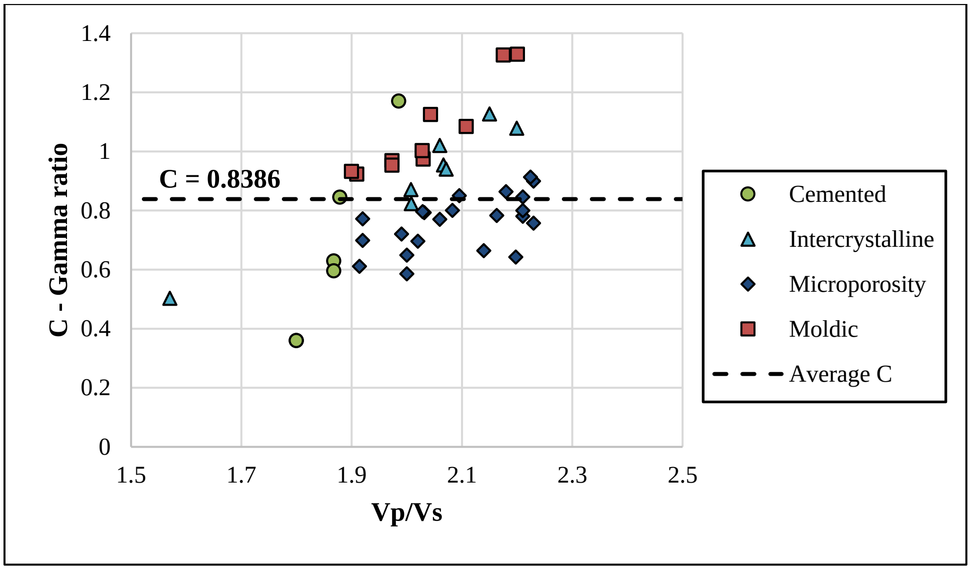

Figure 37. Gamma ratio versus the velocity ratio (Vp/Vs). There is a general cluster around the gamma ratio average, C = 0.8386 line.

4.6 Pore Space Stiffness Model and its Relation to Frame Flexibility

The pore space stiffness ($K_ø$) describes the rock's compressibility variations at a given porosity, as $K_ø$ is independent of porosity, and pore type effect on effective moduli (Baechle, 2009). Pore space stiffness ($K_ø$) was determined by Baechle (2009) to quantify carbonate rock variations in velocity at a given porosity. Pore stiffness is the inverse of the rock space compressibility at a constant pore pressure (Russell and Smith, 2007). The equation for the dry-rock compressibility at a constant pore pressure is (Mavko and Mukerji, 1995):

$$\frac{1}{K_{dry}} = \frac{1}{K_m} + \frac{\emptyset}{K_\emptyset} \tag{4-29}$$

where $K_\emptyset$ is the pore space stiffness, K_m is the mineral bulk modulus, K_{dry} is the dry rock bulk modulus, and $\emptyset$ is the porosity. This equation is the basis of Gassmann's fluid substitution equation as it is the link between the dry and fluid-saturated moduli. With a known porosity and mineral bulk modulus, the pore space stiffness can be derived by calculating K_{dry} using the acoustic velocities:

$$K_{dry} = ({V_p}^2 - \frac{4}{3}{V_s}^2)\rho \tag{4-30}$$

where K_{dry} is the dry rock bulk modulus, V_p is the P-wave or compressional wave velocity, V_s is the S-wave or shear wave velocity, and ρ is the density. Knowing this, the equation for $K_\emptyset$ is:

$$K_\emptyset = \left[\frac{K_m - K_{dry}}{\emptyset K_m K_{dry}}\right]^{-1} \; or \; \left[\frac{K_m - (({V_p}^2 - \frac{4}{3}{V_s}^2)\rho)}{\emptyset K_m(({V_p}^2 - \frac{4}{3}{V_s}^2)\rho)}\right]^{-1} \tag{4-31}$$

where $K_\emptyset$ is the pore space stiffness, K_m is the mineral bulk modulus, K_{dry} is the dry rock bulk modulus, $\emptyset$ is the porosity, V_p is the P-wave or compressional wave velocity, V_s is the S-wave or shear wave velocity, and ρ is the density.

When $K_\emptyset$ is plotted against porosity (Figure 38), it shows high pore stiffness values for low porosity pore types like cemented and moldic pores. The lowest $K_\emptyset$ values are shown by microporosity pores. Similarly, the velocity-pore stiffness crossplot (Figure 39), shows a positive trend with high velocities having high $K_\emptyset$ values. The high $K_\emptyset$ values occur in cemented pores that have the highest velocities, whereas the opposite is true for microporosity pores that have both the lowest velocities and $K_\emptyset$ values.

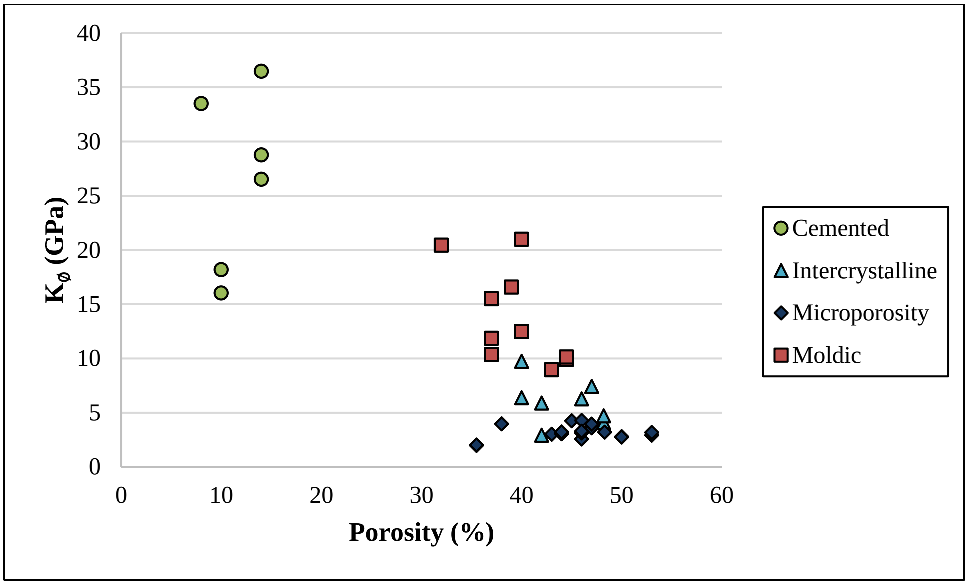

Figure 38. Pore space stiffness relative to porosity. $\boldsymbol{K_{\emptyset}}$ displays a general decreasing trend with increasing porosity.

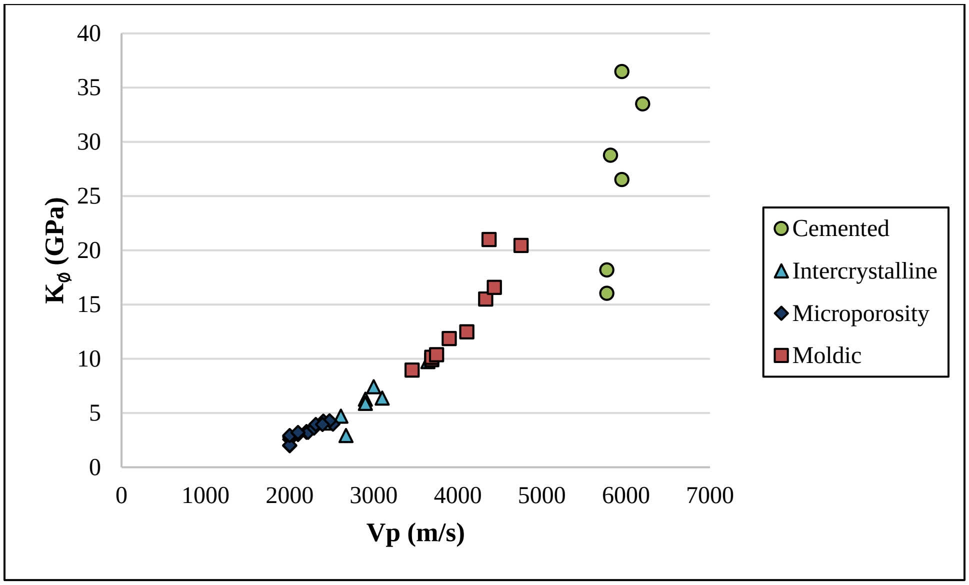

Figure 39. Pore space stiffness relative to compressional wave velocity (Vp). $\boldsymbol{K_{\emptyset}}$ displays a general increasing trend with increasing velocity.

The ratio of pore space stiffness over mineral bulk modulus (k), was introduced to quantify the velocity derivations at a given porosity Baechle (2009). The normalized bulk modulus-porosity diagram (Figure 40) shows values with constant k values of 0.05, 0.1, and 0.2. These k values create trend lines, which allows normalized constant pore space stiffness values to be linked to end member carbonate pore types. The equation for the normalized bulk modulus is:

$$\frac{K_d}{K_m} = \frac{1}{1 + \frac{\emptyset}{k}} \tag{4-32}$$

where

$$k = \frac{K_\emptyset}{K_m} \tag{4-33}$$

where;

K_d – normalized bulk modulus

K_m – mineral bulk modulus

$K_\emptyset$ – pore space stiffness

$\emptyset$ – porosity

k – ratio of pore space stiffness over mineral modulus

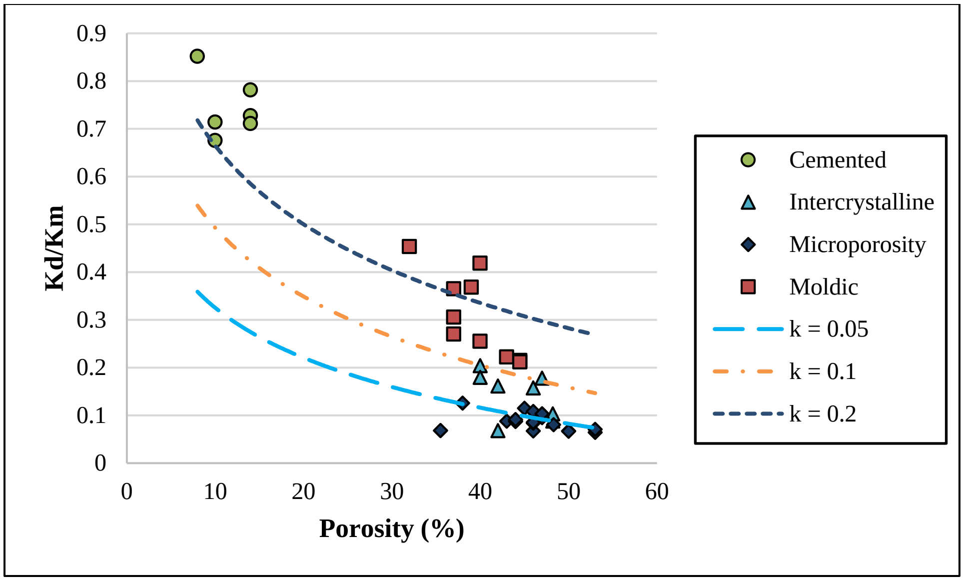

Figure 40. Normalized bulk modulus versus porosity crossplot with constant pore stiffness ratio (k) trend lines representing a nonlinear relationship between pore space stiffness and specific pore types. The determined correlations is k = 0.2 matches moldic, k = 0.1 matches intercrystalline, k = 0.05 matches microporosity, and cemented pores do not follow a trend.

Frame flexibility factors calculated from the Sun (2000) model show that the more flexible the rock's frame is, then for a given porosity, the γ and γ_μ values are larger. The frame flexibility factors are independent of porosity (Mammadova, 2011). Sun (2000) determined a relation between dry bulk modulus to the compressibility of the mineral matrix through γ (frame flexibility factor), based on the derivation of the extended Biot (1956) theory:

$$K_d = K_m(1-\emptyset)^\gamma \qquad \textbf{(4-34)}$$

Using Equations 4.30 and 4.35, a relation between $K_\emptyset$ and γ is determined:

$$K_\emptyset = \frac{\emptyset {K_m}^2(1-\emptyset)^\gamma}{K_m(1-(1-\emptyset)^\gamma)} \qquad \textbf{(4-35)}$$

Figure 41 displays the pore space stiffness increasing with decreasing frame flexibility factor at a given porosity. Low porosity, high density, cemented pores have higher value pore stiffness due to a low flexibility (or better coupling of grains) in the rock with gammas values between 2 and 4. These high-velocity samples between gamma values 2 and 4, are shallow water platform and reefal deposits (Mammadova, 2011). Microporosity and intercrystalline porosity, show gamma values between 3 and 6.

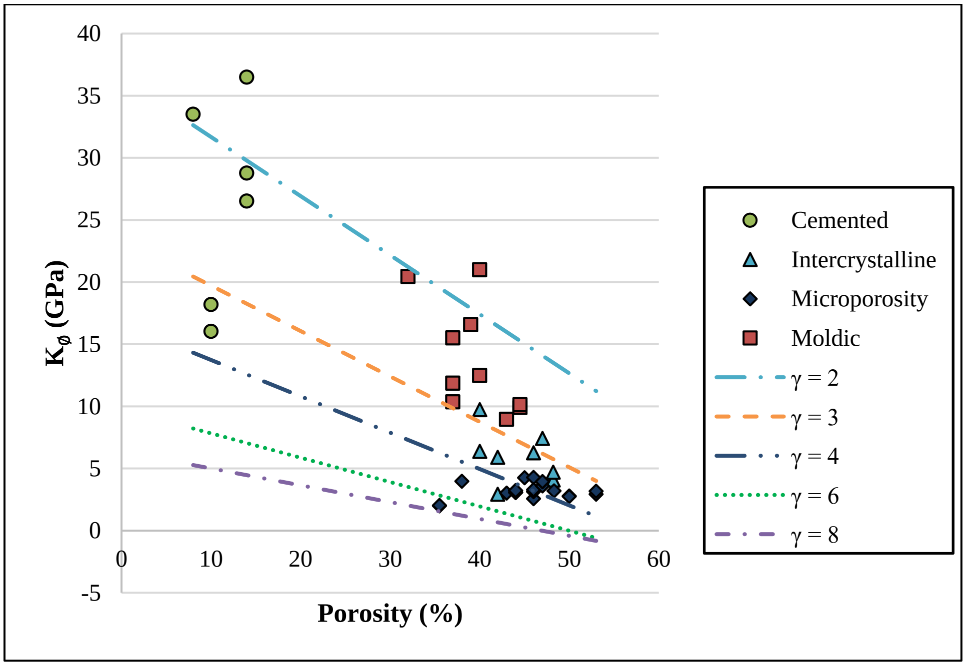

Figure 41. Pore space stiffness versus porosity with respect to constant gamma values, γ = 2, 3, 4, 6, and 8. General trend shows high gamma values correlating with lower pore space stiffness of the rock.

The pore space stiffness versus the frame stiffness factor diagram (Figure 42) depicts a good correlation of 0.96. Microporosity, intercrystalline, and moldic porosities cluster at the lower left of the best-fit curve. High rigid framework samples with low permeabilities, cemented rocks, are clustered around the upper right of the best-fit curve. Densely cemented pores with little to no permeabilities and low porosity, fall off of the general trendline (Mammadova, 2011).

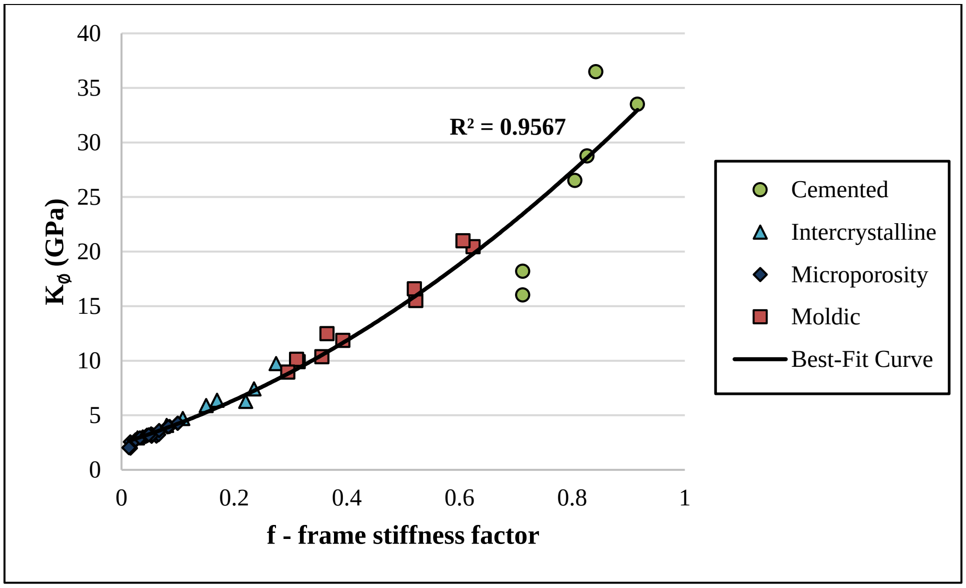

Figure 42. Crossplot of frame stiffness factor (f) with pore space stiffness (K_{ϕ}). Few samples of densely cemented, low porosity and low permeability rocks fall out of the general trendline.

4.7 Conclusions

In this chapter, various rock physics models were introduced and analyzed through their application to Clino and Unda core samples. Starting with Wyllie's time-average equation, the inaccuracy and underestimation of velocities, is due to the fact that Wyllie's equation does not account for velocity variations in carbonate pore types and diagenetic textures. Looking at the Voigt, Reuss, and VRH equations, the model produced displays the Reuss model as the lower bound, Voigt as the upper bound, and VRH as the average. The VRH model is used in this research. The Gassmann equation is used for fluid substitution, although, the assumptions with Gassmann's equation make its applicability to carbonate rocks not well understood. The remainder of this chapter focused on the pore size and pore type effect on velocity and elastic moduli.

The frame stiffness factors (f) of Sun's model are explicit functions of porosity, and it is assumed that γ and γ_μ are independent of porosity. The γ parameters known as the frame flexibility factor, under deformation, characterize the flexibility of the rock frame due to the presence of pore structures. The frame stiffness factors describe the stiffness and rigidity of the rock frame. Generally, higher γ values are related to less grain contacts and grain coupling, but due to diagenesis altering the rock to create special textures that result in high pore-connectivity and rigid rock frame with better grains contacts, this may result in lower γ values. Samples with lower frame flexibility factors have high acoustic wave velocities. Samples with the frame flexibility factors (γ, γ_μ) less than 4 are rocks with moldic porosity. Samples with flexibility factors greater than 4 are usually sucrosic dolomites with intercrystalline porosity, microporosity rocks with high concentrations of lime mud, or highly cemented rocks. Highly cemented, low porosity, high velocity samples show the lowest frame flexibility values, whereas high porosity, low velocity microporosity samples show the highest frame flexibility values. From lowest to highest frame flexibility factor values, the order of the pore types is cemented, moldic, intercrystalline, and microporosity pores. Higher value flexibility factors, like those present in microporosity and intercrystalline pores, are contributed to a lack of cementation, resulting in an unconnected grain fabric. Lower frame flexibility values, like in moldic pores, are due to a rigid, solid framework and their level of grain connectivity. Overall, the relationship is low frame flexibility factor values are associated with low porosities, high velocities, high bulk modulus, and high shear modulus. The opposite is true for low frame flexibility factor values, they are associated with high porosities, low velocities, low bulk modulus, and low shear modulus.

Pore space stiffness ($K_\emptyset$) describes the rock's compressibility variations at a given porosity, as it is independent of porosity, and pore type effect on moduli. $K_\emptyset$ increases with decreasing frame flexibility factor at a given porosity. The high $K_{\emptyset}$ values are in cemented pores that have the highest velocities, whereas the opposite is true for microporosity pores that have both the lowest velocities and $K_{\emptyset}$ values. Low porosity, high density, cemented pores have higher value pore stiffness due to a high flexibility (or better coupling of grains) in the rock with gammas values between 2 and 4. These high-velocity samples between gamma values 2 and 4, are shallow water platform and reefal deposits. Microporosity and intercrystalline porosity, show gamma values between 3 and 6. Gamma ratio quantifies the shear deformation in relation to compressibility.

5. INFLUENCE OF PORE TYPES ON CO_2 SUBSTITUTION

5.1 Introduction

The previous chapters discussed previous work on this research, the study area and dataset, the geological analysis of acoustic properties, and rock physics models. The acoustic velocities, porosities, permeability, density, bulk and shear moduli, and pressure analysis were analyzed for the carbonate rock samples of the Bahamas. The rock physics models used in the previous chapter included Wyllie's time average equation, Voigt-Reuss-Hill bounds, Gassmann fluid substitution, the Sun Model, and pore stiffness model. The previous results for the rock physics models are described in section 4.7 of this thesis.

There are three phases of oil production: primary, secondary, and tertiary. Primary oil recovery consists of hydrocarbons that naturally rise up the wellbore by natural pressure or gravity, or combined with the use of artificial lift devices, like pump jacks, to bring oil to the surface. Primary recovery only produces about 10% of a reservoir's original oil in place (OOIP) (U.S. Department of Energy, 2018). Secondary recovery techniques use water or gas injection to displace the oil, driving it to a production wellbore. Secondary recovery results in 20% to 40% OOIP recovery, meaning if only primary and secondary recovery methods are used, up to 75% of the oil may remain unproduced (U.S. Department of Energy, 2018). Tertiary recovery, also known as Enhanced Oil Recovery (EOR), further increases oil production which can lead to a recovery of ultimately 60% or more (U.S. Department of Energy, 2018). EOR techniques can be sub-divided into three major categories: thermal recovery, chemical injection, and gas injection. Accounting for over 40% of EOR production, primarily in California, thermal techniques involve the introduction of heat to thin the oil and enhance its ability to flow through the reservoir (U.S. Department of Energy, 2018). This heat is often an injection of steam. Chemical injection techniques involve either the use of polymers (long-chained molecules) to increase the effectiveness of waterflood, or the use of surfactants to help lower the surface tension that prevents oil from flowing through a reservoir (U.S. Department of Energy, 2018). Chemical injections comprise of about 1% of EOR production, due to high costs and for some situations, an unpredictability of its effectiveness. Gas injection, consisting of nearly 60% of EOR production, uses gases that expand to push additional oil to a production wellbore, or other gases that dissolve in the oil, lowering its viscosity to improve its flow rate. Gases used in gas injection consist of natural gas, nitrogen, or carbon dioxide (CO_2). The most popular method is CO_2 EOR, which originally used naturally occurring CO_2 deposits, now use CO_2 developed as byproducts from industrial applications, like natural gas processing, fertilizer, ethanol, and hydrogen plants in locations where reservoirs with naturally occurring CO_2 are not available. The U.S. Department of Energy suggests the implementation of EOR techniques, specifically the injection of CO_2, could increase the amount of oil recovered therefore, decreasing the country’s dependence on foreign oil.

Using the Gassmann fluid substitution model, this chapter will explain the influence of pore types on the velocities, elastic moduli, and frame flexibility after CO_2 flooding. The results from the previous chapters (water-saturated rock), new results from a CO_2 gas substitution, and CO_2 liquid substitution will be compared to the live-oil fluid substitution calculations. Live oil is defined by Schlumberger as oil containing dissolved gas in solution, that may be released from solution at surface conditions, whereas dead oil is oil containing no dissolved gas. Therefore, dead oil refers to the state of produced crude oil at atmospheric conditions. Oil existing in a reservoir under “dead” conditions is difficult to produce, as the dissolved gases help increase fluid mobility.

5.2 Method

All measurements from the Bahamas Drilling Project were determined on water-saturated miniplug samples at different effective pressures. Theoretically, all carbonate rocks are initially saturated with oil and the density and elastic moduli of both oil and new rock are then computed. Later on, carbonate rocks are saturated with the new fluid, which in this study is CO_2 in liquid and gas phase. The new densities and elastic moduli are computed after the simulated CO_2 flooding.

Using the calculated frame bulk modulus as previously described (Equation 4.30), a new bulk modulus was calculated for each fluid and then a new P-wave velocity was determined. This was done by determining the K_f(GPa) for each fluid (using the appendices of Mavko and Mukerji (1995)) to calculate a new effective bulk modulus using the equation:

$$K_{Gass} = K_{dry} + \frac{\left(1 - \frac{K_{dry}}{K_m}\right)^2}{\frac{\emptyset}{K_{fl}} + \frac{1-\emptyset}{K_m} - \frac{K_{dry}}{{K_m}^2}} \qquad \textbf{(5-1)}$$

and upon calculating a new K for the fluid-saturated rock, a new P-wave velocity was calculated,

$$V_{p_{Gass}} = \sqrt{\frac{K_{Gass} + \left(\frac{4}{3}\right)\mu}{\rho}} \qquad \textbf{(5-2)}$$

where;

K_{Gass} – Gassmann-predicted bulk modulus (GPa),

K_{dry} – dry bulk modulus (GPa),

K_m – bulk modulus of the matrix (GPa),

K_{fl} – bulk modulus of the fluid (GPa),

$\emptyset$ – porosity;

$V_{p_{Gass}}$ – Gassmann-predicted P-wave velocity (m/s),

ρ – density (GPa),

μ – shear modulus (GPa),

This is all completed using the modified Biot-Gassmann Equation (Gassmann, 1951; Biot, 1956) for fluid substitution modeling:

$$\frac{1}{C - C_m} = \frac{1}{\bar{C} - C_m} + \left(\frac{1}{C_{fl} - C_m}\right)\frac{1}{\emptyset} \tag{5-3}$$

where C is the compressibility of fluid-saturated rock, $\bar{C}$ is the compressibility of the dry rock frame, C_m is the compressibility of the mineral matrix, C_{fl} is the compressibility of the pore fluid, $\emptyset$ is the porosity of the rock. The compressibility of the rock is the inverse of the rock's bulk modulus at a constant pore pressure.

As previously described, the applicability of Gassmann's equation in carbonate rocks is not well understood, due to assumptions the Gassmann equations is derived on. A major assumption for the Gassmann equation is that the shear modulus is independent of the pore fluid content:

$$\mu_{sat} = \mu_{dry} \tag{5-4}$$

where μ_{sat} is the saturated shear modulus and μ_{dry} is the dry shear modulus. The reasoning behind this assumption is that since fluid theoretically has negligible resistance to shear change, the shear modulus for all fluids will be considered 0 GPa and therefore the velocity of the S-wave through a fluid will also be considered 0 m/s. Therefore, the results of the Gassmann equation is independent of the rock's shear modulus from the pore fluid type.

To find live-oil, Mavko and Mukerji (1995) equations were used. Knowing the API is 30 and G (gas gravity) is 0.6, the R_G (gas-oil ratio), density, Vp, and bulk modulus are calculated. For this study, T_0 (initial temperature) = 25°C, P_0 (initial pressure) = 0.1 MPa (~14.5 psi), T (final temperature) = 162.6°C, and P (final pressure) = 70 MPa (~10152.6 psi).

$$\rho_0 = \frac{141.5}{API + 131.5} \tag{5-5}$$

$$B_0 = 0.972 + 0.00038\left[1.4R_G\left(\frac{G}{\rho_0}\right)^{\frac{1}{2}} + T + 17.8\right]^{1.175} \tag{5-6}$$

$$\rho' = \frac{\rho_0}{B_0}(1 + 0.001R_G)^{-1} \tag{5-7}$$

$$\rho_G = (\rho_0 + 0.0012GR_G)/\,B_0 \tag{5-8}$$

$$\rho_P = \rho_G + (0.00277P - 1.71 \times 10^{-7}P^3)(\rho_G - 1.15)^2 + 3.49 \times 10^{-4}P \tag{5-9}$$

$$\rho = \rho_P/[0.972 + 3.81 \times 10^{-4}(T + 17.78)^{1.175}] \tag{5-10}$$

$$V_p = 2096\left(\frac{\rho'}{2.6 - \rho'}\right)^{\frac{1}{2}} - 3.7T + 4.64P + 0.0115\left[4.12\left(\frac{1.08}{\rho'} - 1\right)^{\frac{1}{2}} - 1\right]TP \tag{5-11}$$

$$K = \rho\left({V_p}^2\right) \text{ using Equations (5-6) for } \rho \text{ and (5-7) for } V_p \tag{5-12}$$

where;

ρ_0 - initial density,

API – American Petroleum Institute's oil gravity,

B_0 – oil formation volume factor,

R_G – maximum amount of gas that can be dissolved in an oil (gas-oil ratio),

G – gas gravity,

ρ' - pseudo-density,

ρ_G – true density of oil with gas (g/cc),

ρ_P –density corrected for pressure (g/cc),

ρ - actual density,

V_p – velocity in oil with gas,

K – bulk modulus in oil with gas,

T - temperature,

P – pressure.

Live-Oil	**T_0, P_0**	**T, P_0**	**T_0, P**	**T, P**
ρ (g/cc)	0.87	0.67	0.63	0.59
Vp (m/s)	1397.90	754.83	1043.47	1192.76
K (GPa)	1.31	0.36	0.64	1988.76

Table 3. Live-oil calculations, knowing the API is 30 and G (gas gravity) is 0.6, the R_G (gas-oil ratio), T_0 (initial temperature) = 25°C, P_0 (initial pressure) = 0.1 MPa (~14.5 psi), T (final temperature) = 162.6°C, and P (final pressure) = 70 MPa (~10152.6 psi).

The final T and P for live-oil were used to compare changes in CO_2 flooding, as a high pressure and high temperature with an API of over 22 in a reservoir, create good conditions for miscible CO_2 flooding. Miscible CO_2 flooding means both the injected CO_2 and oil mix completely inside the reservoir, reducing the interfacial tension and improving fluid mobility due to the low viscosity. The immiscible CO_2 flooding method means the CO_2 and oil do not mix, as the pressure is too low and the density is too high, causing a swelling in the oil that reduces the viscosity and increases fluid flow. Miscible CO_2 flooding is more popular in the oil industry.

The accuracy of fluid parameters, especially the properties of CO_2 in liquid and gas phase, affect the results of our substitution model. The CO_2 properties are estimated based on the

Wang et al. (1998) rock physics study that used the McElroy field and a commercially-sourced CO_2 with purity of >99.5% with critical temperature at 31°C (88°F) and pressure at 7.4 MPa (1070 psi) (Wang et al., 1998). Values higher than the critical pressure and below the critical temperature will be in liquid phase, and temperatures higher than the critical temperature will be in gas phase (Wang et al., 1998). Properties of CO_2 are very different from water or oil properties, for example at higher pressures, CO_2 density can reach the density of water, whereas the bulk modulus remains below that of water (Figure 43). The Vp of liquid CO_2 increases with increasing pore pressure, whereas the Vp of CO_2 in the gas phase decreases as pressure increases.

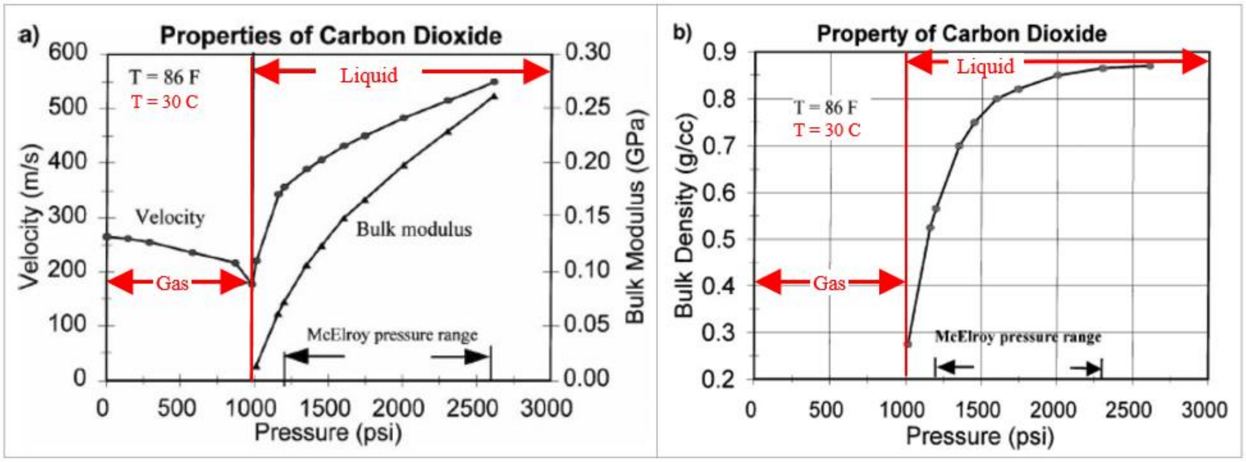

Figure 43. Properties of carbon dioxide (CO_2) at 30°C (86°F); (a) velocities (left y-axis), bulk moduli (right y-axis) versus pressure; (b) bulk density versus pressure (modified from Wang et al., 1998).

5.3 Results

Completing the method described in the methodology, the following fluid substitutions were completed: water-saturated, live-oil, CO_2 (gas), and CO_2 (liquid). The water-saturated rock properties will be used to compare the effects of pore types on CO_2 flooding as the original in-situ rock (the control variable). The live-oil properties that are determined will be used to determine the effect of CO_2 on velocities. For this thesis, we validate Gassmann's theory in carbonate rocks and its assumptions. With this, we theoretically saturate the initially water-saturated carbonate sample with live-oil, then using the same samples, the flooding with CO_2 both in liquid and gas phase is simulated.

5.3.1 Water-Saturated

This substitution is the control for all the fluid substitution models, as we have determined by the previous calculations of the Clino and Unda cores (Appendix C). We will be comparing the fluid substitutions to the water model, as it is the initial rock at an effective pressure of 8 MPa (~1160.3 psi). Table 3 shows the ranges of properties for this fluid substitution model.

This model was analyzed in section 4.5 of this thesis. The overall trends were that samples with lower frame flexibility factors have high acoustic wave velocities (Figures 28 and 29). When comparing Figure 28 to Figure 19 (where pore types are identified on a velocity-porosity diagram), samples with the frame flexibility factors (γ, γ_μ) less than 4 are rocks with moldic porosity. Samples with flexibility factors greater than 4 are usually sucrosic dolomites with intercrystalline porosity, microporosity rocks with high concentrations of lime mud, or highly cemented rocks.

In Figures 30 and 31 (frame flexibility versus velocity), highly cemented, low porosity, high velocity samples show the lowest frame flexibility values, whereas high porosity, low velocity microporosity samples show the highest frame flexibility values. From lowest to highest frame flexibility factor values, the order of the pore types is cemented, moldic, intercrystalline, and microporosity pores. Higher value flexibility factors, like those occurring in microporosity and intercrystalline pores, are contributed to a lack of cementation, resulting in an unconnected grain fabric (Mammadova, 2011). Lower frame flexibility values, like in moldic pores, are due to a rigid, solid framework and their level of grain connectivity.

The same relationship, previously mentioned, is present between elastic moduli, frame flexibility and pore types. Higher frame flexibility occurs in microporosity with low bulk and low shear modulus values, whereas lower frame flexibility is shown in cemented pores with high bulk and high shear modulus values (Figure 32, 33, 34, and 35). Overall, the relationship is low frame flexibility factor values are associated with low porosities, high velocities, high bulk modulus, and high shear modulus. The opposite is true for low frame flexibility factor values, they are associated with high porosities, low velocities, low bulk modulus, and low shear modulus.

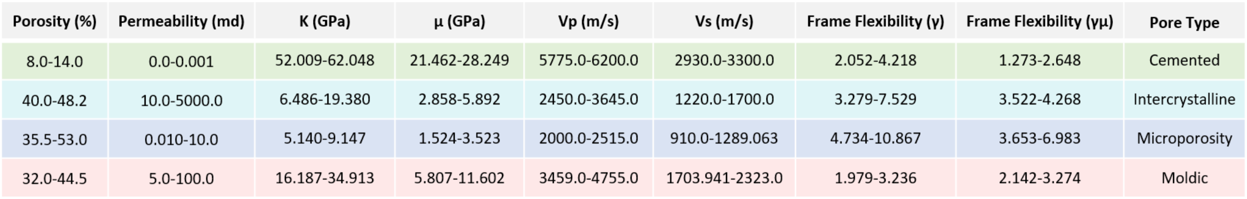

Porosity (%)	Permeability (md)	K (GPa)	μ (GPa)	Vp (m/s)	Vs (m/s)	Frame Flexibility (γ)	Frame Flexibility (γμ)	Pore Type
8.0-14.0	0.0-0.001	52.009-62.048	21.462-28.249	5775.0-6200.0	2930.0-3300.0	2.052-4.218	1.273-2.648	Cemented
40.0-48.2	10.0-5000.0	6.486-19.380	2.858-5.892	2450.0-3645.0	1220.0-1700.0	3.279-7.529	3.522-4.268	Intercrystalline
35.5-53.0	0.010-10.0	5.140-9.147	1.524-3.523	2000.0-2515.0	910.0-1289.063	4.734-10.867	3.653-6.983	Microporosity
32.0-44.5	5.0-100.0	16.187-34.913	5.807-11.602	3459.0-4755.0	1703.941-2323.0	1.979-3.236	2.142-3.274	Moldic

Table 4. Ranges of properties for a water-saturated carbonate rock, using Bahamian data.

5.3.2 Live-Oil-Saturated

To find the bulk modulus for the live-oil-saturated rock, $K_f \cong 1.70$ GPa was used to calculate a new effective bulk modulus (Appendix D). Previous calculations were used to calculate other variables for this fluid substitution, using the equations from Mavko and Mukerji (1995)’s Rock Physics Handbook.

The overall trends were that samples with lower frame flexibility factors have high acoustic wave velocities (Figure 44 and Figure 45). In Figure 46 (frame flexibility versus velocity), highly cemented, low porosity, high velocity samples show the lowest frame flexibility values, whereas high porosity, low velocity microporosity samples show the highest frame flexibility values. From lowest to highest frame flexibility factor values, the order of the pore types is cemented, moldic, intercrystalline, and microporosity pores. For frame flexibility versus Vs, the cemented pores have higher γ values than normal – in general, all the pore types appear to have the same frame flexibility factors (γ).

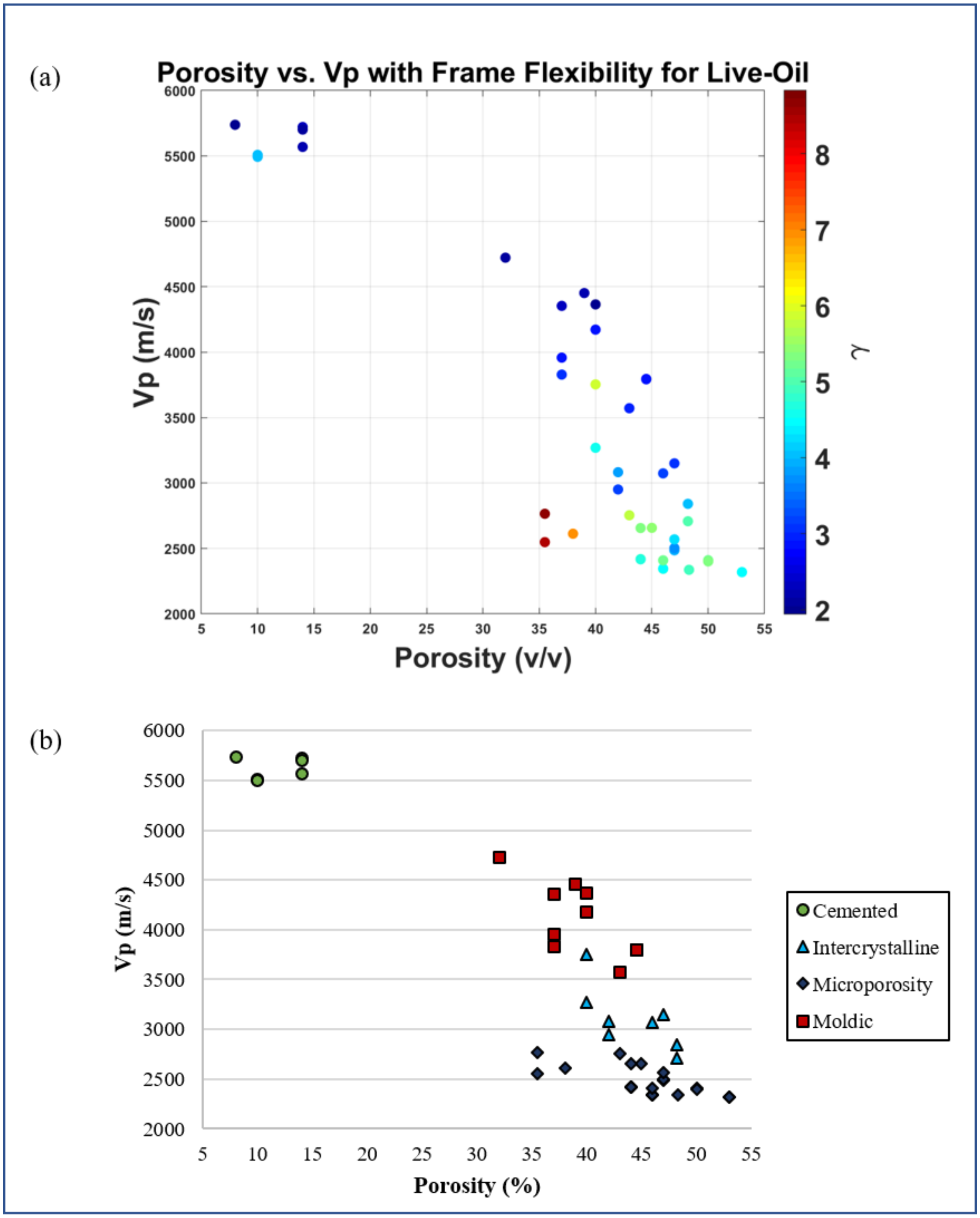

Figure 44. Vp-porosity crossplots for live-oil (a) includes a gradient for frame flexibility (γ). (b) diagram with pore types identified.

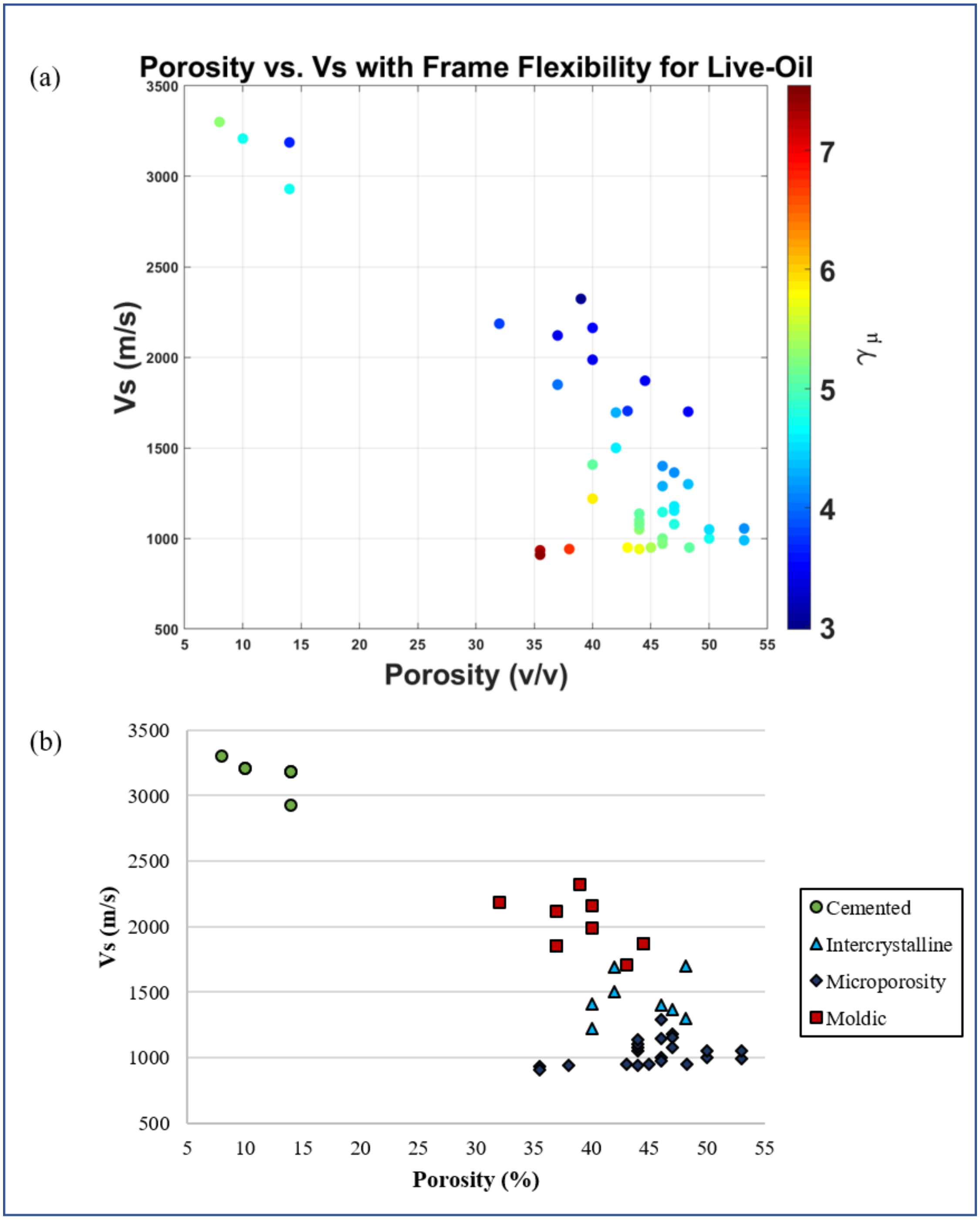

Figure 45. Vs-porosity crossplots for live-oil (a) includes a gradient for frame flexibility (γμ). (b) diagram with pore types identified.

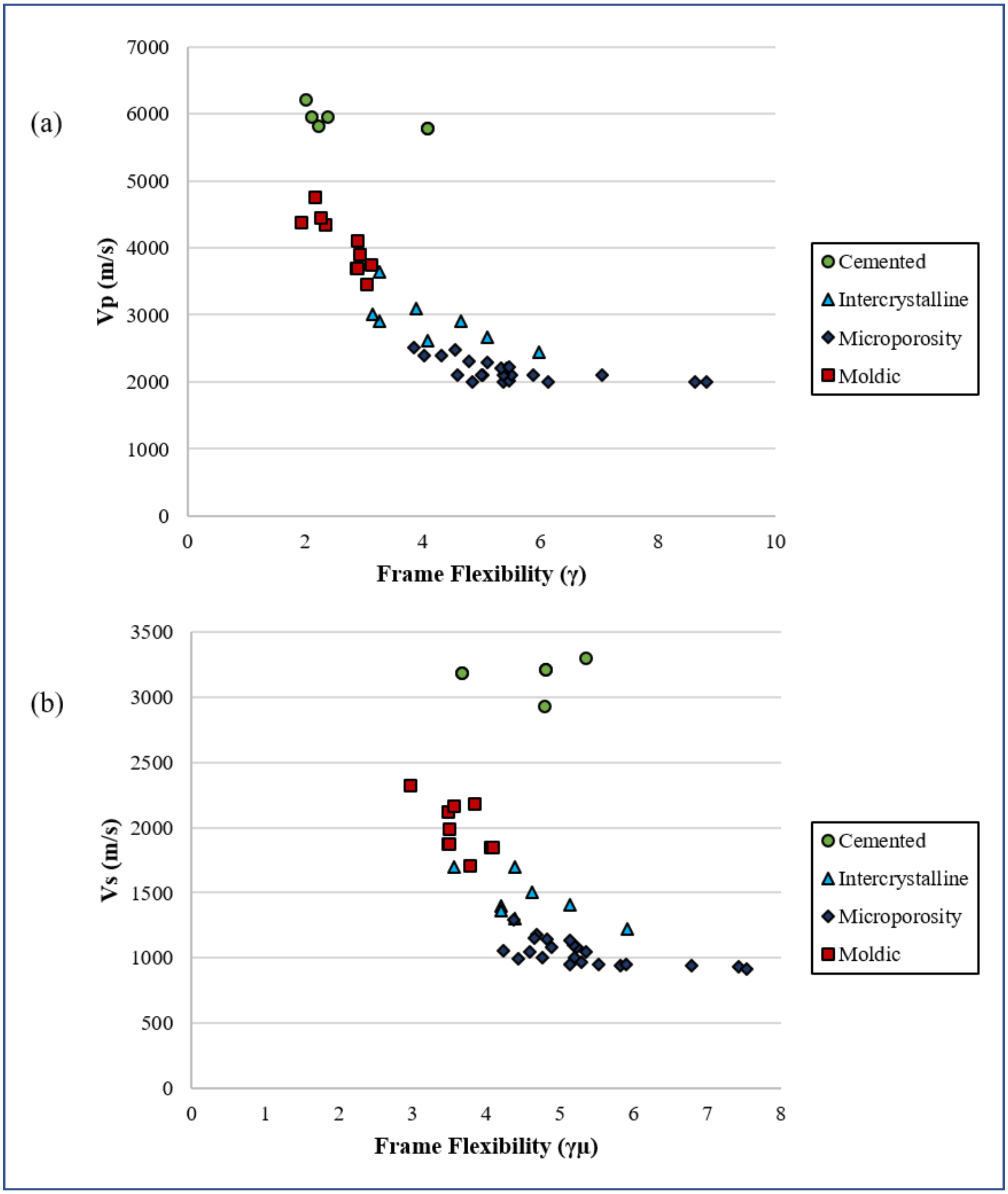

Figure 46. Diagram with frame flexibility factors (γ and γ_μ) versus velocities with pore types identified for live-oil (a) Vp velocity versus frame flexibility factors (γ), (b) Vs versus frame flexibility factors (γ_μ)

Higher frame flexibility is displayed in microporosity pores with low bulk and low shear modulus values, whereas lower frame flexibility occurs in cemented pores with high bulk and high shear modulus values (Figures 47 and 48). Overall, the relationship is low frame flexibility factor values are associated with low porosities, high velocities, high bulk modulus, and high shear modulus. The opposite is true for low frame flexibility factor values, they are associated with high porosities, low velocities, low bulk modulus, and low shear modulus. Table 4 lists the ranges of properties for a live-oil saturated carbonate rock using Bahamian data.

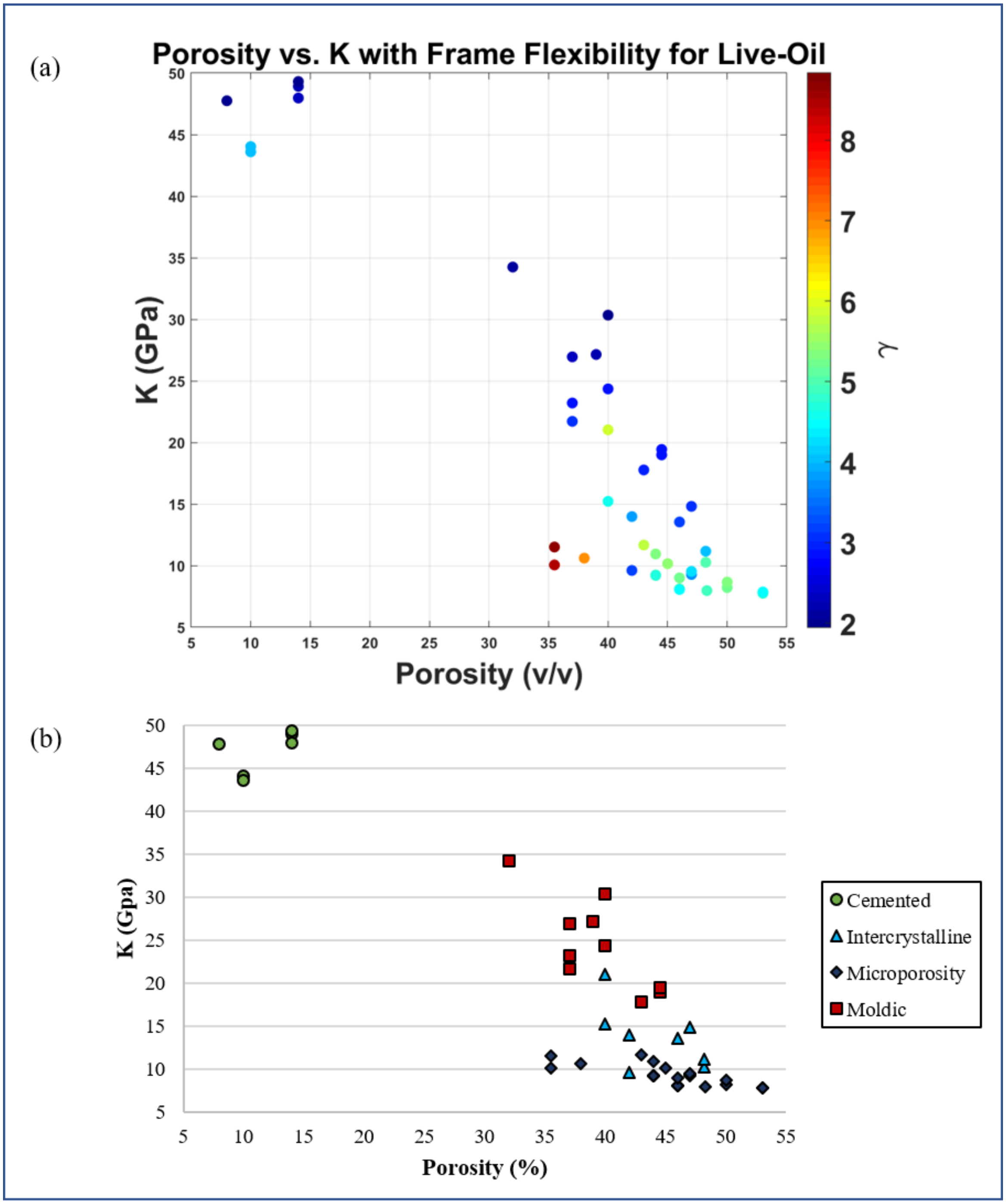

Figure 47. K-porosity crossplots for live-oil (a) includes a gradient for frame flexibility (γ). (b) diagram with pore types identified.

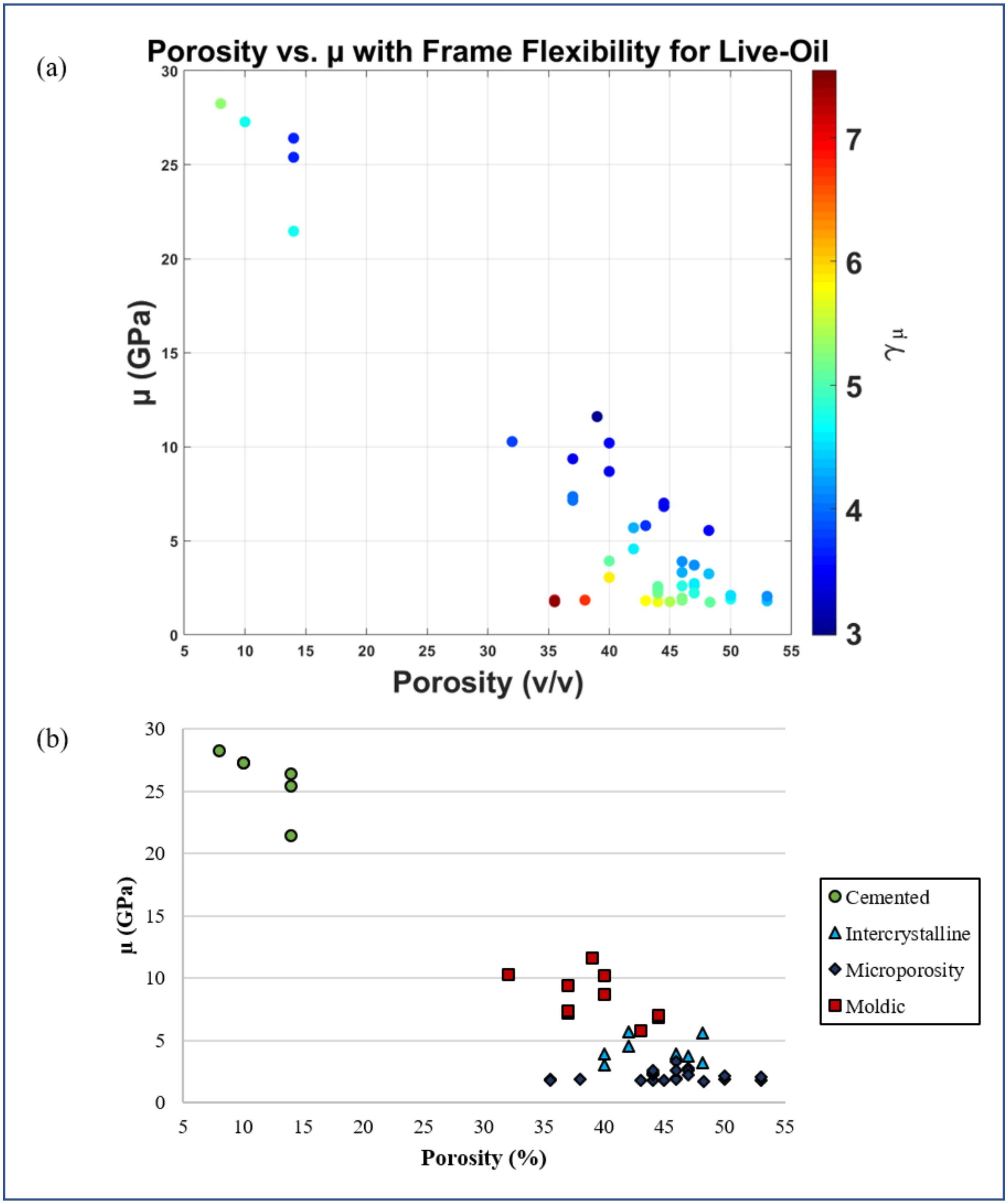

Figure 48. μ-porosity crossplots for live-oil (a) includes a gradient for frame flexibility (γμ). (b) diagram with pore types identified.

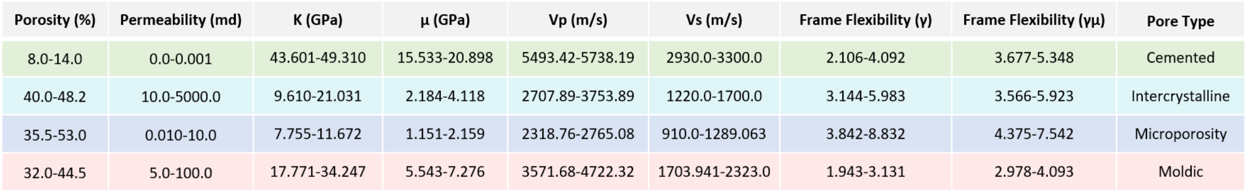

Porosity (%)	Permeability (md)	K (GPa)	µ (GPa)	Vp (m/s)	Vs (m/s)	Frame Flexibility (γ)	Frame Flexibility (γµ)	Pore Type
8.0-14.0	0.0-0.001	43.601-49.310	15.533-20.898	5493.42-5738.19	2930.0-3300.0	2.106-4.092	3.677-5.348	Cemented
40.0-48.2	10.0-5000.0	9.610-21.031	2.184-4.118	2707.89-3753.89	1220.0-1700.0	3.144-5.983	3.566-5.923	Intercrystalline
35.5-53.0	0.010-10.0	7.755-11.672	1.151-2.159	2318.76-2765.08	910.0-1289.063	3.842-8.832	4.375-7.542	Microporosity
32.0-44.5	5.0-100.0	17.771-34.247	5.543-7.276	3571.68-4722.32	1703.941-2323.0	1.943-3.131	2.978-4.093	Moldic

Table 5. Ranges of properties for a live-oil-saturated carbonate rock, using Bahamian data.

5.3.3 CO_2-Saturated (Gas Phase)

For the gas phase CO_2-saturated rock, $K_f = 0.02327$ GPa was used to calculate a new effective bulk modulus (Appendix E). This variable was determined using Mavko and Mukerji (1995)'s Rock Physics Handbook Appendix to find that 1000 psi or ~7 MPa pressure at 31°C was the gaseous phase for CO_2.

The overall trend for Vp is that samples with lower frame flexibility factors have high acoustic wave velocities (Figure 49), whereas Vs samples show lower frame flexibility factors with low wave velocity (Figure 50). In Figure 51a (frame flexibility versus Vp), highly cemented, low porosity, high velocity samples show the lowest frame flexibility values, whereas high porosity, low velocity microporosity samples show the highest frame flexibility values. In Figure 51b (frame flexibility versus Vs), highly cemented, low porosity, high velocity samples show the highest frame flexibility values, whereas high porosity, low velocity microporosity samples show the lowest frame flexibility values.

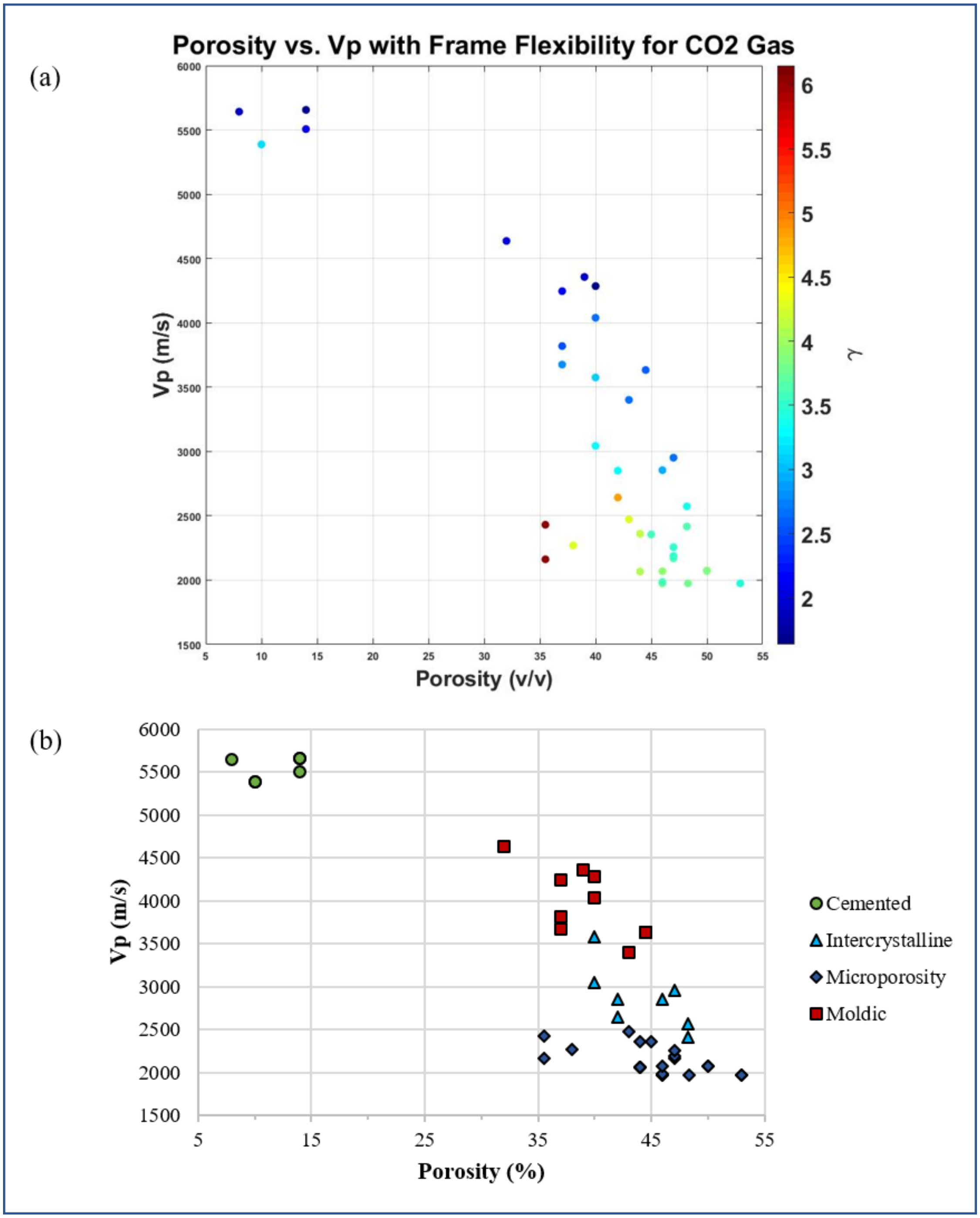

Figure 49. Vp-porosity crossplots for CO_2 gas (a) includes a gradient for frame flexibility (γ). (b) diagram with pore types identified.

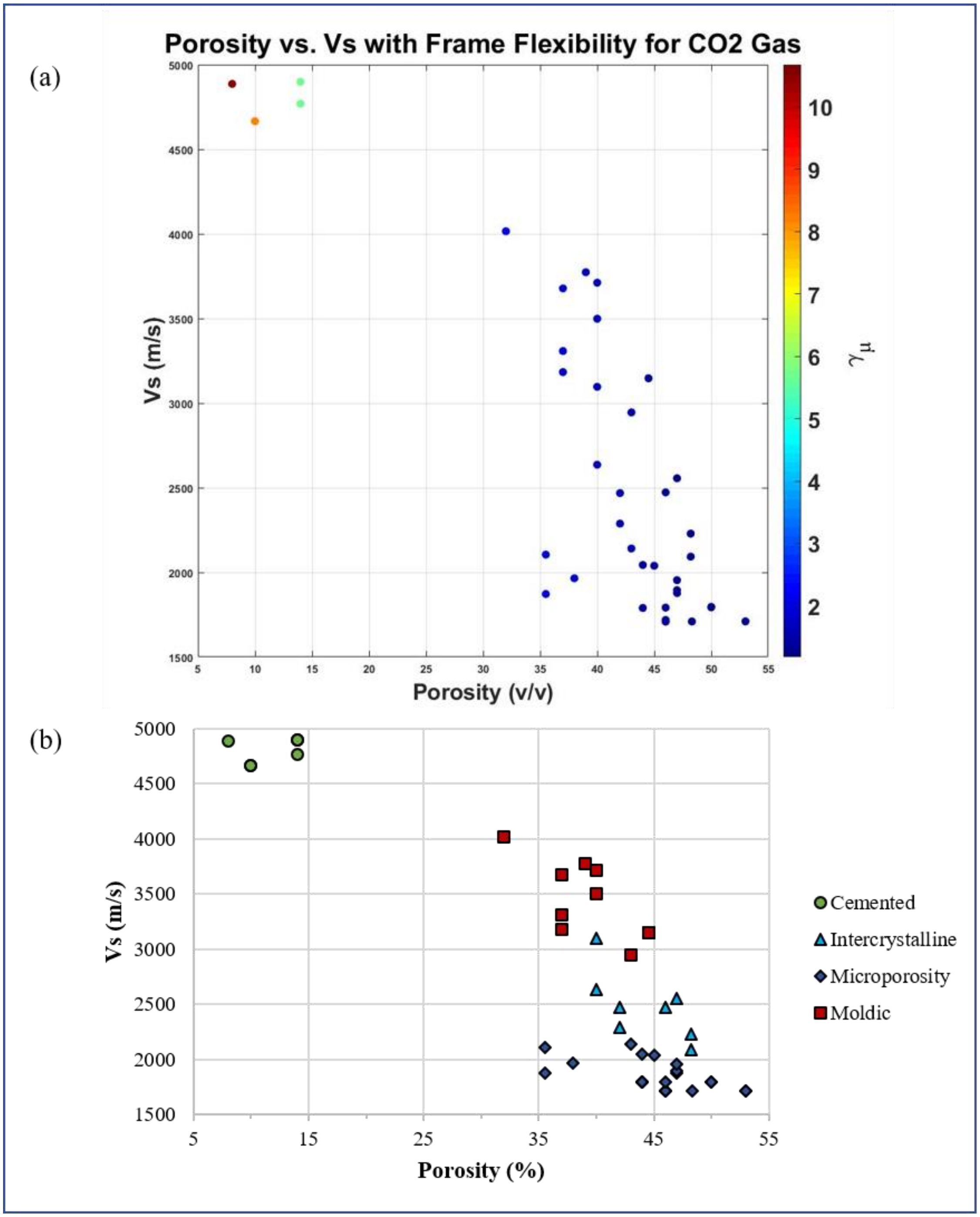

Figure 50. Vs-porosity crossplots for CO_2 gas (a) includes a gradient for frame flexibility (γμ). (b) diagram with pore types identified.

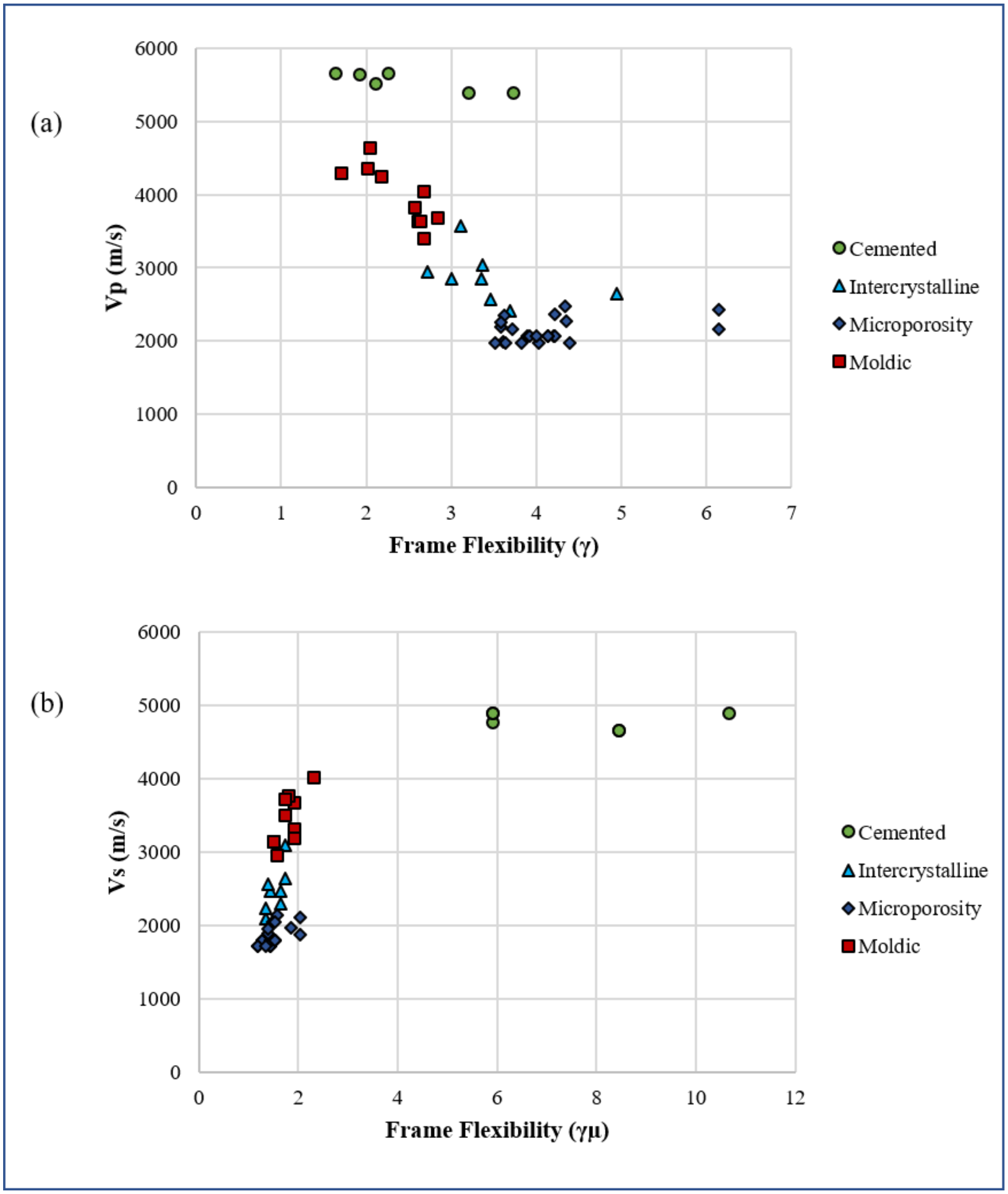

Figure 51. Diagram with frame flexibility factors (γ and γ_{μ}) versus velocities with pore types identified for CO_2 gas (a) Vp velocity versus frame flexibility factors (γ), (b) Vs versus frame flexibility factors (γ_{μ})

In microporosity pores with low bulk and shear modulus values, the flexibility factors are high for γ and low for γμ (Figures 52 and 53). The opposite is true for cemented pores. Overall, the relationship is low γ values are associated with low porosities, high velocities, high bulk modulus, and high shear modulus, whereas low γμ values are associated with high porosities, low velocities, low bulk and low shear moduli. Table 6 lists the ranges of properties for a CO_2 gas saturated carbonate rock using Bahamian data.

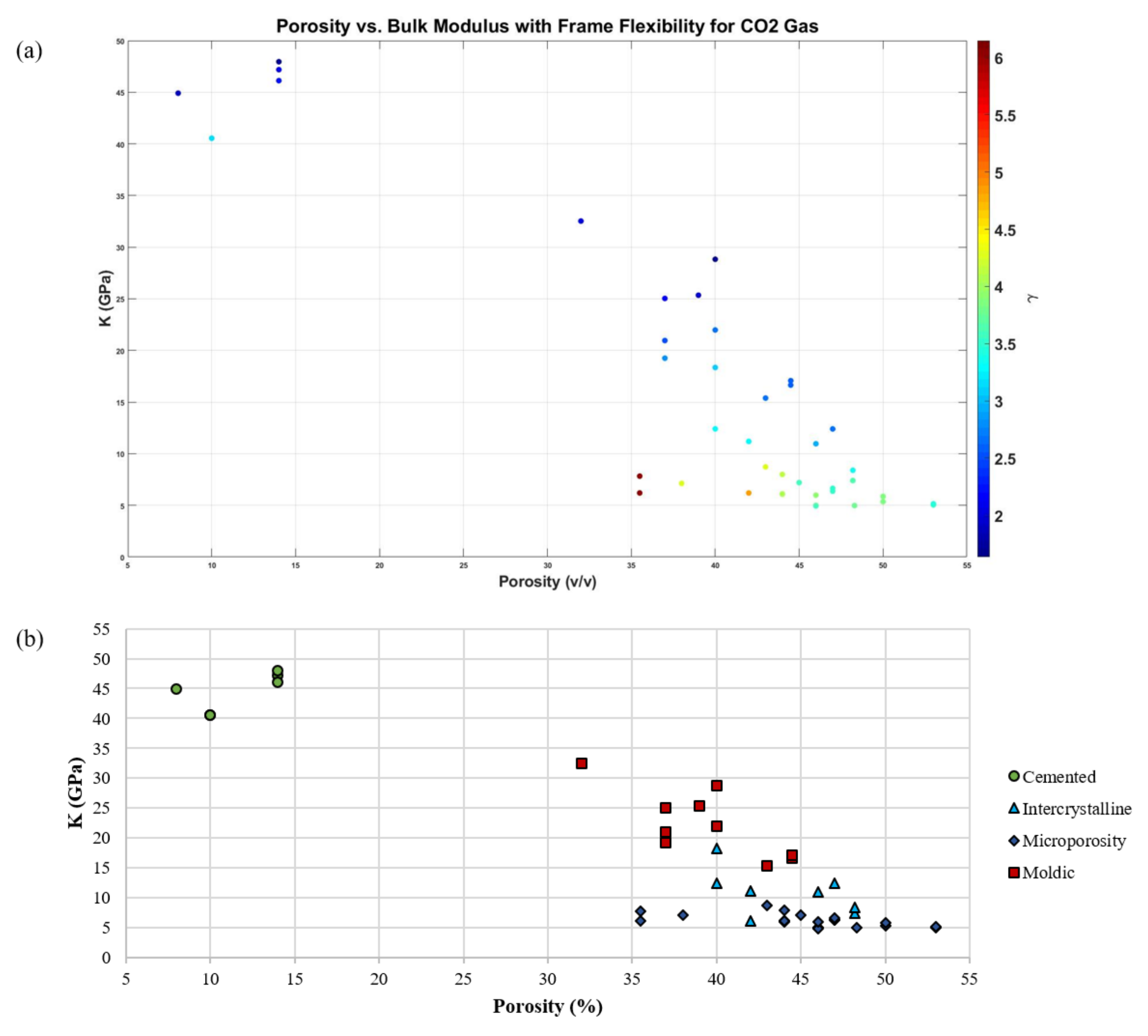

Figure 52. K-porosity crossplots for CO_2 gas (a) includes a gradient for frame flexibility (γ). (b) diagram with pore types identified.

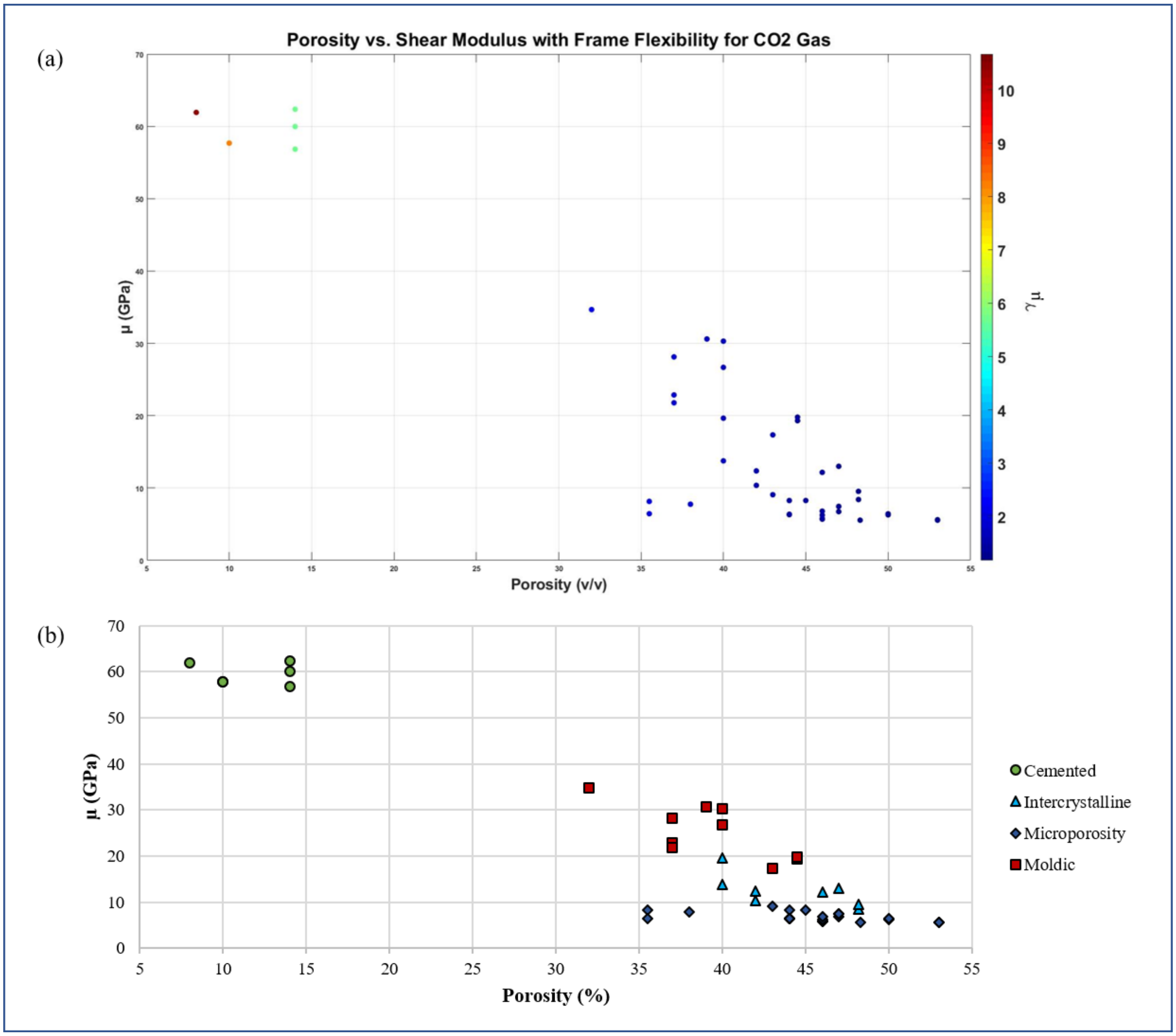

Figure 53. μ-porosity crossplots for CO_2 gas (a) includes a gradient for frame flexibility (γμ). (b) diagram with pore types identified.

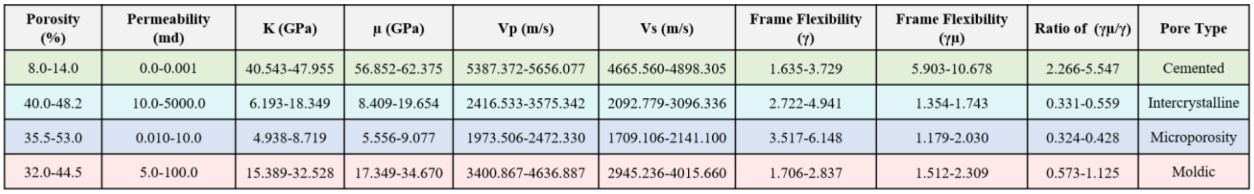

Porosity (%)	Permeability (md)	K (GPa)	µ (GPa)	Vp (m/s)	Vs (m/s)	Frame Flexibility (γ)	Frame Flexibility (γµ)	Ratio of (γµ/γ)	Pore Type
8.0-14.0	0.0-0.001	40.543-47.955	56.852-62.375	5387.372-5656.077	4665.560-4898.305	1.635-3.729	5.903-10.678	2.266-5.547	Cemented
40.0-48.2	10.0-5000.0	6.193-18.349	8.409-19.654	2416.533-3575.342	2092.779-3096.336	2.722-4.941	1.354-1.743	0.331-0.559	Intercrystalline
35.5-53.0	0.010-10.0	4.938-8.719	5.556-9.077	1973.506-2472.330	1709.106-2141.100	3.517-6.148	1.179-2.030	0.324-0.428	Microporosity
32.0-44.5	5.0-100.0	15.389-32.528	17.349-34.670	3400.867-4636.887	2945.236-4015.660	1.706-2.837	1.512-2.309	0.573-1.125	Moldic

Table 6. Ranges of properties for a CO_2 (gas)-saturated carbonate rock, using Bahamian data

5.3.4 CO_2-Saturated (Liquid Phase)

For the liquid phase CO_2-saturated rock, K_f = 0.31249 GPa was used to calculate a new effective bulk modulus (Appendix F). This variable was determined using Mavko and Mukerji (1995)'s Rock Physics Handbook Appendix to find that 2500 psi or ~17 MPa pressure at 31°C was the liquid phase for CO_2.

The overall trends were that samples with lower frame flexibility factors have high acoustic wave velocities (Figures 54 and 55). In Figure 56 (frame flexibility versus velocity), highly cemented, low porosity, high velocity samples show the lowest frame flexibility values, whereas high porosity, low velocity microporosity samples show the highest frame flexibility values. From lowest to highest frame flexibility factor values, the order of the pore types is cemented, moldic, intercrystalline, and microporosity pores. For frame flexibility versus Vs, the cemented pores have higher γ values than normal – in general, all the pore types appear to have the same frame flexibility factors (γ).

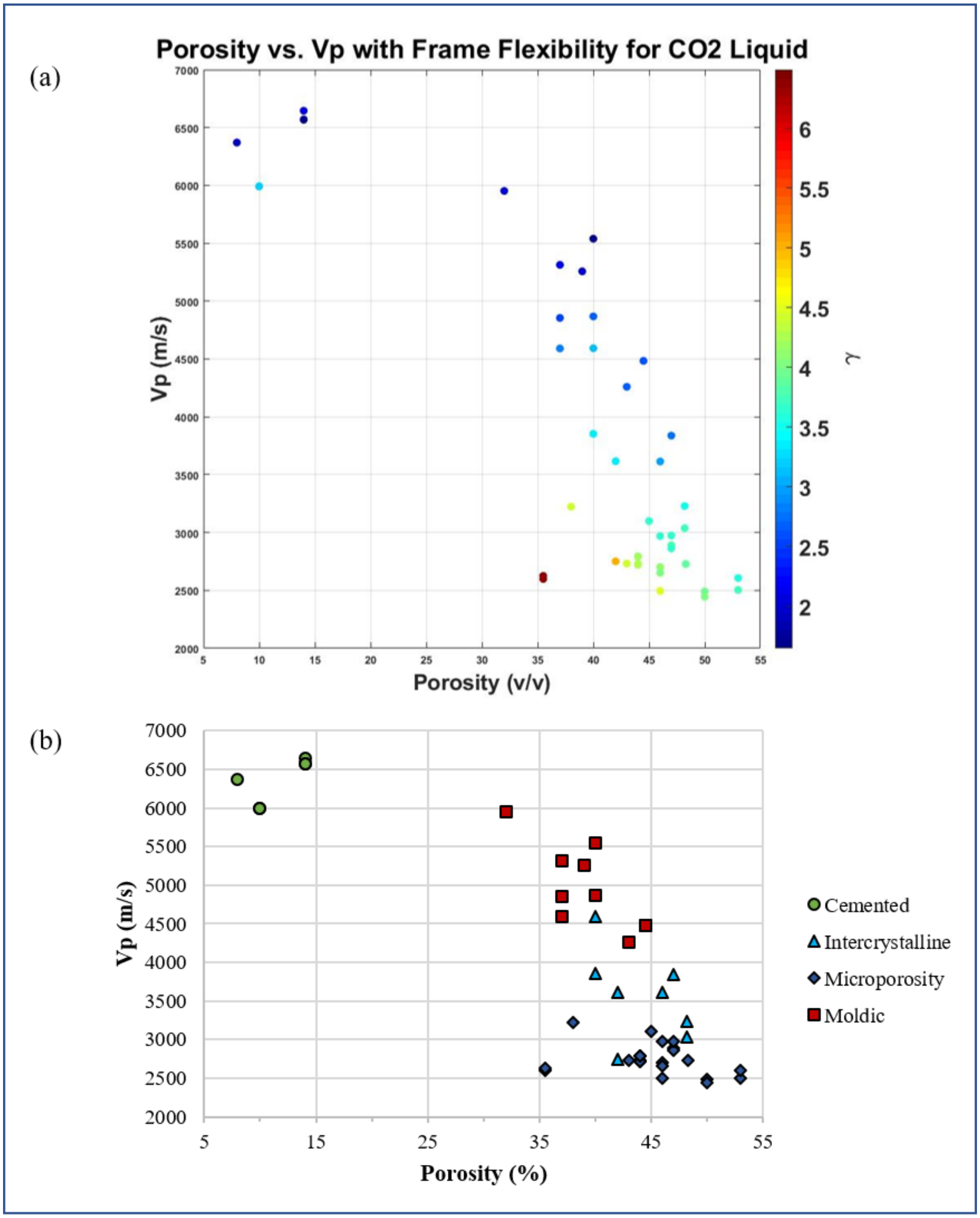

Figure 54. Vp-porosity crossplots for CO_2 liquid (a) includes a gradient for frame flexibility (γ). (b) diagram with pore types identified.

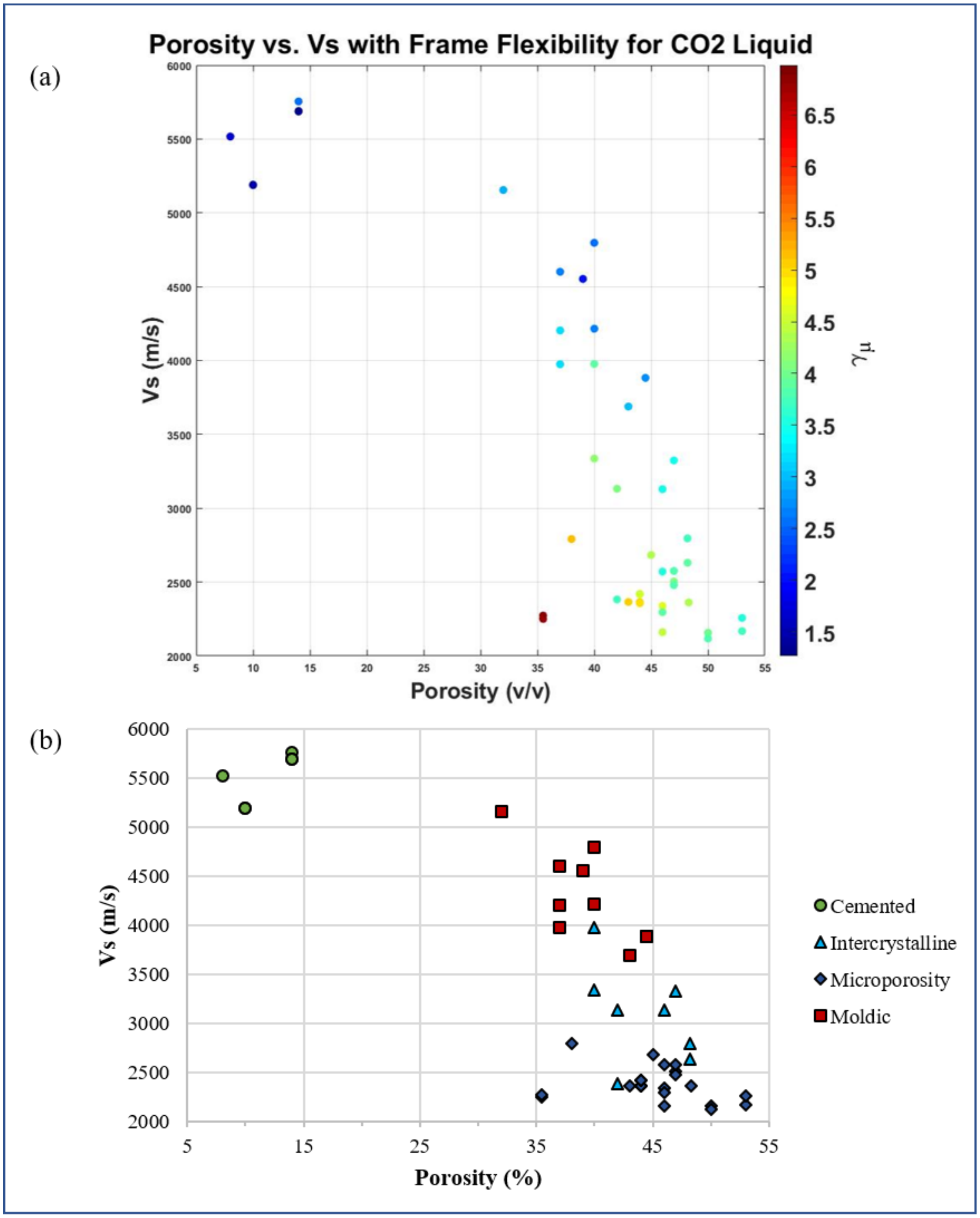

Figure 55. Vs-porosity crossplots for CO_2 liquid (a) includes a gradient for frame flexibility (γμ). (b) diagram with pore types identified.

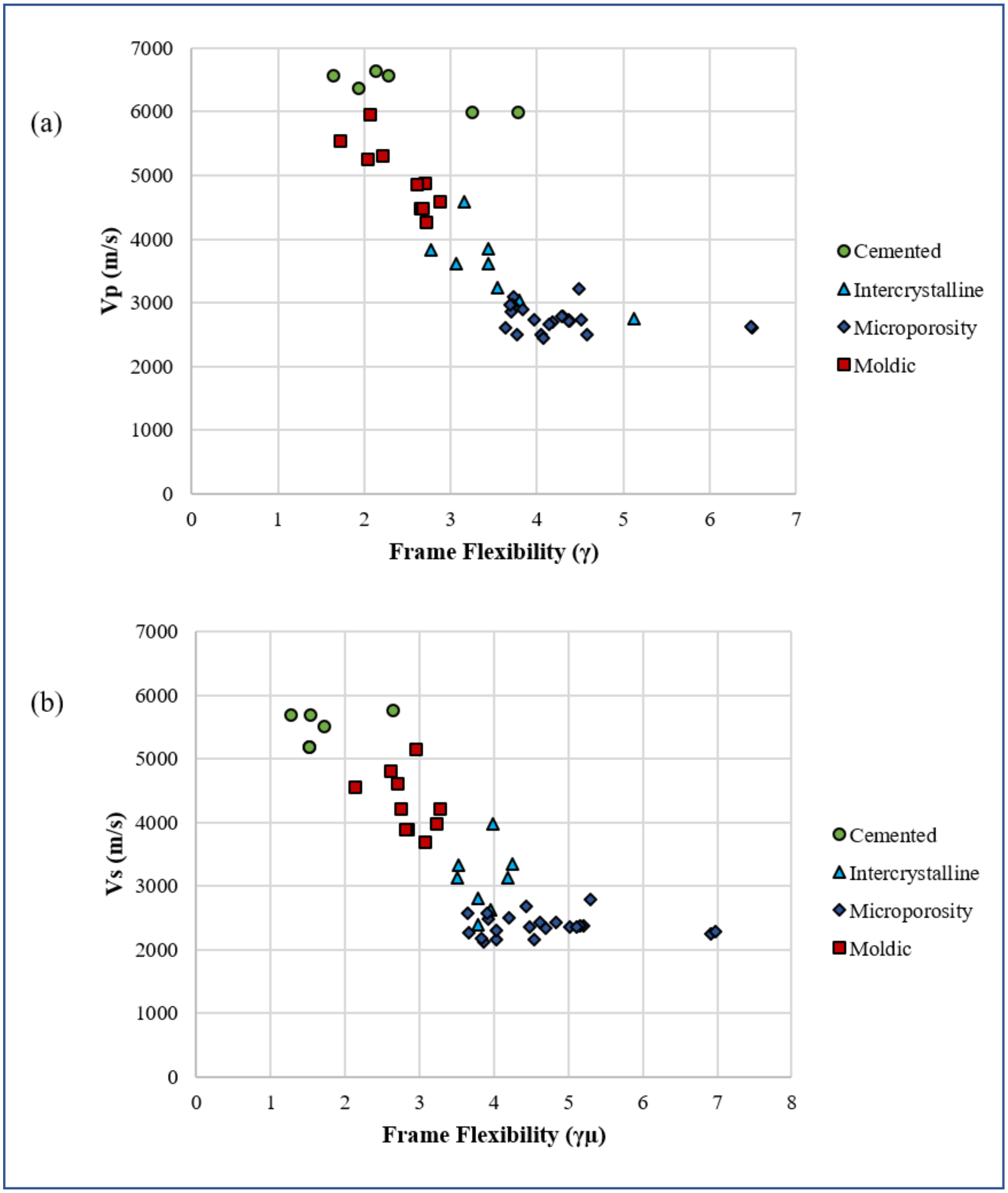

Figure 56. Diagram with frame flexibility factors (γ and γ_{μ}) versus velocities with pore types identified for CO_2 liquid (a) Vp velocity versus frame flexibility factors (γ), (b) Vs versus frame flexibility factors (γ_{μ})

Higher frame flexibility is displayed in microporosity pores with low bulk and low shear modulus values, whereas lower frame flexibility is shown in cemented pores with high bulk and high shear modulus values (Figures 57 and 58). Overall, the relationship is low frame flexibility factor values are associated with low porosities, high velocities, high bulk modulus, and high shear modulus. The opposite is true for low frame flexibility factor values, they are associated with high porosities, low velocities, low bulk modulus, and low shear modulus. Table 7 lists the ranges of properties for a CO_2 liquid saturated carbonate rock using Bahamian data.

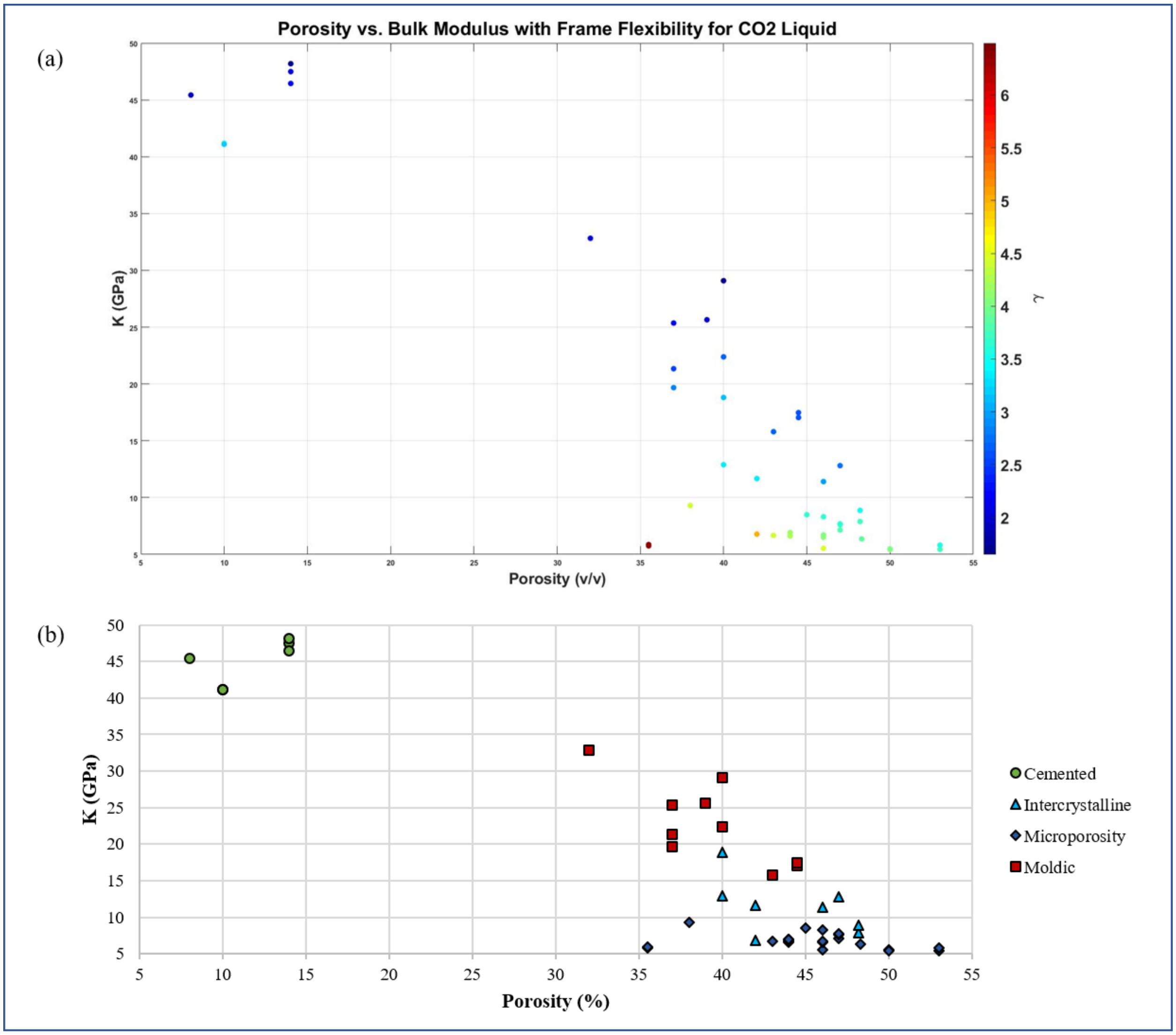

Figure 57. K-porosity crossplots for CO_2 liquid (a) includes a gradient for frame flexibility (γ). (b) diagram with pore types identified.

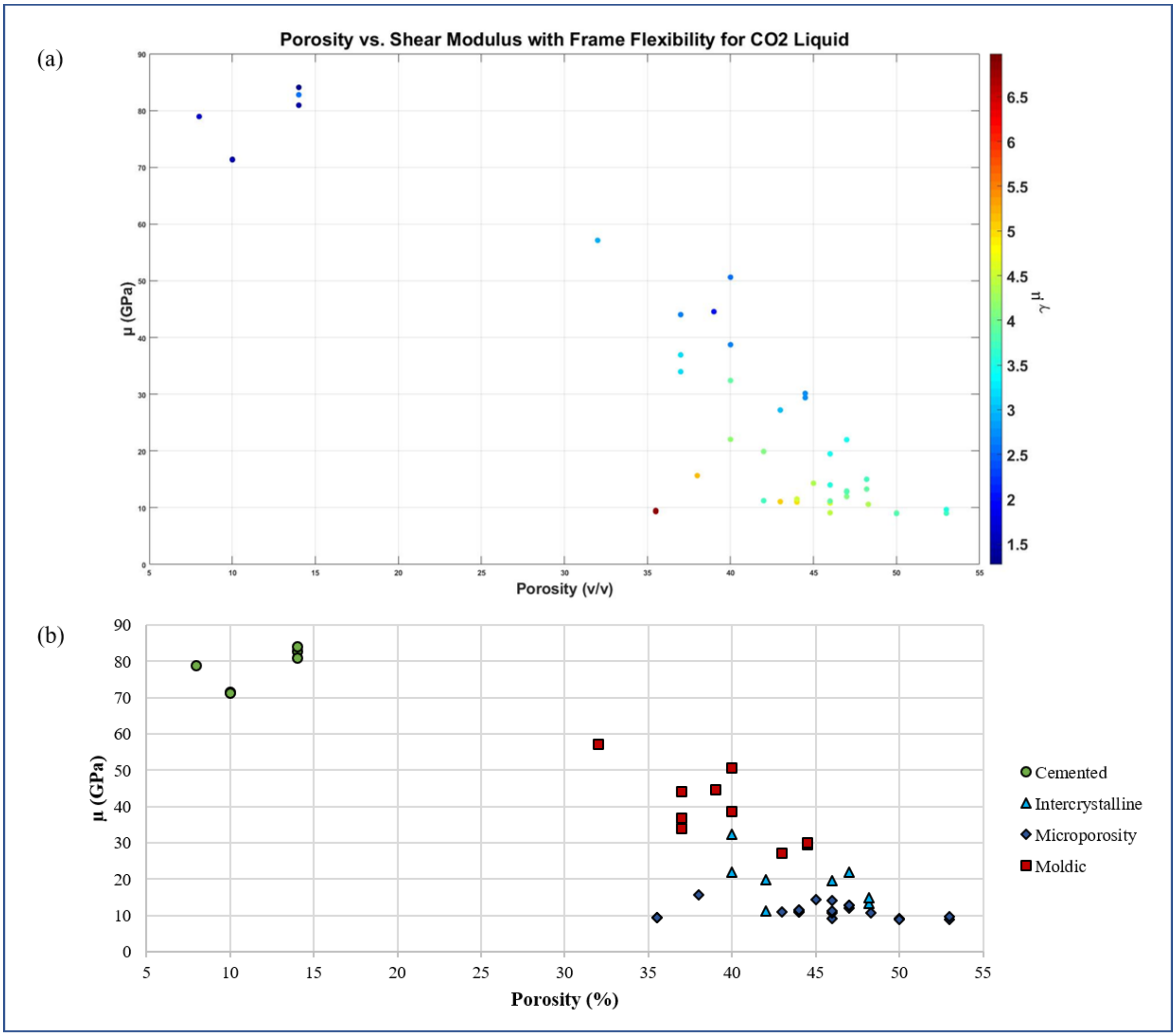

Figure 58. μ-porosity crossplots for CO_2 liquid (a) includes a gradient for frame flexibility ($\gamma\mu$). (b) diagram with pore types identified.

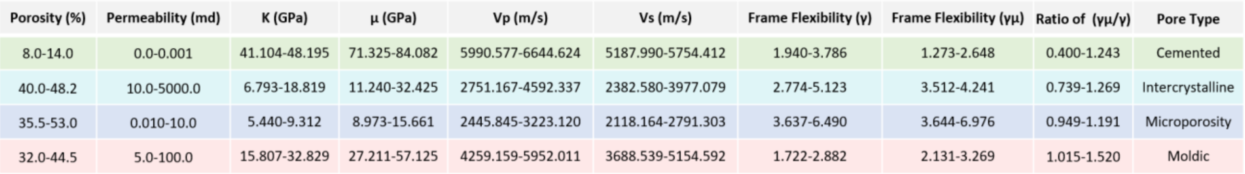

Porosity (%)	Permeability (md)	K (GPa)	μ (GPa)	Vp (m/s)	Vs (m/s)	Frame Flexibility (γ)	Frame Flexibility (γμ)	Ratio of (γμ/γ)	Pore Type
8.0-14.0	0.0-0.001	41.104-48.195	71.325-84.082	5990.577-6644.624	5187.990-5754.412	1.940-3.786	1.273-2.648	0.400-1.243	Cemented
40.0-48.2	10.0-5000.0	6.793-18.819	11.240-32.425	2751.167-4592.337	2382.580-3977.079	2.774-5.123	3.512-4.241	0.739-1.269	Intercrystalline
35.5-53.0	0.010-10.0	5.440-9.312	8.973-15.661	2445.845-3223.120	2118.164-2791.303	3.637-6.490	3.644-6.976	0.949-1.191	Microporosity
32.0-44.5	5.0-100.0	15.807-32.829	27.211-57.125	4259.159-5952.011	3688.539-5154.592	1.722-2.882	2.131-3.269	1.015-1.520	Moldic

Table 7. Ranges of properties for a CO_2 (liquid)-saturated carbonate rock, using Bahamian data.

5.3.5 Pressure Analysis of Fluid Substitutions

Previously mentioned, Figure 24, depicts various traces which each trace represents the velocities at different pressures for one sample. Below, Figure 59, shows a modified graph by Mammadova (2010) of the graph created by Anselmetti and Eberli (1993), with the different pore types labelled. The velocity evolution of carbonate rocks under varying pressures depends on pore types and lithologies (Figure 59), as previously mentioned in this thesis.

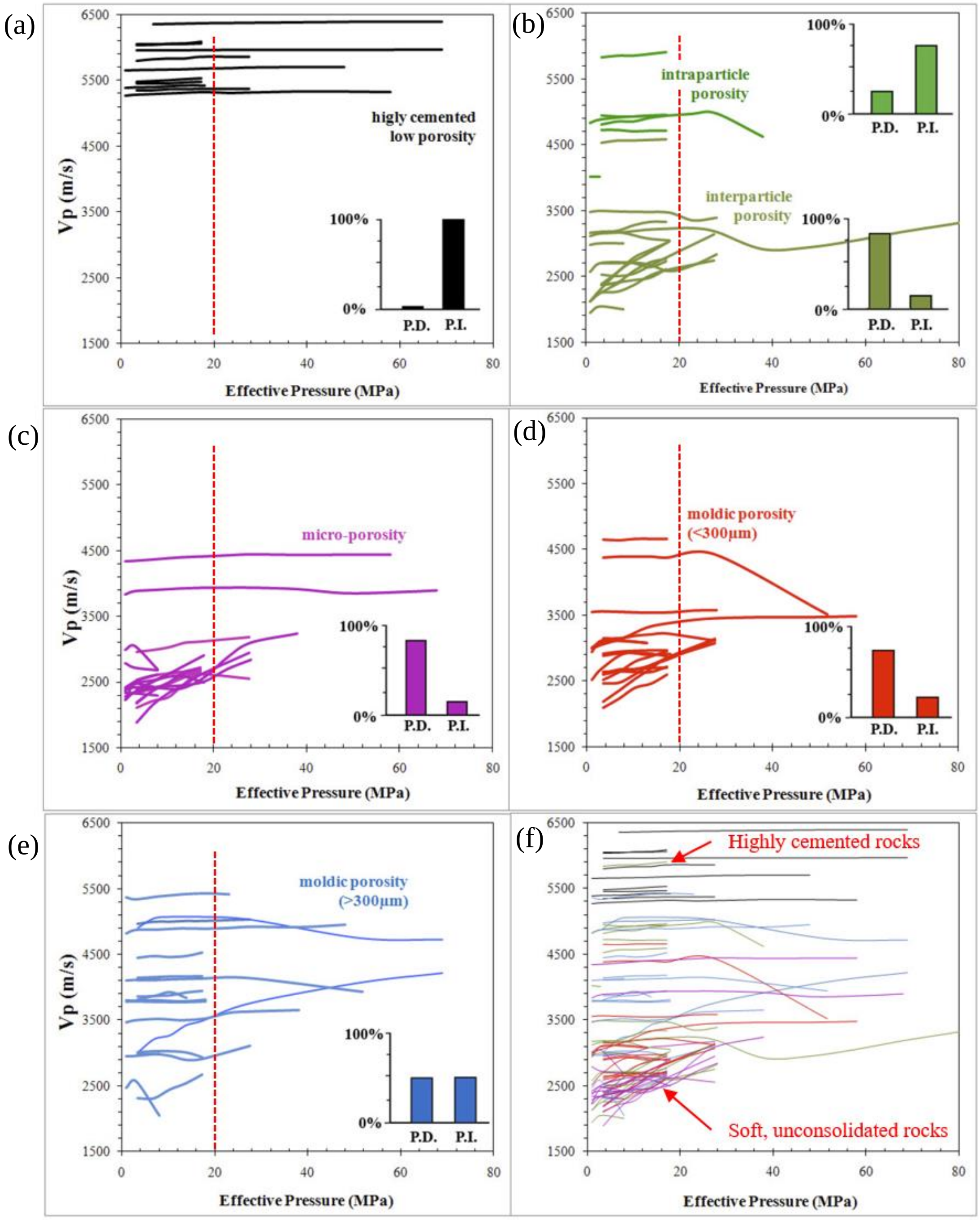

Figure 59. Velocity of all samples at increasing effective pressures, where each trace represents the velocities at different pressures for different pore types. The pore types associated with the traces are: (a) cemented pores, (b) interparticle and intraparticle pores, which for this research refer to intercrystalline pores, (c) microporosity pores, (d) coarse moldic pores, (e) fine moldic pores, (f) all 89 samples at increasing effective pressures. Each pore type was determined to be either P.D. (Pressure-Dependent) or P.I. (Pressure Independent). A large majority of the samples reach critical pressure at 20 MPa, as shown with the red dashed line (modified from Mammadova, 2011).

Using the data for a microporosity sample that depicts the average pressure change trend for this pore type, Figure 60 displays P-wave (Vp) velocities, bulk moduli (K), and shear moduli (μ) at varying effective pressures for each fluid substitution. The highest Vp and K values are associated with water-saturated samples, followed by oil-saturated, CO_2-liquid-saturated samples, CO_2-gas-saturated samples, and lastly dry samples. The same pattern occurs for the moldic sample in Figure 61. Both Figure 60 and Figure 61, show the shear modulus to remain unchanged for all fluids under varying effective pressures. The lack of change in the shear modulus is associated to the assumption in Gassmann's equation that $\mu_{dry} = \mu_{saturated}$. The pressure changes displayed in Figure 60 and Figure 61 are under a constant porosity and are based on saturation changes created by the density effect as each fluid has a different density.

(a)

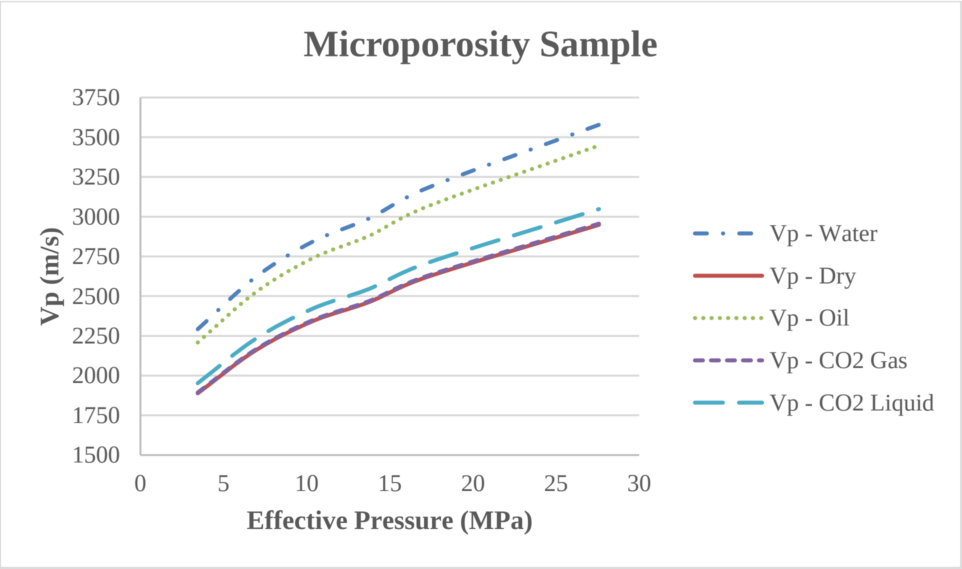

Figure 60. (a) P-wave (Vp) velocities for microporosity sample at different effective pressures, with different fluid substitutions; (b) Bulk moduli (K) for microporosity sample at different effective pressures, with different fluid substitutions; (c) Shear moduli (μ) for microporosity sample at different effective pressures, with different fluid substitutions. Microporosity sample at a porosity of 53%.

(b)

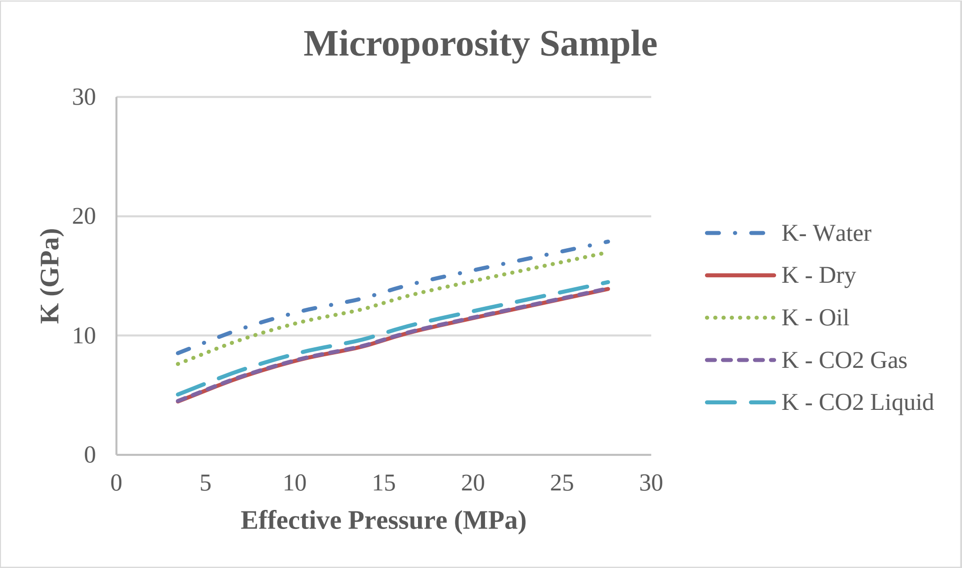

(c)

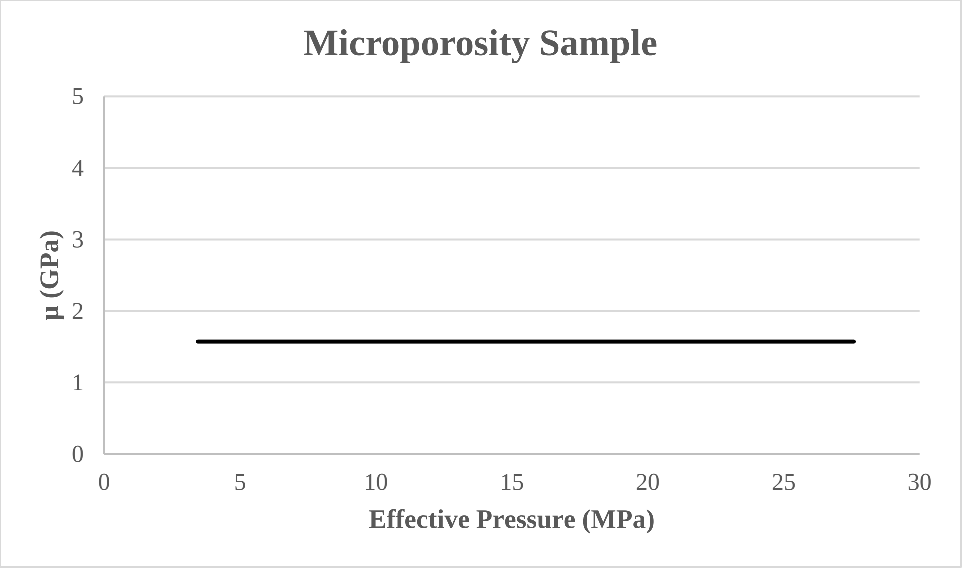

Figure 60. Continued.

(a)

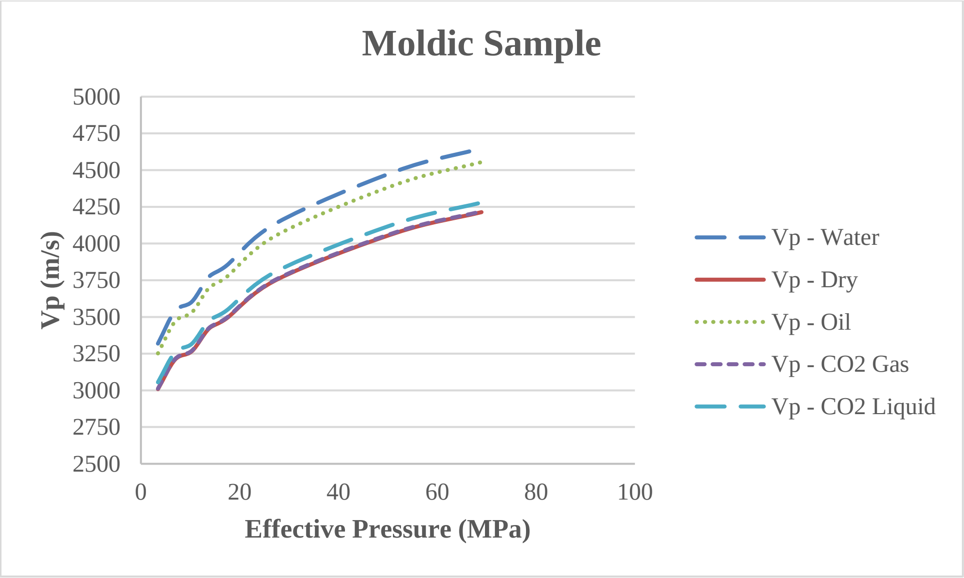

(b)

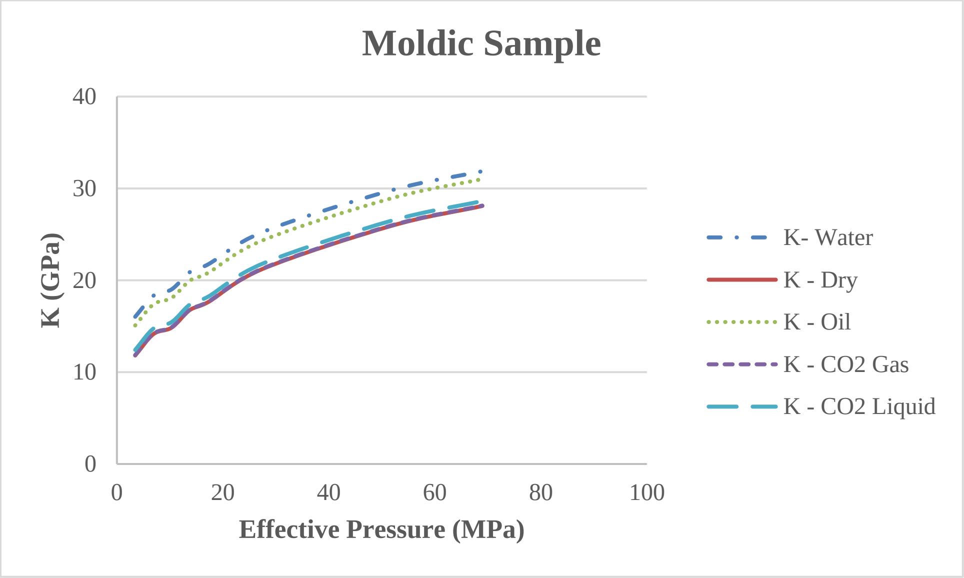

Figure 61. (a) P-wave (Vp) velocities for moldic sample at different effective pressures, with different fluid substitutions; (b) Bulk moduli (K) for moldic sample at different effective pressures, with different fluid substitutions; (c) Shear moduli (μ) for moldic sample at different effective pressures, with different fluid substitutions. Moldic sample at a porosity of 50%.

(c)

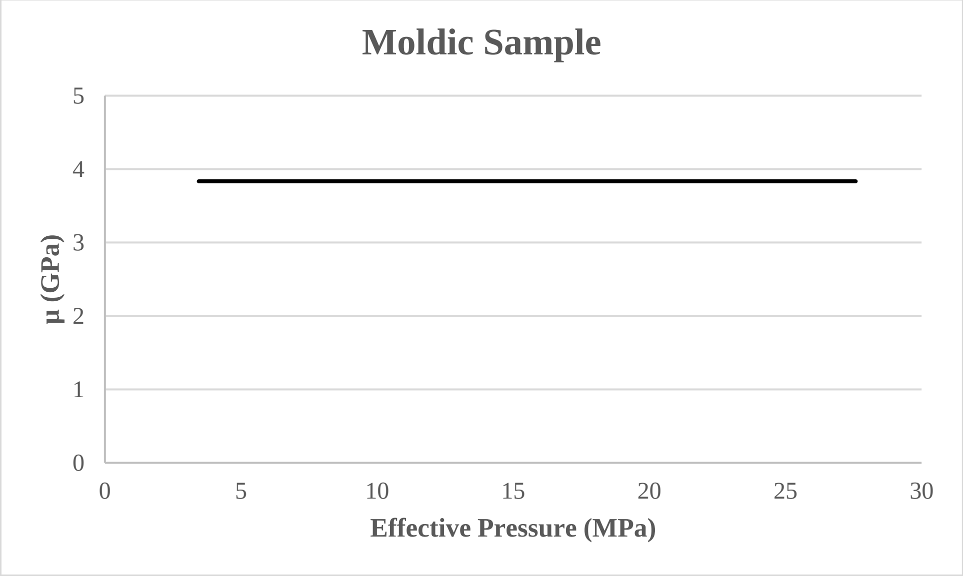

Figure 61. Continued.

5.3.6 Fluid Substitution Overall Results

The general relationship is low frame flexibility factor values are associated with low porosities, high velocities, high bulk modulus, and high shear modulus. The opposite is true for high frame flexibility factor values, they are associated with high porosities, low velocities, low bulk modulus, and low shear modulus. This relationship is not observed by CO_2 gas saturated rocks, which display the opposite trend for $\gamma\mu$ values.

The bulk modulus increases from water-saturated to live-oil (except cemented pores decrease), then decreases with CO_2 gas and remains roughly the same for CO_2 liquid. Using this same table, from live-oil to CO_2 gas, Vp decreases and bulk modulus decreases. Live-oil to CO_2 liquid, Vp increases and bulk modulus decreases.

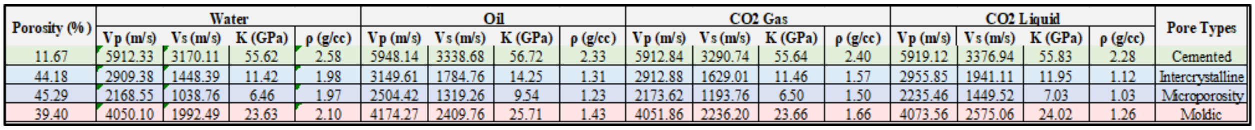

Porosity (%)	Water				Oil				CO2 Gas				CO2 Liquid				Pore Types
	Vp (m/s)	Vs (m/s)	K (GPa)	ρ (g/cc)	Vp (m/s)	Vs (m/s)	K (GPa)	ρ (g/cc)	Vp (m/s)	Vs (m/s)	K (GPa)	ρ (g/cc)	Vp (m/s)	Vs (m/s)	K (GPa)	ρ (g/cc)	
11.67	5912.33	3170.11	55.62	2.58	5948.14	3338.68	56.72	2.33	5912.84	3290.74	55.64	2.40	5919.12	3376.94	55.83	2.28	Cemented
44.18	2909.38	1448.39	11.42	1.98	3149.61	1784.76	14.25	1.31	2912.88	1629.01	11.46	1.57	2955.85	1941.11	11.95	1.12	Intercrystalline
45.29	2168.55	1038.76	6.46	1.97	2504.42	1319.26	9.54	1.23	2173.62	1193.76	6.50	1.50	2235.46	1449.52	7.03	1.03	Microporosity
39.40	4050.10	1992.49	23.63	2.10	4174.27	2409.76	25.71	1.43	4051.86	2236.20	23.66	1.66	4073.56	2575.06	24.02	1.26	Moldic

Table 8. Comparison of average Vp, Vs, K and ρ for different fluid substitution models with pore types identified and average porosity.

The simulated substitution of water-wet samples with oil, and later with CO_2 in gas and liquid phase results both in different bulk moduli and velocities. CO_2 flooding decreases the bulk modulus for the samples, with the decrease being slightly more for CO_2 in the gas phase. The Vs increases with CO_2 substitutions, as the density of each individual fluid phase decreases whereas shear modulus is kept constant. The increase in Vs is much higher for the gas phase CO_2 than the liquid phase CO_2, due to the change in rock densities is higher for CO_2 gas rocks than CO_2 liquid rocks. Higher porosities also result in a higher decrease in density, and therefore a higher Vs.

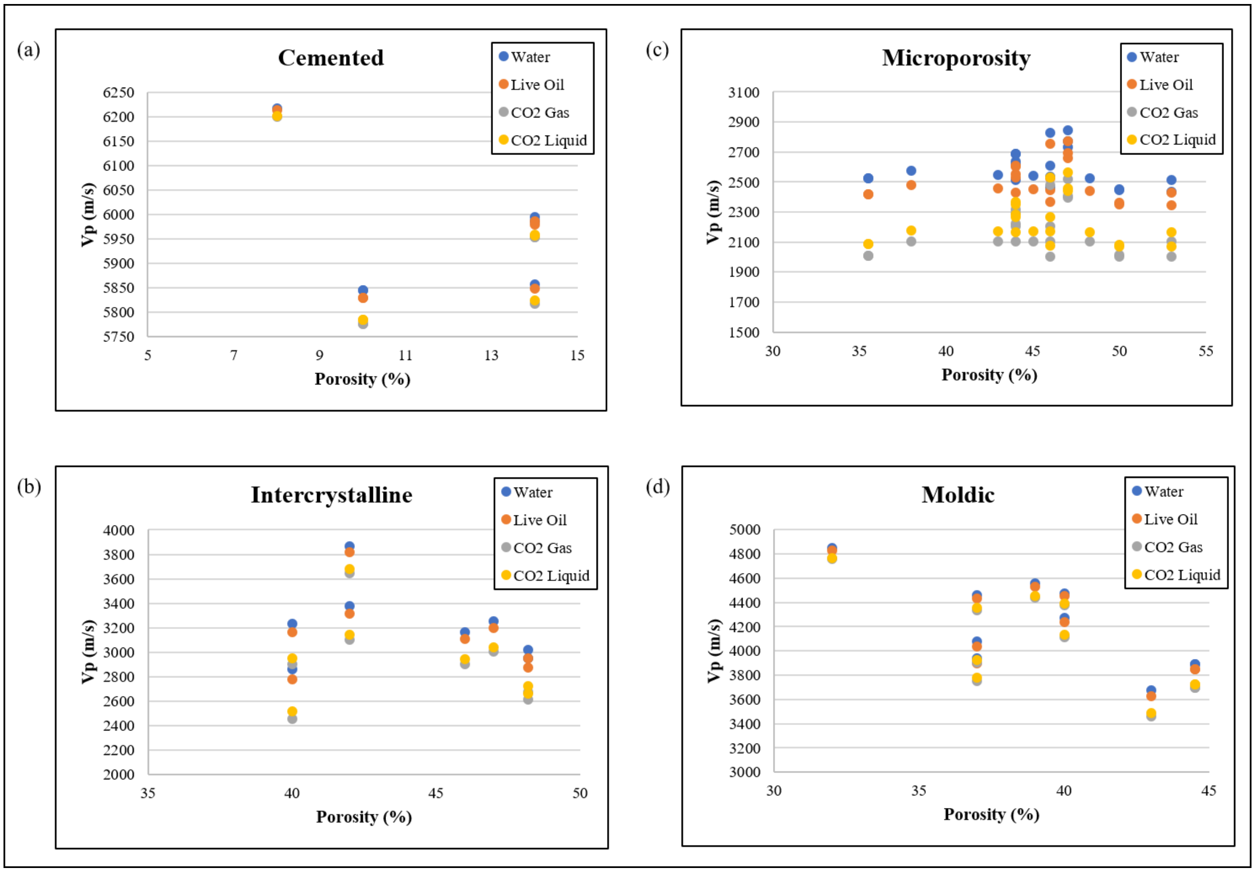

Figure 62. Velocity-porosity crossplot for each pore type, with the Vp for each type of fluid substitution labelled (i.e. water, live-oil, CO_2 gas, CO_2 liquid); (a) cemented pores, (b) intercrystalline pores, (c) microporosity pores, (d) moldic pores.

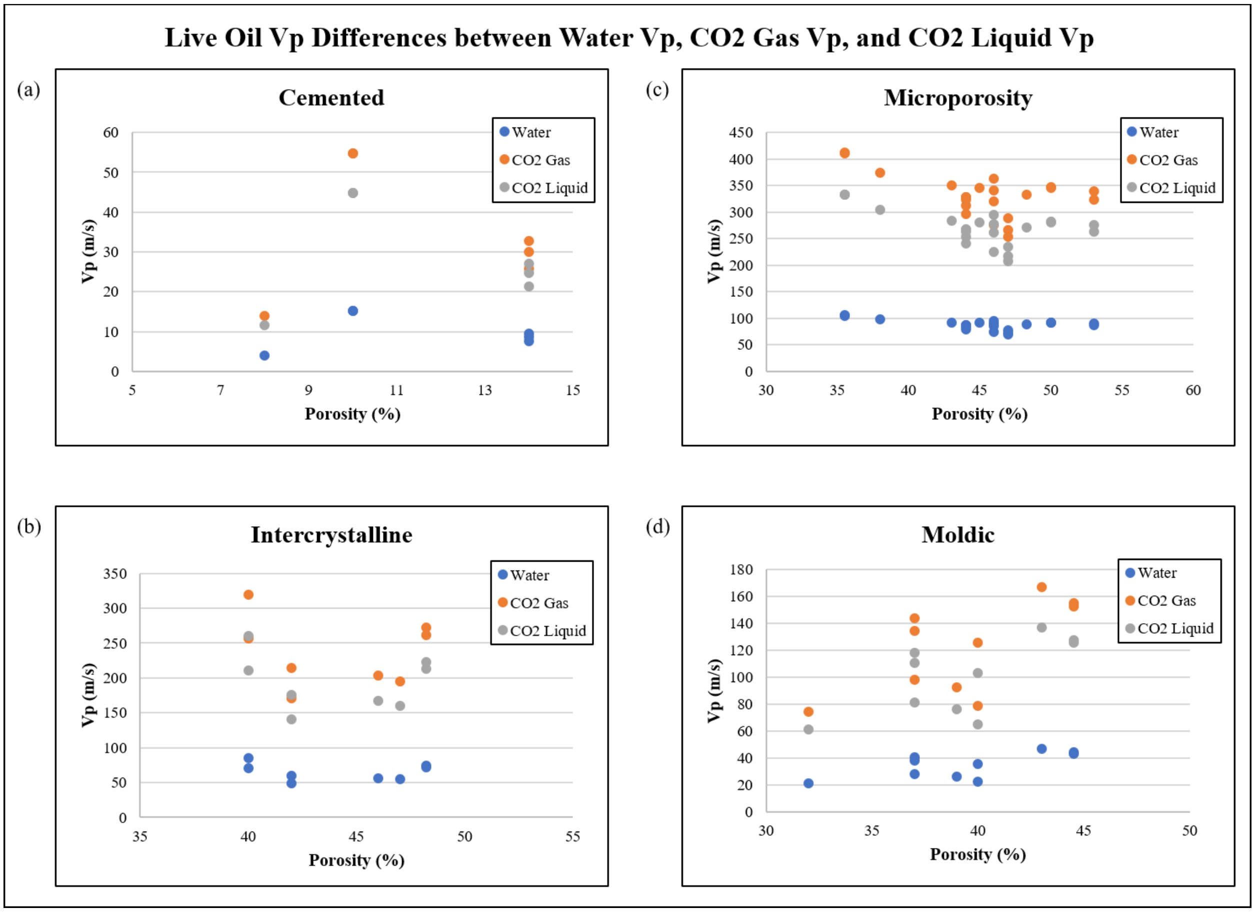

Figure 63. Velocity-porosity crossplot for each pore type, with the Vp difference between live-oil and each type of fluid substitution labelled (i.e. water, CO_2 gas, CO_2 liquid); (a) cemented pores, (b) intercrystalline pores, (c) microporosity pores, (d) moldic pores.

The effects of CO_2 saturation on the velocities are calculated by:

$$Effect\ of\ flooding = \frac{CO_2\ flooded\ velocity - Oil\ saturated\ velocity}{Oil\ saturated\ velocity} \times 100\% \qquad \textbf{(5-13)}$$

As seen in Figure 59, the Vp values for water-saturated rocks are the highest with CO_2 gas-saturated rocks having the lowest Vp values for all pore types. Figure 60 shows the difference between live-oil Vp and the Vp for the other fluids, which shows the highest difference between live oil and CO_2 gas. The lowest difference is shown to be between live oil and water, as they have similar properties.

Using Equation 5.9, the effect of CO_2 flooding calculations in Table 8 are completed, which depict the highest percent change for Vp, Vs, bulk modulus (K), and density (ρ) for microporosity pores and the lowest for cemented pores. The CO_2 flooding effect (for both gas and liquid phases) for each pore type, from highest to lowest percent change, is microporosity pores, intercrystalline pores, moldic pores, and cemented pores. The percent change is higher for CO_2 gas than for CO_2 liquid.

Porosity (%)	**CO_2 Gas Flooding Effect (Oil-CO_2 Gas)**				**CO_2 Liquid Flooding Effect (Oil-CO_2 liquid)**				**Pore Types**
	ΔVp (%)	**ΔVs (%)**	**ΔK (%)**	**Δρ (%)**	**ΔVp (%)**	**ΔVs (%)**	**ΔK (%)**	**Δρ (%)**	
11.67	-0.59	-1.44	-1.90	2.92	-0.49	1.15	-1.56	-2.24	Cemented
44.18	-7.52	-8.73	-19.61	19.61	-6.15	8.76	-16.18	-15.03	Intercrystalline
45.29	-13.21	-9.51	-31.83	21.40	-10.74	9.87	-26.23	-16.39	Microporosity
39.40	-2.93	-7.20	-7.97	16.03	-2.41	6.86	-6.58	-12.28	Moldic

Table 9. CO_2 flooding effect percent changes for average Vp, Vs, K, and ρ, with different pore types identified.

5.4 Conclusions

Low frame flexibility factor values correlate to low porosities, high velocities, high bulk modulus, and high shear modulus. The opposite is true for high frame flexibility factor values, although the relationship does not occur for CO_2 gas saturated rocks that display the opposite trend for $\gamma\mu$ values.

For physical properties at varying effective pressures and a constant porosity, the highest Vp and K values are associated with water-saturated samples, followed by oil-saturated, CO_2-liquid-saturated samples, CO_2-gas-saturated samples, and lastly dry samples. The shear modulus remains unchanged for all fluids under varying effective pressures, due to the assumption in

Gassmann's equation that $\mu_{dry} = \mu_{saturated}$. The pressure changes, under a constant porosity, are based on saturation changes created by the density effect as each fluid has a different density.

In general, CO_2 decreases Vp and bulk modulus (a larger decrease occurs for CO_2 gas rather than CO_2 liquid). The Vp for water-saturated rocks are the highest, whereas CO_2 gas-saturated rocks have the lowest Vp values for all pore types. Looking at pore types, moldic pores show an increase in Vp, whereas intercrystalline and microporosity samples decrease. The Vp values are controlled by the bulk modulus effect rather than the density effect. The difference between oil Vp and the Vp of other fluids is highest for CO_2 gas and lowest for water. Water and oil have similar properties, which is why the Vp difference between the two fluids is lowest.

The percent change in relation to pore types, was highest for microporosity and lowest for cemented pores. The CO_2 flooding effect percent change was higher for CO_2 gas than CO_2 liquid.

6. SEISMIC MONITORING OF CO_2 FLOODING IN CARBONATE ROCKS

6.1 Basic Overview of Seismic and Elastic Moduli

In a seismic survey, acoustic wave sources and receivers are used to interpret the geometry and properties of the subsurface. The different materials that compose rock layers give off different acoustic impedance (Z) values. The amount of energy reflected back to the receiver depends on the angle at which the wave intercepts the difference in impedance of the rock layers, which is known as the reflection coefficient (RC).

$$RC = \frac{\rho_2 v_2 - \rho_1 v_1}{\rho_2 v_2 + \rho_1 v_1} \; or \; \frac{z_2 - z_1}{z_2 + z_1} \qquad \textbf{(6-1)}$$

where RC is the reflection coefficient, ρ is the density (g/cm^3), v is the velocity (m/s), and z is the acoustic impedance.

Multiple waves are produced during seismic surveys, which include the primary wave or pressure wave, known as the P-wave, and the secondary wave or shear wave, known as the S-wave. These waves have their own velocities, which is dependent on the bulk (K) and shear (μ) moduli properties. The bulk modulus is the rock’s ability to resist changes in volume, whereas the shear modulus is the rock’s ability to resist changes in shape – both are in the units gigapascal (GPa). The equations for the P-wave and S-wave velocities are below:

$$V_p = \sqrt{\frac{K + \frac{4}{3}\mu}{\rho}} \qquad \textbf{(3-2)}$$

and,

$$V_s = \sqrt{\frac{\mu}{\rho}} \tag{3-3}$$

where ρ is the density (g/cm^3), K is the bulk modulus, μ is the shear modulus, and V is the velocity (m/s). Since fluid theoretically has negligible resistance to shear change, the shear modulus for all fluids will be considered 0 GPa and therefore the velocity of the S-wave through a fluid will also be considered 0 m/s. This is keeping in mind:

$$\mu_{sat} = \mu_{dry} \tag{3-4}$$

where μ_{sat} is the saturated shear modulus and μ_{dry} is the dry shear modulus.

Gassmann’s equation for fluid substitution is used for time-lapse seismic monitoring, as it provides calculations for various fluid scenarios before actual flooding of fluids. For this thesis, we validate Gassmann’s theory in carbonate rocks and its assumptions. With this, we theoretically saturate the initially water-saturated carbonate sample with live-oil, then using the same samples, the flooding with CO_2 both in liquid and gas phase is simulated. Water-flooded samples are also simulated in this research. The high porosities in the Bahamian Clino and Unda core samples increase the volume of fluid, allowing larger seismic responses and dry-frame compressibility result in a better understanding and sense of the pore fluid. The results from this study should not be applied to all carbonate rocks, as the samples used are from a modern carbonate province with very high porosities.

6.2 Methodology

Using CGG’s Hampson-Russell Geoview software, forward modeling was completed using the dataset’s horizons, P-wave velocity, and density were entered to create synthetic density and sonic p-wave logs. Using these log properties, the acoustic impedance was developed and combined with a seismic wavelet to output synthetic seismic models. The models created in Hampson-Russell include: synthetic seismic, p-wave velocity model, density model, and the acoustic impedance model. These models will be used to analyze the formation properties and create correlations between pore types and CO_2 flooding effects.

6.3 Seismic Analysis Results

The synthetic seismic of each fluid substitution mimics Figure 64, which displays the associated lithologies for the cores and seismic sequences.

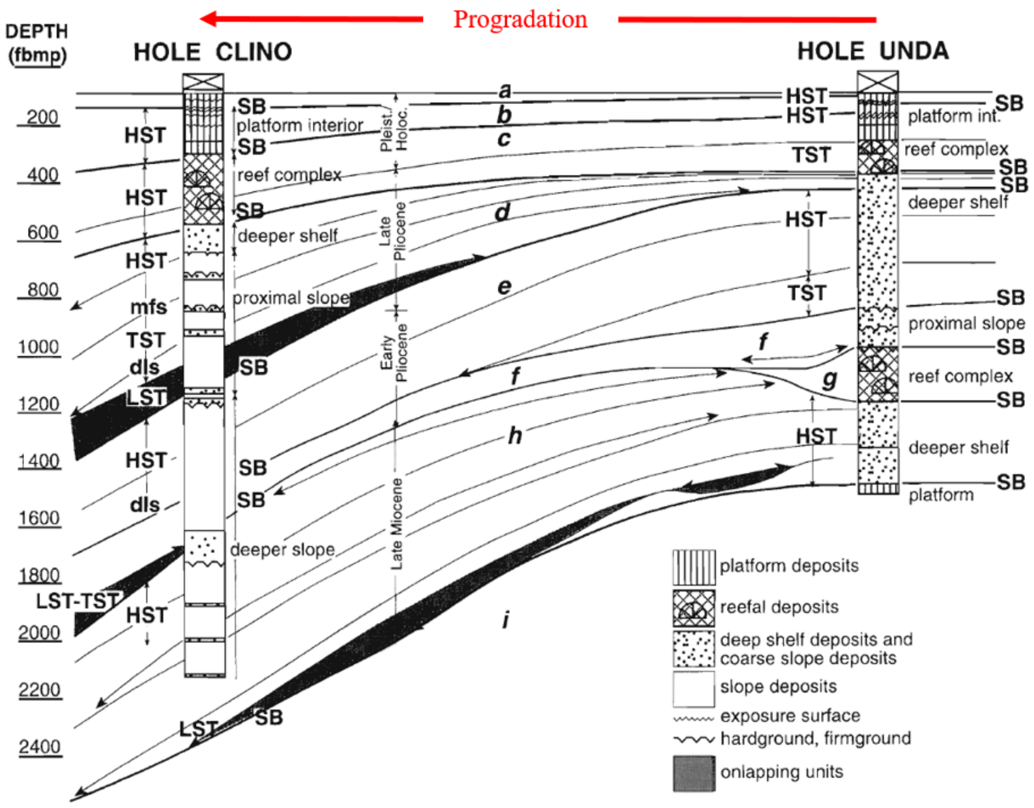

Figure 64. Stratigraphic framework with lithologies and seismic sequences (modified from Eberli et al., 2012).

As previously mentioned, cemented pores and moldic pore types have high density, high velocity, and low porosity. Lower densities and velocities are correlated with microporosity and intercrystalline pores, for both Clino and Unda cores. Higher values on the density logs and P-wave velocity (Vp) logs correlate with the pore type horizon tops of cemented and moldic pores.

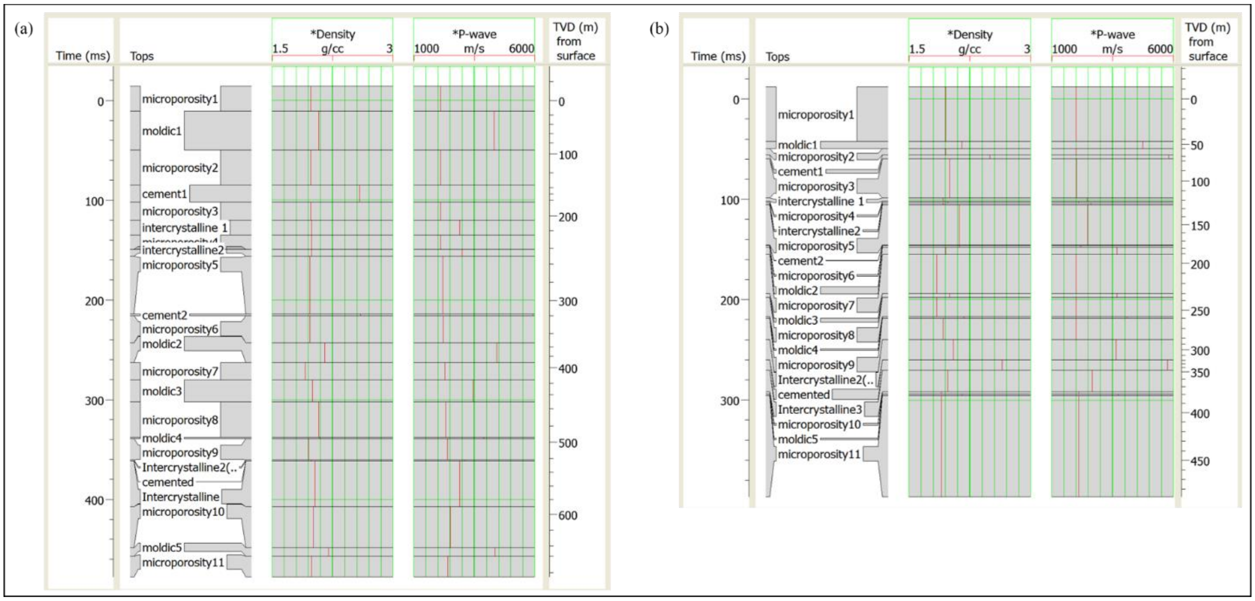

Figure 65. Water-saturated rock density and P-wave velocity logs for (a) Clino core and (b) Unda core, with associated pore type horizon tops

Amplitude is related to reflectivity, which is related to subsurface impedance contrasts, as the reflection coefficient is calculated with the impedance of different horizons. Amplitude attributes provide information about the rock. In this study, the amplitudes are positive values for cemented and moldic pore types. This is due to cementation affecting the mechanical strength of the rocks, which affects the seismic reflections. Cemented and moldic pores, have high impedance values, high velocities, low porosity, high density, high elastic moduli, and therefore, create high amplitudes. The opposite is true for intercrystalline and microporosity pore types.

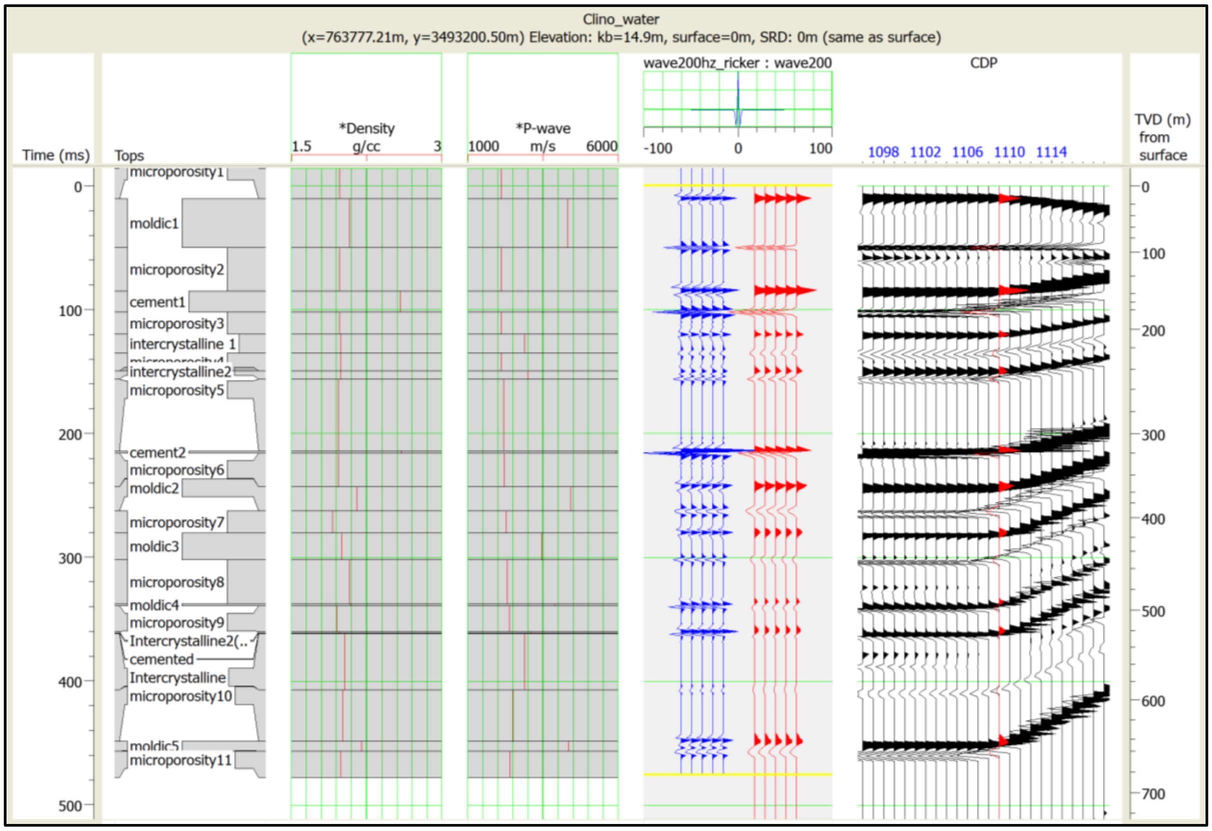

Figure 66. Correlation between water-saturated Clino core density and P-wave velocity (Vp) logs and synthetic seismic amplitudes with pore type horizon tops

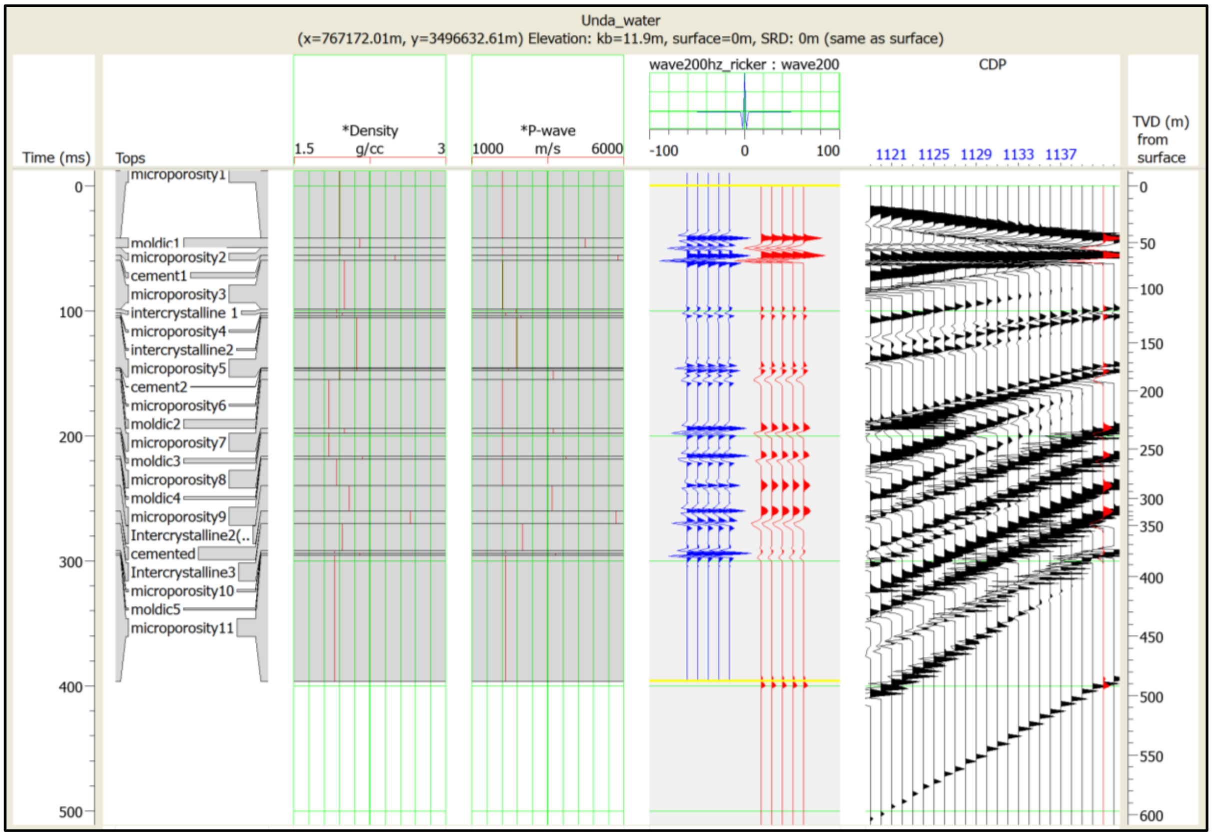

Figure 67. Correlation between water-saturated Unda core density and P-wave velocity (Vp) logs and synthetic seismic amplitudes with pore type horizon tops.

The samples used for modeling fluid substitutions in seismic monitoring are samples with the same porosity and similar mineralogy, but have different velocities due to pore types. The samples chosen are characteristic of the different pore types. Cemented pores were not included in the sample selection, as they have little to no porosity, and would not be a targeted zone for substitution.

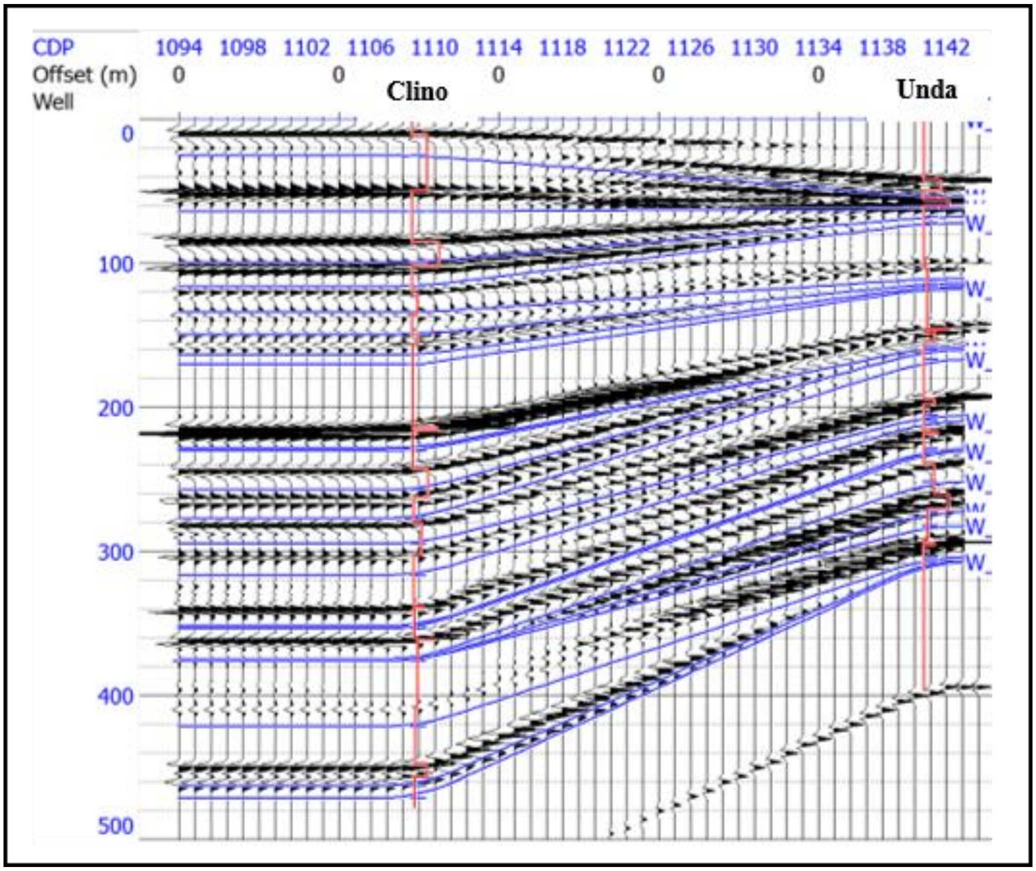

Figure 68. Synthetic seismic section for Clino and Unda cores before fluid substitutions.

In Figure 69, the P-wave velocities for each pore type are shown over the synthetic seismic amplitudes. The high velocities relate to the cemented and moldic pore types, whereas the low velocities relate to intercrystalline and microporosity pores. When comparing the fluid substitution models, the model with the higher Vp values is the waterflooded substitution, followed by oil, CO_2 liquid, and CO_2 gas, respectively. This is shown in Figure 69 (a-d) through the use of a red arrow at ~240 meters common depth point (CDP), a yellow arrow at ~300 meters CDP, and a blue arrow at ~500 meters CDP. The red arrow is the top of moldic rock, whereas the yellow and blue arrows are the tops of microporosity rock. All three horizons have the highest value in the waterflood substitution. This relationship was previously shown in Figure 60 and Figure 61.

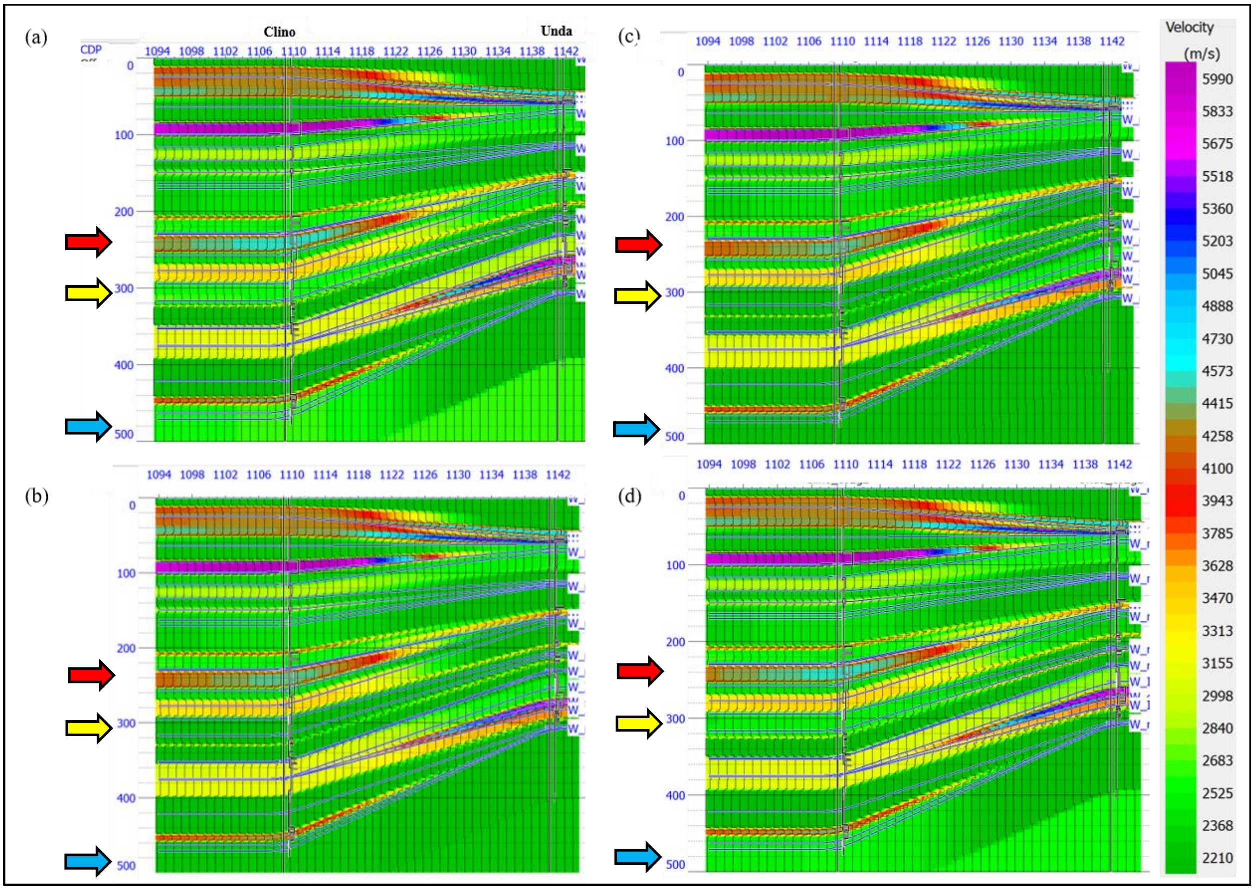

Figure 69. Synthetic seismic section with Vp for (a) waterflooded, (b) oil-saturated, (c) CO_2 gas-saturated, and (d) CO_2 liquid-saturated Clino and Unda cores.

Figure 70 displays the differences in Vp for the different fluid substitutions taken from the measured values, each using a different scale (due to the drastic variations in scale among the models). The waterflood differences in Vp (Figure 70a) are the highest differences, ranging from 130 to 450 m/s changes. The CO_2 gas-saturated substitution differences in Vp (Figure 70c) are the lowest differences, ranging from 4.3 to 5.6 m/s changes. Oil substitution difference range from 100 to 360 m/s, and CO_2 liquid substitution difference range from 20 to 70 m/s. Highest to lowest substitution differences occur in the order: waterflood, oil, CO_2 liquid, and CO_2 gas, respectively.

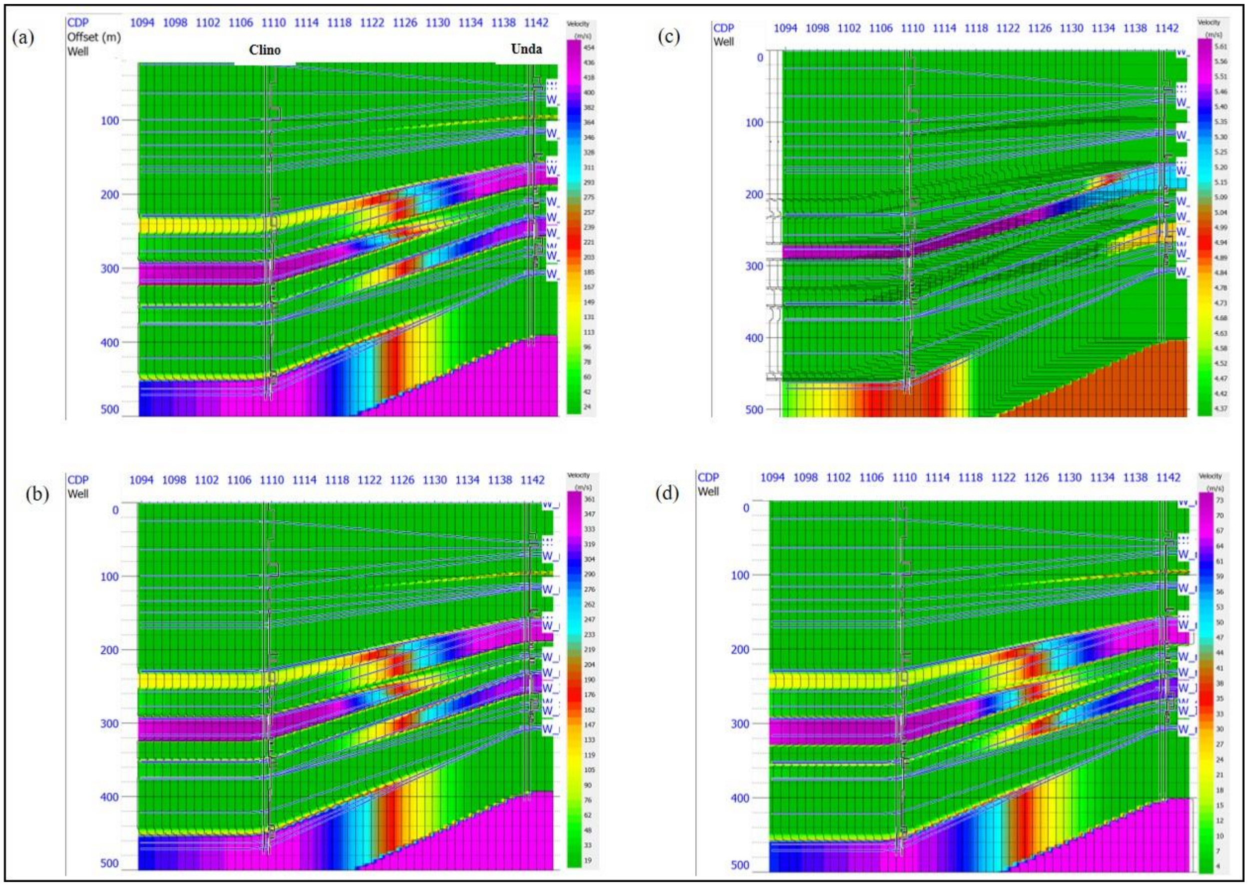

Figure 70. Differences in P-wave velocity (Vp) over synthetic seismic for (a) waterflooded, (b) oil-saturated, (c) CO_2 gas-saturated, and (d) CO_2 liquid-saturated Clino and Unda cores. Each model has a different scale bar.

Figure 71 shows the synthetic seismic with density for the different fluids, with the highest density values in the CO_2 gas-saturated rock, oil, water-flooded, and CO_2 liquid. The densities of the rock are affected by the fluid densities (Equation 4.17). The CO_2 gas showed the highest density values, as the fluid density for CO_2 gas is the smallest at 0.00187 g/cc. Following that, oil has a fluid density of 0.58516 g/cc and water has a fluid density of 1.0 g/cc. The lowest density values were attributed to CO_2 liquid, which has a fluid density of 1.032 g/cc. As mentioned previously, high density values correlate to cemented and moldic pore types, whereas low density values correlate to microporosity and intercrystalline pore types.

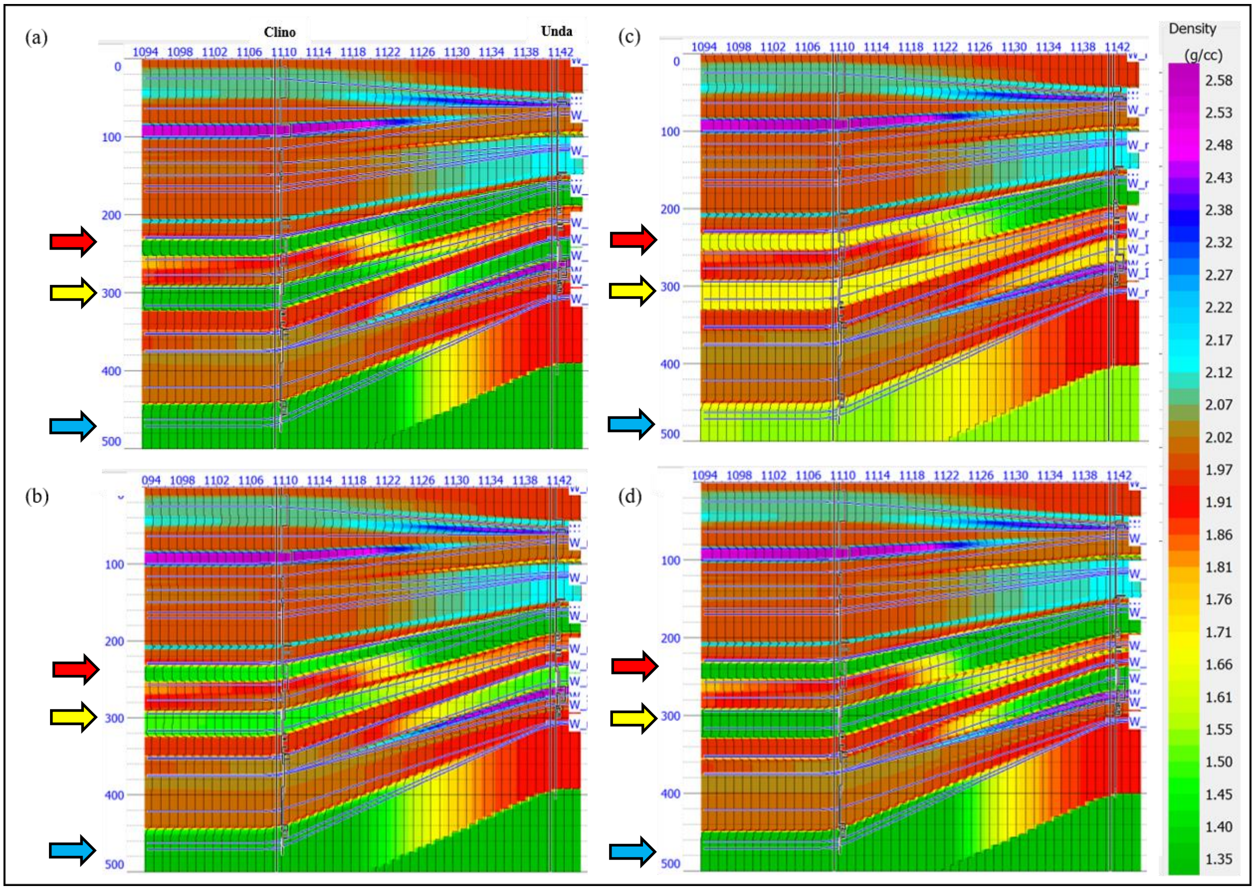

Figure 71. Synthetic seismic section with density for (a) waterflooded, (b) oil-saturated, (c) CO_2 gas-saturated, and (d) CO_2 liquid-saturated Clino and Unda cores.

Figure 72 displays the differences in density for the different fluid substitutions taken from the measured values, each using a different scale (due to the drastic variations in scale among the models). The CO_2 liquid-saturated differences in density (Figure 72d) are the highest differences, ranging from -1.05 to -0.7 g/cc changes. The CO_2 gas-saturated substitution differences in density (Figure 72c) are the lowest differences, ranging from -0.5 to -0.45 g/cc changes. Oil substitution differences range from -0.8 to -0.5 g/cc, and waterflooded substitution differences range from -1.02 to -0.7 g/cc. Highest to lowest substitution differences occur in the order: CO_2 liquid, waterflooded, oil, and CO_2 gas, respectively.

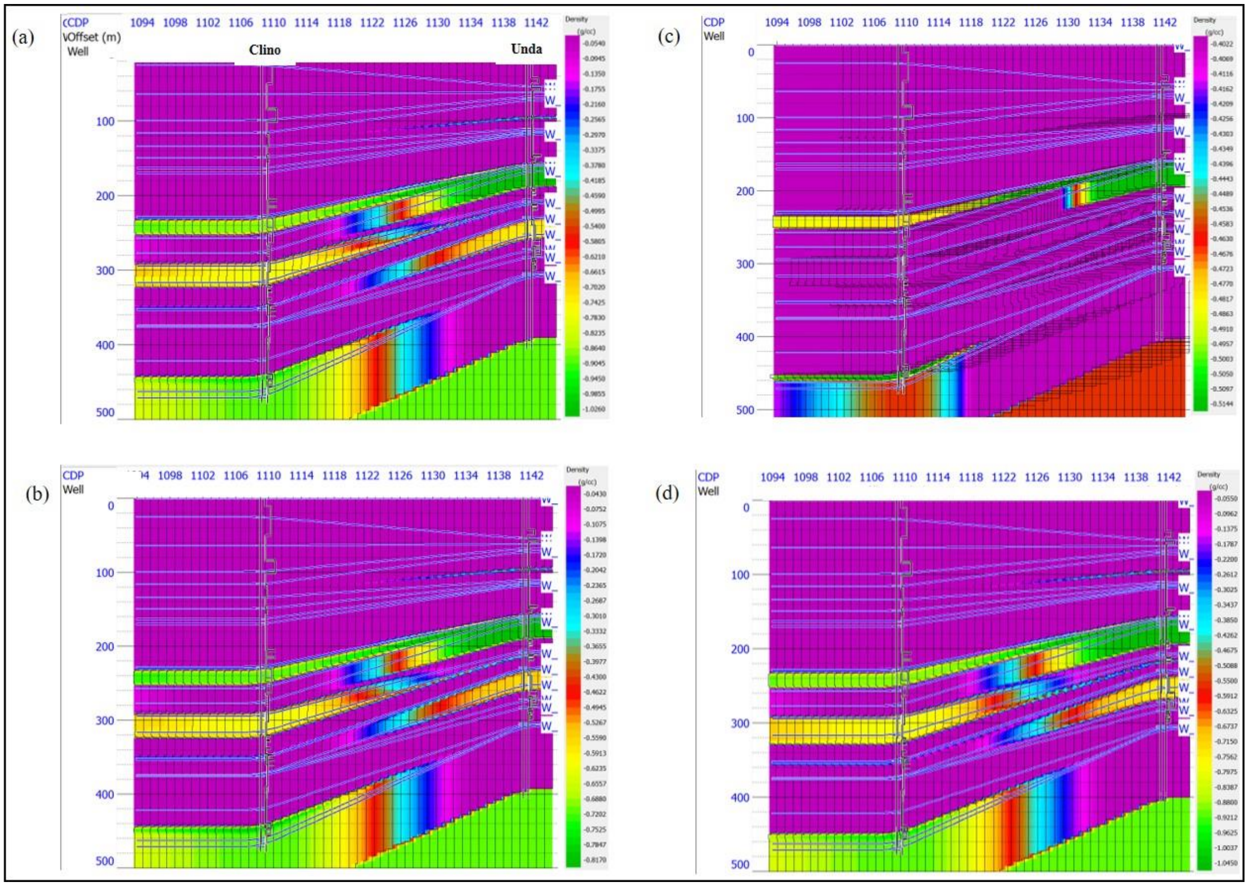

Figure 72. Differences in density over synthetic seismic for (a) waterflooded, (b) oil-saturated, (c) CO_2 gas-saturated, and (d) CO_2 liquid-saturated Clino and Unda cores. Each model has a different scale bar.

The acoustic impedance (Z) values were calculated using Equation 6.1 from the log properties. Large impedance values are related to high amplitudes. These high impedance values occur for cemented and moldic pores, as cementation affects the mechanical strength of the rock and seismic reflections through the reflection coefficient. Figure 73 shows the synthetic seismic with P-impedance for the different fluids, with the highest impedance values in the CO_2 gas-saturated rock, followed by oil, waterflooded, and CO_2 liquid. This is similar to the relationship present in the density models.

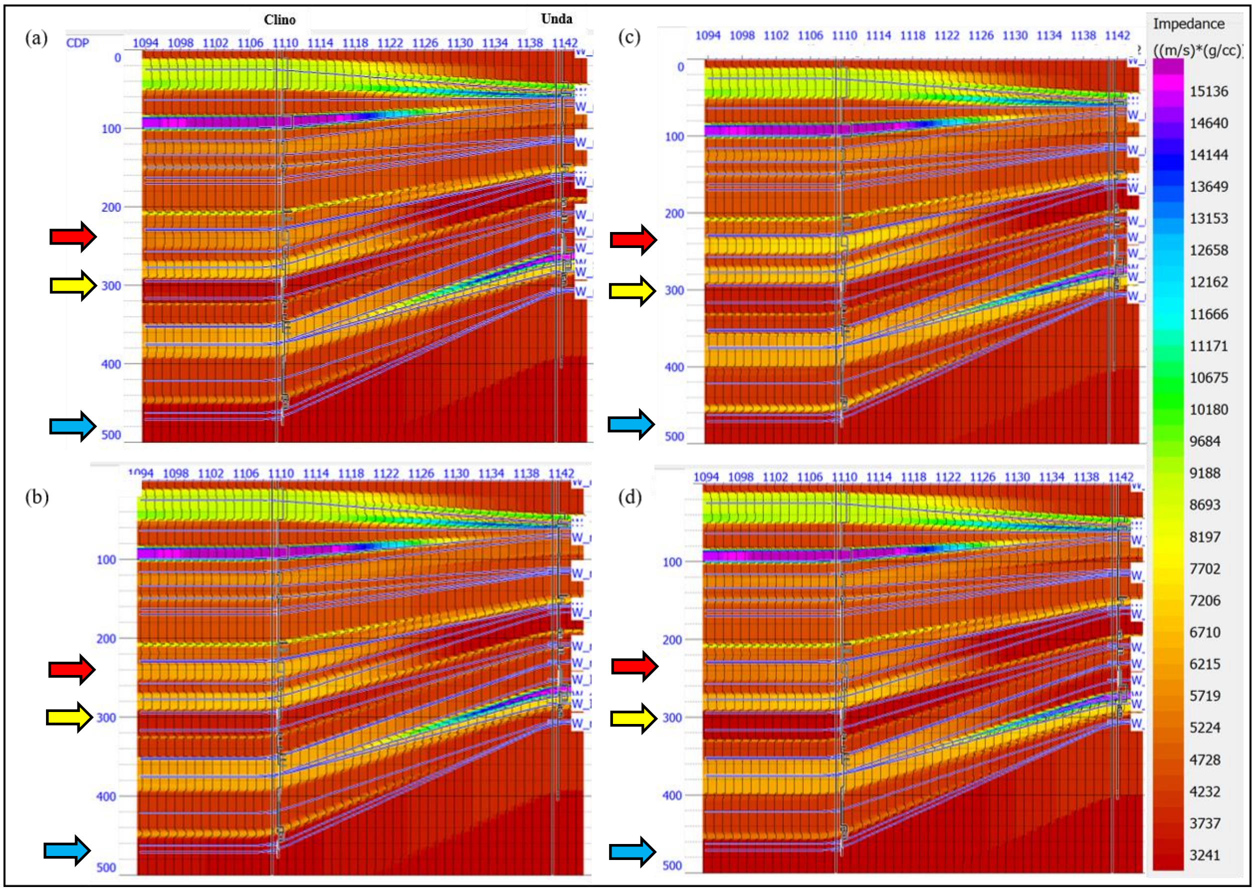

Figure 73. Synthetic seismic section with impedance for (a) waterflooded, (b) oil-saturated, (c) CO_2 gas-saturated, and (d) CO_2 liquid-saturated Clino and Unda cores

Figure 74 displays the differences in impedance (Z) for the different fluid substitutions taken from the measured values, each using a different scale (due to the drastic variations in scale among the models). The waterflood differences in impedance (Figure 74a) are the highest differences, ranging from -450 to -130 ((m/s)*(g/cc)) changes. The CO_2 gas-saturated substitution differences in impedance (Figure 74c) are the lowest differences, ranging from -2.3 to -2.0 ((m/s)*(g/cc)) changes. Oil substitution differences range from -280 to -85 ((m/s)*(g/cc)), and CO_2 liquid substitution differences range from -70 to -15 ((m/s)*(g/cc)). Highest to lowest substitution differences occur in the order: waterflood, oil, CO_2 liquid, and CO_2 gas, respectively.

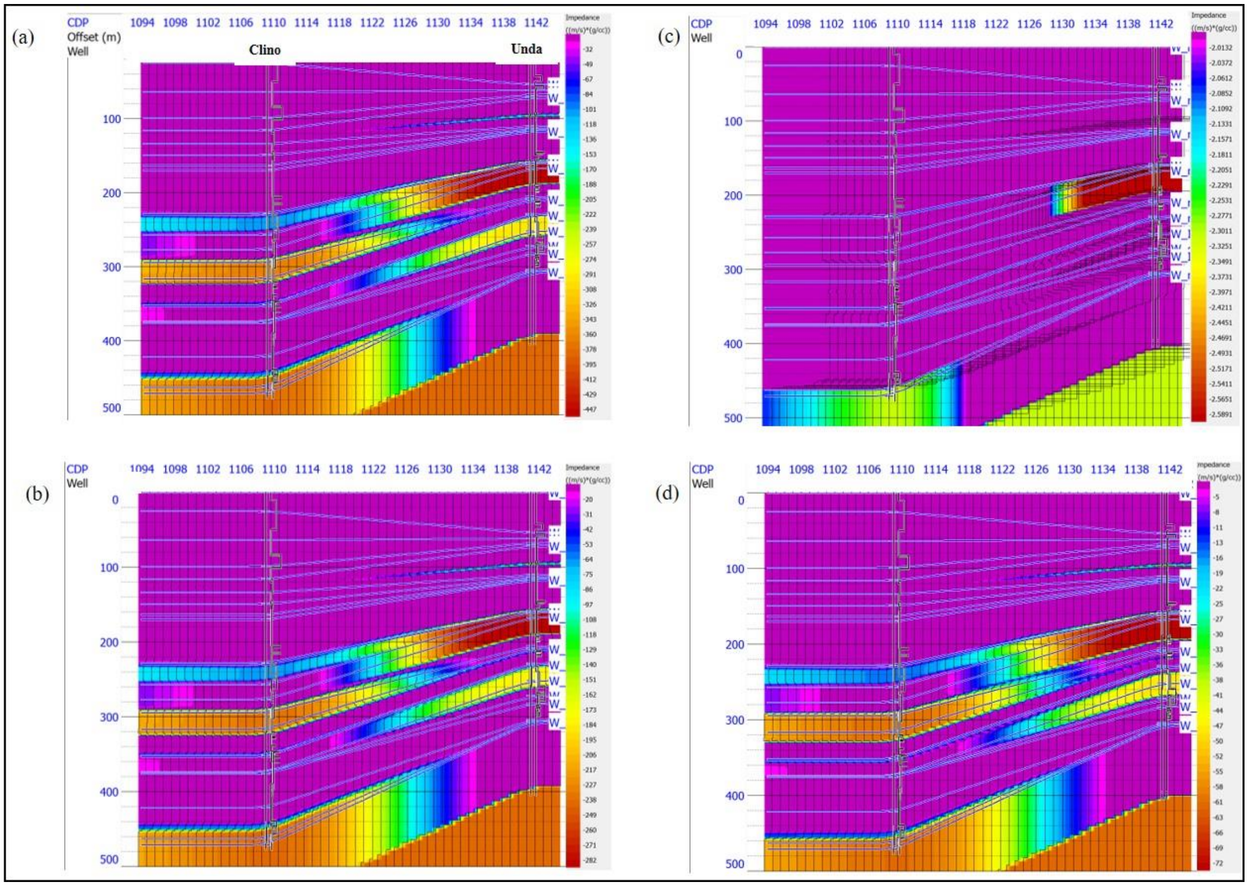

Figure 74. Differences in impedance (Z) over synthetic seismic for (a) waterflooded, (b) oil-saturated, (c) CO_2 gas-saturated, and (d) CO_2 liquid-saturated Clino and Unda cores. Each model has a different scale bar.

In Table 10, the average acoustic impedance (Z) values were calculated for each pore type in each fluid substitution model. The cemented pores had the highest impedance values, followed by moldic pores, intercrystalline pores, and lastly, microporosity pores. The highest impedance values are present in the CO_2 gas-saturated rock, followed by oil, water-flooded, and CO_2 liquid substitutions.

Porosity (%)	**Z ((m/s)*(g/cc))**				**Pore Types**
	Water	**Oil**	**CO_2 Gas**	**CO_2 Liquid**	
11.67	15265.93	13855.74	14175.22	13480.01	Cemented
44.18	5769.15	4147.80	4584.90	3310.12	Intercrystalline
45.29	4271.16	3092.83	3256.21	2306.03	Microporosity
39.40	8507.07	6016.38	6768.29	5161.39	Moldic

Table 10. Comparison of average Z for different fluid substitution models with pore types identified and average porosity.

Using Equation 5.13, the effect of CO_2 flooding calculations in Table 11 are completed, which depict the percent change of Vp, density (ρ), and impedance (Z). The highest percent change for Vp, density, and impedance was in microporosity pores and the lowest for cemented pores, for both CO_2 gas and liquid. The CO_2 flooding effect (for both gas and liquid phases) for each pore type, from highest to lowest percent change, is microporosity pores, intercrystalline pores, moldic pores, and cemented pores. The percent change is higher for CO_2 gas than for CO_2 liquid.

Porosity (%)	**CO_2 Gas Flooding Effect (Oil-CO_2 Gas)**			**CO_2 Liquid Flooding Effect (Oil-CO_2 liquid)**			**Pore Types**
	ΔVp (%)	**Δρ (%)**	**ΔZ (%)**	**ΔVp (%)**	**Δρ (%)**	**ΔZ (%)**	
11.67	-0.59	2.92	2.31	-0.49	-2.24	-2.71	Cemented
44.18	-7.52	19.61	10.54	-6.15	-15.03	-20.20	Intercrystalline
45.29	-13.21	21.40	5.28	-10.74	-16.39	-25.44	Microporosity
39.40	-2.93	16.03	12.50	-2.41	-12.28	-14.21	Moldic

Table 11. CO_2 flooding effect percent changes for average Vp, ρ, and Z, with different pore types identified.

6.4 Overall Effect of Pore Types on CO_2 Flooding

The effect of CO_2 flooding was determined using Equation 5.13, where the highest percent change, overall, was for microporosity samples. Looking at the pore types, the CO_2 flooding percent change from highest to lowest was: microporosity, intercrystalline, moldic, and cemented pores. The lowest change was in cemented pore types, due to the dense packing of their grains. On average, microporosity samples had about a -13% Vp change for CO_2 gas, whereas it was a -11% Vp change for CO_2 liquid. Of the properties, the largest percent change was for the bulk modulus of microporosity pores, with a -32% change for CO_2 gas and -26% change for CO_2 liquid. The CO_2 flooding effect percent changes were higher for CO_2 gas-saturated than for CO_2 liquid-saturated samples.

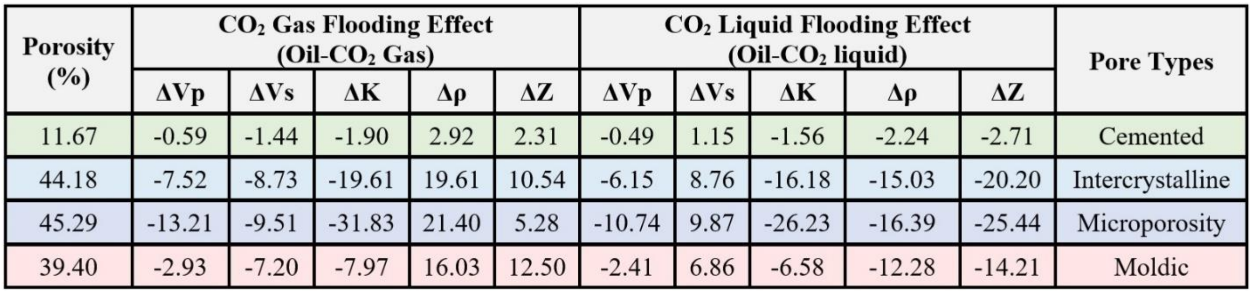

Porosity (%)	CO_2 Gas Flooding Effect (Oil-CO_2 Gas)					CO_2 Liquid Flooding Effect (Oil-CO_2 liquid)					Pore Types
	ΔVp	ΔVs	ΔK	Δρ	ΔZ	ΔVp	ΔVs	ΔK	Δρ	ΔZ	
11.67	-0.59	-1.44	-1.90	2.92	2.31	-0.49	1.15	-1.56	-2.24	-2.71	Cemented
44.18	-7.52	-8.73	-19.61	19.61	10.54	-6.15	8.76	-16.18	-15.03	-20.20	Intercrystalline
45.29	-13.21	-9.51	-31.83	21.40	5.28	-10.74	9.87	-26.23	-16.39	-25.44	Microporosity
39.40	-2.93	-7.20	-7.97	16.03	12.50	-2.41	6.86	-6.58	-12.28	-14.21	Moldic

Table 12. The CO_2 flooding effect percent changes for average Vp, Vs, K, ρ, and Z, with different pore types identified.

Comparing the samples used in the fluid substitutions with the CO_2 flooding effect, microporosity pores had the highest percent changes for all petrophysical properties. The samples used have roughly the same porosity of about 40%. With the same porosity in the samples, as well as similar mineralogy, the change in CO_2 flooding effect is caused by the change in pore type geometries.

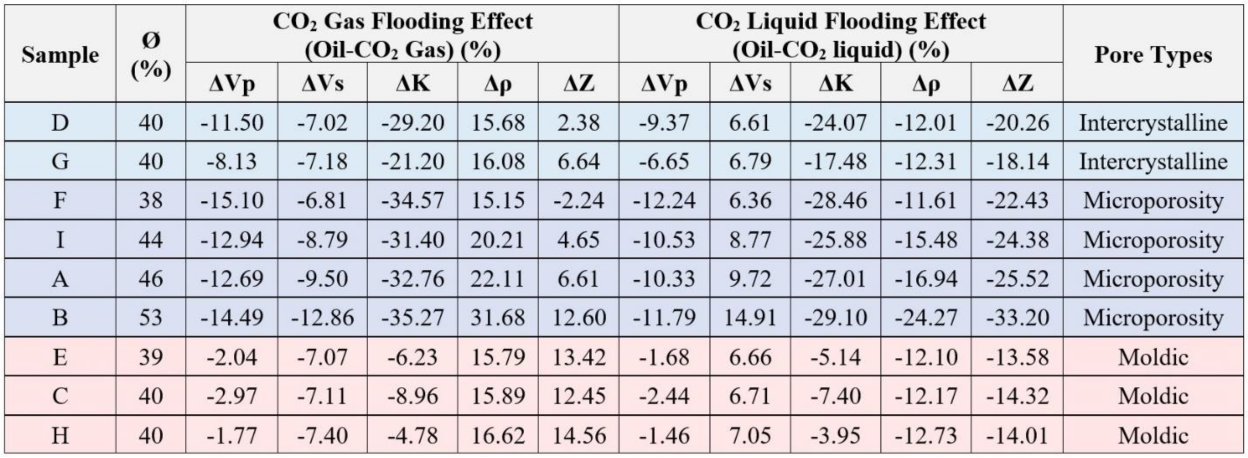

Sample	Ø (%)	CO$_2$ Gas Flooding Effect (Oil-CO$_2$ Gas) (%)					CO$_2$ Liquid Flooding Effect (Oil-CO$_2$ liquid) (%)					Pore Types
		ΔVp	ΔVs	ΔK	Δρ	ΔZ	ΔVp	ΔVs	ΔK	Δρ	ΔZ	
D	40	-11.50	-7.02	-29.20	15.68	2.38	-9.37	6.61	-24.07	-12.01	-20.26	Intercrystalline
G	40	-8.13	-7.18	-21.20	16.08	6.64	-6.65	6.79	-17.48	-12.31	-18.14	Intercrystalline
F	38	-15.10	-6.81	-34.57	15.15	-2.24	-12.24	6.36	-28.46	-11.61	-22.43	Microporosity
I	44	-12.94	-8.79	-31.40	20.21	4.65	-10.53	8.77	-25.88	-15.48	-24.38	Microporosity
A	46	-12.69	-9.50	-32.76	22.11	6.61	-10.33	9.72	-27.01	-16.94	-25.52	Microporosity
B	53	-14.49	-12.86	-35.27	31.68	12.60	-11.79	14.91	-29.10	-24.27	-33.20	Microporosity
E	39	-2.04	-7.07	-6.23	15.79	13.42	-1.68	6.66	-5.14	-12.10	-13.58	Moldic
C	40	-2.97	-7.11	-8.96	15.89	12.45	-2.44	6.71	-7.40	-12.17	-14.32	Moldic
H	40	-1.77	-7.40	-4.78	16.62	14.56	-1.46	7.05	-3.95	-12.73	-14.01	Moldic

Table 13. The CO$_2$ flooding effect percent changes for each sample used in the fluid substitution. The percent changes for Vp, Vs, K, ρ, and Z, with different pore types and porosity (Ø), are identified.

The percent changes in the CO$_2$ flooding effect for CO$_2$ gas, displays a negative change for all properties except density and impedance, where the change was positive. This may be related to the density effect. Percent changes in the CO$_2$ flooding effect for CO$_2$ liquid, shows a negative change for all properties except Vs, where the change was positive. The positive change in Vs, in CO$_2$ liquid is due to the density effect associated with the CO$_2$ phase change.

Important to know this because CO$_2$ EOR continues to be a complicated task for carbonate reservoirs in the industry. The temperature and pore pressure of CO$_2$ will behave differently for various phases, which depending on the depth of storage may exist in gaseous or liquid phase. Seismic monitoring of CO$_2$ EOR is dependent on CO$_2$ as a pore fluid, where its elastic properties can vary at large ranges dependent on depth and its pressure-temperature relationship.

6.5 Conclusion

The above figures show the synthetic seismic section with the by P-wave velocity, density, and acoustic impedance values of each fluid substitution as an overlay. High amplitudes correlate with cemented and moldic pores. Cemented and moldic pores have high density, high velocity, low porosity, high impedance values, high elastic moduli, and therefore create high amplitudes. The opposite is true for microporosity and intercrystalline samples.

Samples chosen for fluid substitution in seismic monitoring have similar porosity and mineralogy, but different pore types. This was used to test the influence of pore type geometries. Cemented pores were not included in the sample selection, as they have little to no porosity, and would not be a targeted zone for oil exploration.

Looking at the changes in Vp for the various fluid substitutions, the waterflood substitution had the highest, followed by oil, CO_2 liquid, and CO_2 gas. For density, the CO_2 gas-saturated rock had the highest fluid substitution values, followed by oil, waterflooded, and CO_2 liquid. The opposite order describes the highest to lowest substitution differences for density: CO_2 liquid, waterflooded, oil, and CO_2 gas. Impedance follows the same fluid substitution orders as density, which is due to the influence of the changes in density or the density effect.

The effect of CO_2 flooding was determined using Equation 5.13, where the highest percent change, overall, was for microporosity samples. Looking at the pore types, the CO_2 flooding percent change from highest to lowest was: microporosity, intercrystalline, moldic, and cemented pores. The lowest change was in cemented pore types, due to the dense packing of their grains. As CO_2 EOR continues to be a complicated task for carbonate reservoirs in the industry, the results of this study will be influential to effectively model the elastic properties of rocks saturated in CO_2. The temperature and pore pressure of CO_2 behaves differently for various phases - depending on the depth of storage may exist in gaseous or liquid phase. Seismic monitoring of CO_2 EOR is dependent on CO_2 as a pore fluid, where its elastic properties can vary at large ranges dependent on depth and its pressure-temperature relationship.

7. OVERALL CONCLUSION AND DISCUSSION

7.1 Conclusions and Synopsis

For this study, the research objectives were to answer the following questions: (1) How do carbonate rock pore types influence the petrophysical properties?, (2) Can knowledge of carbonate rock pore types be used to predict seismic monitoring of CO_2 sequestration?, and (3) How can better carbonate rock pore type knowledge improve production with CO_2 EOR? This research was completed through the (1) characterization and identification of different carbonate rock pore types based on 46 samples from the Clino and Unda cores in the GBB, (2) identification of elastic properties of the pore geometries using rock physics models, and (3) creating an analysis of the influence of carbonate rock pore types on CO_2 sequestration through seismic monitoring. The theoretical results of this quantitative study are designed to provide a better understanding of the influence of carbonate rock pore types on seismic monitoring of CO_2 flooding in carbonate reservoirs.

No correlation was observed between mineralogy and velocity, as a result of similar physical properties in the mineral composition of the samples. A relationship between high velocities and shallow-water depositional environments was determined, as porosity and diagenetic processes in shallow-water result in high velocities and elastic moduli. Carbonate rock pore types influence the petrophysical properties, as rocks with the same porosity can have very different velocities. Cemented and moldic pores have low porosity, high velocity, low permeability, high density, high bulk and shear moduli, low frame flexibility factors, high pore stiffness values, high impedance values, positive amplitudes in seismic, and the lowest percent change in CO_2 flooding. The opposite is true for microporosity and intercrystalline pores.

Two key parameters for reservoir characterization are porosity and permeability, which can be complicated to estimate in carbonate rock reservoirs. Using rock physics models, like the Sun (2000) model, the elastic properties important for carbonate rock reservoir characterization can be considered. Frame flexibility factors offer a structural representation of the pore, where high frame flexibility factors are associated with rocks that have more grain coupling and contacts, such as intercrystalline and microporosity samples. Low frame flexibility factors relate to a rigid rock frame, present in cemented and moldic pore types. The stiffness (f) and rigidity (f_μ) factors are also useful in characterizing pore types and reservoir rock properties, as lower values are associated with microporous and intercrystalline rocks. These pore types deform easily under compressional and shear motion, whereas moldic and cemented rocks are insensitive to stress and show high stiffness/rigidity values. Using a combination of the Sun model and pore space stiffness model may aid in determining low permeable carbonate rocks from highly permeable rocks. This is because the pore space stiffness increases with decreasing frame flexibility factors for a given porosity.

For effective seismic monitoring of CO_2 sequestration, it is important to know that CO_2 flooding causes a decrease in Vp and bulk modulus. In general, average microporosity samples had about a -13% Vp change for CO_2 gas, whereas it was a -11% Vp change for CO_2 liquid. Of the petrophysical properties, the largest percent change was for the bulk modulus of microporosity pores, with a -32% change for CO_2 gas and -26% change for CO_2 liquid. CO_2 liquid flooding causes an increase in Vs due to the density effect. Overall, the highest percent change was in microporosity pores for both CO_2 phases, whereas the lowest percent change for petrophysical properties was in cemented pores. The CO_2 flooding percent change from highest to lowest was: microporosity, intercrystalline, moldic, and cemented pores. The lowest change was in cemented pore types, due to the dense packing of their grains. The CO_2 flooding effect percent changes were higher for CO_2 gas-saturated than for CO_2 liquid-saturated samples. With the samples having the same porosity of about 40%, as well as similar mineralogical composition properties, the change in CO_2 flooding effect is caused by the change in pore type geometries.

For CO_2 gas, the percent changes in the CO_2 flooding effect displays a negative change for all properties except density and impedance, where the change was positive. The CO_2 flooding effect percent changes for CO_2 liquid, shows a negative change for all properties except Vs, where the change was positive. The changes that occur with CO_2 flooding are due to the density effect associated with the CO_2 phase changes.

All the assumptions by Gassmann's equation is in violation with carbonate rocks, therefore certain errors may be present in these theoretical results. It is important to acknowledge that CO_2 is not an inert fluid, meaning it can react with the rock matrix and lead to secondary porosities from an alteration or dissolution of the rock frame. There is also a significant violation of Gassmann's assumption of a constant shear modulus in carbonate rocks. Shear modulus actually does change with saturation, as the grain contacts in carbonate rocks can stiffen or weaken with fluid changes in the pores. It is possible that Gassmann's fluid substitution model may underpredict the time-lapse changes caused by fluid substitution, as the Gassmann equation assumes a constant porosity and shear modulus. Further experimental studies are needed to confirm with our theoretical results.

Knowing the changes related to pore types in CO_2 flooding is important, because CO_2 flooding continues to be a complicated task in relation to oil exploration of carbonate reservoirs. The temperature and pore pressure of CO_2 will behave differently for various phases, which depending on the depth of storage may exist in gaseous or liquid phase. Seismic monitoring of

CO_2 EOR is dependent on CO_2 as a pore fluid, where its elastic properties can vary at large ranges dependent on depth and its pressure-temperature relationship. The results of this thesis provide significant conclusions that could be used as a guide for future researches on time-lapse seismic monitoring of carbonate rocks following CO_2 sequestration.

REFERENCES

Anselmetti, F.S. and G.P. Eberli, 1993, Controls on sonic velocity in carbonates: Pure and Applied Geophysics, **141**, 287-323.

Anselmetti, F. S., G. A. von Salis, K. J. Cunningham, and G. P. Eberli, 1997, Acoustic properties of Neogene carbonates and siliciclastics from the subsurface of the Florida Keys: Implications for seismic reflectivity: Marine Geology, **144**, 9–31.

Anselmetti, F.S. and G.P. Eberli, 1999, The Velocity-Deviation Log: A Tool to Predict Pore Type and Permeability Trends in Carbonate Drill Holes from Sonic and Porosity or Density Logs: AAPG Bulletin, **83**, 450-466.

Anselmetti, F.S. and G.P. Eberli, 2001, Sonic velocity in carbonates–a combined product of depositional lithology and diagenetic alterations, *in* R.N. Ginsburg, eds., Subsurface Geology of a Prograding Carbonate Platform Margin, Great Bahama Bank: Results of the Bahamas Drilling Project, 191-216.

Baechle, G.T., G.P. Eberli, R.J. Weger, and J.L. Massaferro, 2009, Changes in dynamic shear moduli of carbonate rocks with fluid substitution, Society of Exploration Geophysicists (SEG), **74**, E135-E147.

Biot, M.A., 1956, Theory of propagation of elastic waves in a fluid-saturated porous solid. I. low-frequency range: The Journal of the Acoustical Society of America, **28**, 168-178.

Carew, J.L. and J.E. Mylroie, 1997, Geology of the Bahamas: Geology and Hydrogeology of Carbonate Islands, **1**, p. 91–139.

Choquette, P. W., and L.C. Pray, 1970, Geologic nomenclature and classification of porosity in sedimentary carbonates: American Association of Petroleum Geologists (AAPG), **54**, 107–250.

Davidson, Daniel, 2013, A Rock Physics Based Investigation of Pore Structure Variations Associated with a CO_2 Flood in a Clastic Reservoir, Delhi, LA. Master's thesis, Texas A&M University. Available electronically from http://hdl.handle.net/1969.1/151283.

Eberli, G.P. and R. N. Ginsburg, 1989, Cenozoic Progradation of Northwestern Great Bahama Bank, A Record of Lateral Platform Growth and Sea-Level Fluctuations: The Society of Economic Paleontologists and Mineralogists (SEPM), **44**, 339-351.

Eberli, G.P., P.K. Swart, D.f. McNeill, J.A.M. Kenter, F.S. Anselmetti, L.A. Melim, and R. N. Ginsburg, 1997, A Synopsis of the Bahamas Drilling Project: Results from two deep core borings drilled on the Great Bahamas Bank: Ocean Drilling Program, **166**, 23-41.

Gassmann, F., 1951, Elastic waves through a packing of spheres: Geophysics, **16**, 673- 685.

Ginsburg, R.N., 2001, The Bahamas Drilling Project: Background and Acquisition of Cores and Logs, *in* R.N. Ginsburg, eds., Subsurface Geology of a Prograding Carbonate Platform Margin, Great Bahama Bank: Results of the Bahamas Drilling Project, 3-13.

Harris, P.M., 1986, Depositional Environments of Carbonate Platforms: Colorado School of Mines, **1**, 31-60.

Hill, R., 1952, The elastic behavior of a crystalline aggregate: Proceedings of the Physical Society, **65**, 349.

Mammadova, Elnara, 2011, Influence of Rock Types on Seismic Monitoring of CO_2 Sequestration in Carbonate Reservoirs. Master's thesis, Texas A&M

University. Available electronically from http://hdl.handle.net/1969.1/ETD-TAMU-2011-08-10019.

Massaferro, J.L., F.S. Anselmetti, G.P. Eberli, G.T. Baechle, G.B. Gartner, and Y.F. Sun, 2002, Effects on pore types on velocity and permeability in carbonates: Shell International Exploration and Production B.V., 37-39.

Mavko, G. and T. Mukerji, 1995, Seismic pore space compressibility and Gassmann's relation: Geophysics, **60**, 1743-1749.

Melim, L., F. Anselmetti, and G. Eberli, 2001, The Importance of Pore Type of Permeability of Neogene Carbonates, Great Bahama Bank: Society for Sedimentary Geology (SEPM), **70**, 217-238.

Meyerhoff, A.A. and C.W. Hatten, 1974, Bahamas salient of North America: The Geology of Continental Margins, **1**, 429--446.

Preston, C., M. Monea, W. Jazrawi, K. Brown, S. Whittaker, et al., 2005, IEA GHG Weyburn CO_2 Monitoring and Storage Project. *Fuel Processing Technology*, 1547-1568.

Reuss, A., 1929, Berechnung der Fliessgrenze von Mischkristallen auf Grund der Plastizitätsbedingung für Einkristalle: ZAMM—Journal of Applied Mathematics, **9**, 49.

Russell, B. and T. Smith, 2007, The relationship between dry rock bulk modulus and porosity – An empirical study: CREWES Research Report, **19**, 1-14.

Schlumberger, 2007, Carbonate Reservoirs, http://www.slb.com/~/media/Files/industry_challenges/carbonates/brochures/cb_carbonate_reservoirs_07os003.ashx, accessed 8 January 2019.

Stalkup, F., 1978, Carbon Dioxide Miscible Flooding: Past, Present, and Outlook for the Future. *Journal of Petroleum*, 1102-1112.

Sun, Y.F., 2000, Core-log-seismic integration in hemipelagic marine sediments on the eastern flank of the Juan de Fuca Ridge: Ocean Drilling Program, Scientific results, **168**, 21-35.

Sun, Y.F., 2004, Pore structure effects on elastic wave propagation in rocks: AVO modeling: Journal of Geophysics and Engineering, **1**, 269-276.

U.S. Department of Energy, 2018, Enhanced Oil Recovery, https://www.energy.gov/fe/science-innovation/oil-gas-research/enhanced-oil-recovery, accessed 10 February 2019.

Vanorio, T., G. Mavko, S. Vialle, and K. Spratt, 2010, The rock physics basis for 4D seismic monitoring of CO_2 fate: Are we there yet?: The Leading Edge, **29**, 156-162.

Voigt, W., 1928, Lehrbuch der Kristallphysik: Leipzig, **1**, 739.

Wang, Z. and A.M. Nur, 1989, Effects of CO_2 flooding on wave velocities in rocks with hydrocarbons: SPE Reservoir Engineering, **4**, 429-436.

Wang, Z., M. Cates, and R. Langan, 1998, Seismic monitoring of a CO_2 flood in a carbonate reservoir: A rock physics study: Society of Exploration Geophysicists (SEG), **63**, 1604-1617.

Wyllie, M.R., A.R. Gregory, and G.H.F. Gardner, 1958, An experimental investigation of factors affecting elastic wave velocities in porous media: Geophysics, **23**, 459-493.

APPENDIX A

Table shows mineralogical composition with velocities and pore types of samples.

Table of Sample Mineralogical Composition with Velocities and Pore Type						
Sample	**Calcite (%)**	**Aragonite (%)**	**Dolomite (%)**	**Vp (m/s)**	**Vs (m/s)**	**Pore Type**
1	90	10	0	6200	3300	Cemented
2	100	0	0	5818	2930	Cemented
3	100	0	0	5953	3187	Cemented
4	100	0	0	5953	3187	Cemented
5	100	0	0	5775	3208.333	Cemented
6	100	0	0	5775	3208.333	Cemented
7	38	2	60	2900	1400	Intercrystalline
8	0	0	100	2670	1700	Intercrystalline
9	70	10	20	3000	1364	Intercrystalline
10	35	5	60	2610	1300	Intercrystalline
11	65	30	5	2900	1407.767	Intercrystalline
12	40	0	60	2450	1220	Intercrystalline
13	38	2	60	3100	1500	Intercrystalline
14	0	0	100	3645	1695.349	Intercrystalline
15	40	60	0	2100	941.704	Microporosity
16	100	0	0	2100	941.704	Microporosity
17	88	10	2	2100	950	Microporosity
18	58	40	2	2100	950	Microporosity
19	45	50	5	2200	1050	Microporosity
20	80	20	0	2219	1077.184	Microporosity
21	85	5	10	2289	1099	Microporosity
22	95	0	5	2310	1137	Microporosity
23	95	2	3	2390	1178	Microporosity
24	83	2	15	2515	1153.67	Microporosity
25	90	5	5	2400	1079	Microporosity
26	100	0	0	2000	1000	Microporosity
27	100	0	0	2000	1000	Microporosity
28	100	0	0	2010	1050	Microporosity
29	80	10	10	2100	970.7692	Microporosity
30	85	5	10	2475	1289.063	Microporosity
31	85	5	10	2200	1145.833	Microporosity
32	85	5	10	2000	934.728	Microporosity
33	95	0	5	2000	910	Microporosity
34	80	0	20	2000	990	Microporosity

Table of Sample Mineralogical Composition with Velocities and Pore Type

Sample	Calcite (%)	Aragonite (%)	Dolomite (%)	Vp (m/s)	Vs (m/s)	Pore Type
35	83	2	15	2100	1055	Microporosity
36	90	5	5	2100	950	Microporosity
37	90	10	0	4334	2121	Moldic
38	100	0	0	4755	2186	Moldic
39	85	5	10	4436	2323	Moldic
40	55	5	40	3692	1871	Moldic
41	90	5	5	3459	1703.941	Moldic
42	55	0	45	3692	1871	Moldic
43	95	2	3	3900	1850	Moldic
44	20	0	80	4110	2163	Moldic
45	88	2	10	4373	1987	Moldic
46	90	5	5	3750	1849	Moldic

APPENDIX B

Table shows calculated bulk and shear modulus for measured sample data, with pore types identified.

Table with Calculated Bulk and Shear Modulus

Sample	Vp (m/s)	Vs (m/s)	Density (g/cc)	Bulk Modulus (GPa)	Shear Modulus (GPa)	Pore Type
1	6200	3300	2.5	56.00648	21.46225	Cemented
2	5818	2930	2.594	62.04848	28.24866	Cemented
3	5953	3187	2.5	54.73896	25.39242	Cemented
4	5953	3187	2.6	56.92852	26.40812	Cemented
5	5775	3208.333	2.65	52.00913	27.27752	Cemented
6	5775	3208.333	2.65	52.00913	27.27752	Cemented
7	2900	1400	1.92	6.289088	5.5488	Intercrystalline
8	2670	1700	1.99	11.53537	3.9004	Intercrystalline
9	3000	1364	1.92	8.752832	3.2448	Intercrystalline
10	2610	1300	1.99	12.97348	3.702387	Intercrystalline
11	2900	1407.767	2.05	8.236832	3.05122	Intercrystalline
12	2450	1220	1.98	11.41983	3.92398	Intercrystalline
13	3100	1500	1.98	18.71842	5.690931	Intercrystalline
14	3645	1695.349	2.03	13.4183	4.5675	Intercrystalline
15	2100	941.704	1.95	5.2	1.95	Microporosity
16	2100	941.704	1.98	6.390631	1.755877	Microporosity
17	2100	950	1.9	5.066667	1.9	Microporosity
18	2100	950	2.08	6.71339	1.844558	Microporosity
19	2200	1050	1.9	4.88319	2.09475	Microporosity
20	2219	1077.184	1.95	6.253	1.759875	Microporosity
21	2289	1099	1.95	6.149278	1.837666	Microporosity
22	2310	1137	2.01	6.4454	1.814025	Microporosity
23	2390	1178	2	7.820098	3.323364	Microporosity
24	2515	1153.67	1.99	6.7063	2.193975	Microporosity
25	2400	1079	1.98	6.117054	2.599609	Microporosity
26	2000	1000	1.98	6.686181	2.297446	Microporosity
27	2000	1000	2.12	6.010295	1.852279	Microporosity
28	2010	1050	1.98	7.185657	2.391446	Microporosity
29	2100	970.7692	2.12	6.139237	1.755572	Microporosity
30	2475	1289.063	1.99	7.188692	2.57261	Microporosity
31	2200	1145.833	1.84	4.955488	1.803384	Microporosity
32	2000	934.728	1.97	7.607854	2.733737	Microporosity
33	2000	910	1.84	5.383779	2.047966	Microporosity

Table with Calculated Bulk and Shear Modulus						
Sample	**Vp (m/s)**	**Vs (m/s)**	**Density (g/cc)**	**Bulk Modulus (GPa)**	**Shear Modulus (GPa)**	**Pore Type**
34	2000	990	1.97	8.964721	2.621979	Microporosity
35	2100	1055	1.92	6.1568	1.7328	Microporosity
36	2100	950	1.91	8.036666	2.2237	Microporosity
37	4334	2121	2.15	34.91291	10.27398	Moldic
38	4755	2186	2.08	26.59357	9.357173	Moldic
39	4436	2323	1.95	17.47852	6.82625	Moldic
40	3692	1871	2.15	26.83843	11.60211	Moldic
41	3459	1703.941	2	17.92669	7.001282	Moldic
42	3692	1871	2	16.18692	5.806829	Moldic
43	3900	1850	2.18	23.22574	10.19928	Moldic
44	4110	2163	2.09	22.25153	7.153025	Moldic
45	4373	1987	2.15	20.43381	7.350422	Moldic
46	3750	1849	2.2	30.48959	8.685972	Moldic

APPENDIX C

Table shows frame flexibility factors for water-saturated rocks with pore types identified.

Water-Saturated								
Sample	**Φk**	**Fk**	**Frame stiffness (f)**	**Frame stiffness (fμ)**	**Frame flexibility (γ)**	**Frame flexibility (γμ)**	**Ratio of (γμ/γ)**	**Pore type**
1	0.265	1.896	0.846	0.780	2.111	2.648	1.255	cement1
2	0.144	1.806	0.926	0.941	1.924	1.734	0.901	cement1
3	0.281	2.004	0.827	0.923	2.262	1.533	0.678	cement2
4	0.254	1.817	0.860	0.960	2.002	1.273	0.636	cement2
5	0.305	3.050	0.750	0.947	3.724	1.515	0.407	cement3
6	0.305	3.050	0.750	0.947	3.724	1.515	0.407	cement3
7	0.907	1.881	0.139	0.273	4.000	2.974	0.744	intercrystalline1
8	0.804	1.748	0.323	0.209	2.834	3.540	1.250	intercrystalline1
9	0.877	1.820	0.200	0.158	3.454	3.805	1.102	intercrystalline2
10	0.811	1.726	0.322	0.200	2.784	3.537	1.270	intercrystalline2
11	0.887	2.217	0.145	0.113	4.787	5.268	1.101	Intercrystalline3
12	0.843	2.107	0.220	0.166	3.960	4.516	1.140	Intercrystalline3
13	0.786	1.872	0.340	0.218	2.982	3.796	1.273	Intercrystalline4
14	0.823	1.960	0.268	0.200	3.417	3.956	1.158	Intercrystalline4
15	0.906	1.969	0.125	0.113	4.374	4.541	1.038	microporosity1
16	0.852	1.936	0.204	0.087	3.740	5.211	1.393	microporosity1
17	0.913	1.827	0.129	0.112	3.955	4.154	1.050	microporosity10
18	0.879	2.313	0.139	0.091	5.126	6.005	1.172	microporosity10
19	0.912	1.825	0.129	0.127	3.954	3.973	1.005	microporosity11
20	0.892	1.982	0.148	0.099	4.192	4.876	1.163	microporosity11
21	0.895	1.945	0.148	0.106	4.102	4.637	1.130	microporosity2
22	0.890	2.069	0.144	0.094	4.449	5.205	1.170	microporosity2
23	0.875	1.901	0.188	0.192	3.712	3.675	0.990	microporosity3
24	0.884	2.009	0.158	0.119	4.180	4.669	1.117	microporosity3
25	0.892	1.938	0.152	0.142	4.054	4.162	1.027	microporosity4
26	0.886	2.014	0.155	0.128	4.215	4.543	1.078	microporosity4
27	0.881	2.482	0.122	0.086	5.800	6.599	1.138	microporosity5
28	0.874	1.987	0.175	0.130	4.002	4.520	1.129	microporosity5
29	0.879	2.477	0.124	0.081	5.752	6.721	1.169	microporosity6
30	0.854	1.941	0.206	0.132	3.726	4.496	1.207	microporosity6
31	0.915	1.727	0.138	0.115	3.624	3.868	1.067	microporosity7
32	0.846	1.799	0.241	0.144	3.241	4.058	1.252	microporosity7

Water-Saturated								
Sample	**Φk**	**Fk**	**Frame stiffness (f)**	**Frame stiffness (fμ)**	**Frame flexibility (γ)**	**Frame flexibility (γμ)**	**Ratio of (γμ/γ)**	**Pore type**
33	0.911	1.719	0.147	0.134	3.538	3.664	1.036	microporosity8
34	0.847	1.802	0.245	0.149	3.215	4.003	1.245	microporosity8
35	0.901	1.865	0.148	0.098	3.893	4.524	1.162	microporosity9
36	0.872	1.856	0.198	0.125	3.549	4.270	1.203	microporosity9
37	0.536	1.674	0.667	0.472	2.051	2.946	1.436	moldic1
38	0.621	1.680	0.579	0.455	2.181	2.704	1.240	moldic1
39	0.769	1.729	0.387	0.332	2.613	2.873	1.099	moldic2
40	0.637	1.633	0.575	0.569	2.118	2.142	1.011	moldic2
41	0.773	1.736	0.382	0.338	2.636	2.842	1.078	moldic3
42	0.768	1.785	0.375	0.310	2.744	3.085	1.124	moldic3
43	0.730	1.824	0.425	0.405	2.675	2.771	1.036	moldic4
44	0.691	1.869	0.461	0.350	2.676	3.274	1.223	moldic4
45	0.710	1.919	0.429	0.355	2.834	3.243	1.144	moldic5
46	0.599	1.498	0.653	0.435	1.833	2.628	1.434	moldic5

APPENDIX D

Table shows frame flexibility factors for oil-saturated rocks with pore types identified.

Oil-Saturated								
Sample	Φk	Fk	Frame stiffness (f)	Frame stiffness (fμ)	Frame flexibility (γ)	Frame flexibility (γμ)	Ratio of (γμ/γ)	Pore type
1	0.279	1.991	0.831	0.780	2.226	2.648	1.190	cement1
2	0.152	1.897	0.918	0.941	2.021	1.734	0.858	cement1
3	0.296	2.112	0.810	0.923	2.396	1.533	0.640	cement2
4	0.267	1.904	0.846	0.960	2.106	1.273	0.605	cement2
5	0.332	3.319	0.722	0.947	4.092	1.515	0.370	cement3
6	0.332	3.319	0.722	0.947	4.092	1.515	0.370	cement3
7	0.946	1.964	0.068	0.273	5.091	2.974	0.584	intercrystalline1
8	0.847	1.842	0.247	0.209	3.269	3.540	1.083	intercrystalline1
9	0.915	1.899	0.131	0.158	4.094	3.805	0.929	intercrystalline2
10	0.848	1.805	0.256	0.200	3.144	3.537	1.125	intercrystalline2
11	0.930	2.325	0.078	0.113	5.983	5.268	0.880	Intercrystalline3
12	0.885	2.213	0.155	0.166	4.655	4.516	0.970	Intercrystalline3
13	0.818	1.947	0.290	0.218	3.274	3.796	1.159	Intercrystalline4
14	0.862	2.051	0.207	0.200	3.894	3.956	1.016	Intercrystalline4
15	0.954	2.073	0.042	0.113	6.136	4.541	0.740	microporosity1
16	0.913	2.076	0.098	0.087	5.014	5.211	1.039	microporosity1
17	0.956	1.912	0.048	0.112	5.375	4.154	0.773	microporosity10
18	0.934	2.458	0.055	0.091	7.049	6.005	0.852	microporosity10
19	0.957	1.914	0.045	0.127	5.474	3.973	0.726	microporosity11
20	0.939	2.087	0.067	0.096	5.514	4.876	0.884	microporosity11
21	0.941	2.045	0.067	0.106	5.380	4.637	0.862	microporosity2
22	0.938	2.182	0.064	0.094	5.888	5.205	0.884	microporosity2
23	0.919	1.997	0.111	0.192	4.563	3.675	0.806	microporosity3
24	0.932	2.119	0.077	0.119	5.424	4.669	0.861	microporosity3
25	0.939	2.042	0.069	0.142	5.337	4.162	0.780	microporosity4
26	0.934	2.122	0.075	0.128	5.470	4.543	0.830	microporosity4
27	0.942	2.655	0.032	0.086	8.832	6.599	0.747	microporosity5
28	0.923	2.098	0.093	0.130	5.099	4.520	0.886	microporosity5
29	0.941	2.650	0.035	0.081	8.632	6.721	0.779	microporosity6
30	0.909	2.067	0.112	0.132	4.783	4.496	0.940	microporosity6
31	0.956	1.805	0.055	0.115	4.849	3.868	0.798	microporosity7
32	0.898	1.910	0.146	0.144	4.029	4.058	1.007	microporosity7

Oil-Saturated								
Sample	**Φk**	**Fk**	**Frame stiffness (f)**	**Frame stiffness (fμ)**	**Frame flexibility (γ)**	**Frame flexibility (γμ)**	**Ratio of (γμ/γ)**	**Pore type**
33	0.952	1.795	0.066	0.134	4.593	3.664	0.797	microporosity8
34	0.892	1.898	0.165	0.149	3.842	4.003	1.042	microporosity8
35	0.943	1.953	0.071	0.098	5.004	4.524	0.904	microporosity9
36	0.915	1.947	0.122	0.125	4.315	4.270	0.990	microporosity9
37	0.559	1.747	0.635	0.472	2.179	2.946	1.352	moldic1
38	0.650	1.757	0.536	0.455	2.348	2.704	1.152	moldic1
39	0.802	1.802	0.331	0.332	2.875	2.873	0.999	moldic2
40	0.664	1.702	0.533	0.569	2.271	2.142	0.943	moldic2
41	0.804	1.808	0.328	0.338	2.893	2.842	0.982	moldic3
42	0.804	1.870	0.315	0.310	3.056	3.085	1.009	moldic3
43	0.759	1.898	0.379	0.405	2.897	2.771	0.956	moldic4
44	0.726	1.961	0.410	0.350	2.931	3.274	1.117	moldic4
45	0.747	2.018	0.374	0.355	3.131	3.243	1.036	moldic5
46	0.622	1.554	0.618	0.435	1.943	2.628	1.353	moldic5

APPENDIX E

Table shows frame flexibility factors for CO_2 gas-saturated rocks with pore types identified.

CO_2 Gas-Saturated Frame Flexibility Factors								
Sample	**Φk**	**Fk**	**Frame stiffness (f)**	**Frame stiffness ($f\mu$)**	**Frame flexibility (γ)**	**Frame flexibility ($\gamma\mu$)**	**Ratio of ($\gamma\mu/\gamma$)**	**Pore type**
1	0.27	1.95	0.85	0.78	2.11	2.65	1.25	cement1
2	0.15	1.85	0.93	0.94	1.92	1.73	0.90	cement1
3	0.29	2.07	0.83	0.92	2.26	1.53	0.68	cement2
4	0.26	1.86	0.86	0.96	2.00	1.27	0.64	cement2
5	0.32	3.25	0.75	0.95	3.73	1.52	0.41	cement3
6	0.32	3.25	0.75	0.95	3.73	1.52	0.41	cement3
7	0.93	1.93	0.14	0.27	4.01	2.97	0.74	intercrystalline1
8	0.83	1.80	0.32	0.21	2.84	3.54	1.25	intercrystalline1
9	0.90	1.86	0.20	0.16	3.46	3.80	1.10	intercrystalline2
10	0.83	1.76	0.32	0.20	2.79	3.54	1.27	intercrystalline2
11	0.91	2.28	0.14	0.11	4.80	5.27	1.10	Intercrystalline3
12	0.87	2.17	0.22	0.17	3.97	4.52	1.14	Intercrystalline3
13	0.80	1.91	0.34	0.22	2.99	3.80	1.27	Intercrystalline4
14	0.84	2.01	0.27	0.20	3.42	3.96	1.16	Intercrystalline4
15	0.93	2.03	0.12	0.11	4.39	4.54	1.03	microporosity1
16	0.89	2.01	0.20	0.09	3.75	5.21	1.39	microporosity1
17	0.94	1.87	0.13	0.11	3.97	4.15	1.05	microporosity10
18	0.91	2.41	0.14	0.09	5.14	6.01	1.17	microporosity10
19	0.94	1.87	0.13	0.13	3.97	3.97	1.00	microporosity11
20	0.92	2.04	0.15	0.10	4.20	4.88	1.16	microporosity11
21	0.92	2.00	0.15	0.11	4.11	4.64	1.13	microporosity2
22	0.92	2.14	0.14	0.09	4.46	5.21	1.17	microporosity2
23	0.90	1.95	0.19	0.19	3.72	3.68	0.99	microporosity3
24	0.91	2.07	0.16	0.12	4.19	4.67	1.11	microporosity3
25	0.92	2.00	0.15	0.14	4.07	4.16	1.02	microporosity4
26	0.91	2.08	0.15	0.13	4.23	4.54	1.07	microporosity4
27	0.92	2.60	0.12	0.09	5.82	6.60	1.13	microporosity5
28	0.90	2.05	0.17	0.13	4.01	4.52	1.13	microporosity5
29	0.92	2.59	0.12	0.08	5.77	6.72	1.16	microporosity6
30	0.89	2.01	0.20	0.13	3.74	4.50	1.20	microporosity6
31	0.94	1.77	0.14	0.11	3.63	3.87	1.06	microporosity7
32	0.87	1.86	0.24	0.14	3.25	4.06	1.25	microporosity7

CO_2 Gas-Saturated Frame Flexibility Factors								
Sample	**Φk**	**Fk**	**Frame stiffness (f)**	**Frame stiffness (fμ)**	**Frame flexibility (γ)**	**Frame flexibility (γμ)**	**Ratio of (γμ/γ)**	**Pore type**
33	0.93	1.76	0.15	0.13	3.55	3.66	1.03	microporosity8
34	0.87	1.85	0.24	0.15	3.22	4.00	1.24	microporosity8
35	0.92	1.91	0.15	0.10	3.90	4.52	1.16	microporosity9
36	0.90	1.90	0.20	0.13	3.56	4.27	1.20	microporosity9
37	0.55	1.71	0.67	0.47	2.05	2.95	1.44	moldic1
38	0.64	1.72	0.58	0.46	2.18	2.70	1.24	moldic1
39	0.79	1.77	0.39	0.33	2.62	2.87	1.10	moldic2
40	0.65	1.66	0.57	0.57	2.12	2.14	1.01	moldic2
41	0.79	1.77	0.38	0.34	2.64	2.84	1.08	moldic3
42	0.79	1.83	0.37	0.31	2.75	3.08	1.12	moldic3
43	0.75	1.86	0.42	0.40	2.68	2.77	1.03	moldic4
44	0.71	1.92	0.46	0.35	2.68	3.27	1.22	moldic4
45	0.73	1.97	0.43	0.35	2.84	3.24	1.14	moldic5
46	0.61	1.52	0.65	0.44	1.83	2.63	1.43	moldic5

APPENDIX F

Table shows frame flexibility factors for CO_2 liquid-saturated rocks with pore types identified.

CO_2 Liquid-Saturated Frame Flexibility Factors

Sample	Φk	Fk	Frame stiffness (f)	Frame stiffness ($f\mu$)	Frame flexibility (γ)	Frame flexibility ($\gamma\mu$)	Ratio of ($\gamma\mu/\gamma$)	Pore type
1	0.27	1.96	0.84	0.78	2.13	2.65	1.24	cement1
2	0.15	1.86	0.92	0.94	1.94	1.73	0.89	cement1
3	0.29	2.07	0.82	0.92	2.29	1.53	0.67	cement2
4	0.26	1.87	0.86	0.96	2.02	1.27	0.63	cement2
5	0.33	3.26	0.75	0.95	3.79	1.52	0.40	cement3
6	0.33	3.26	0.75	0.95	3.79	1.52	0.40	cement3
7	0.93	1.93	0.13	0.27	4.14	2.97	0.72	intercrystalline1
8	0.83	1.80	0.31	0.21	2.90	3.54	1.22	intercrystalline1
9	0.90	1.87	0.19	0.16	3.55	3.80	1.07	intercrystalline2
10	0.83	1.77	0.31	0.20	2.84	3.54	1.24	intercrystalline2
11	0.92	2.29	0.13	0.11	4.95	5.27	1.06	Intercrystalline3
12	0.87	2.18	0.21	0.17	4.06	4.52	1.11	Intercrystalline3
13	0.81	1.92	0.33	0.22	3.03	3.80	1.25	Intercrystalline4
14	0.85	2.02	0.26	0.20	3.49	3.96	1.13	Intercrystalline4
15	0.94	2.04	0.11	0.11	4.57	4.54	0.99	microporosity1
16	0.89	2.02	0.19	0.09	3.90	5.21	1.34	microporosity1
17	0.94	1.88	0.11	0.11	4.12	4.15	1.01	microporosity10
18	0.92	2.41	0.12	0.09	5.35	6.01	1.12	microporosity10
19	0.94	1.88	0.11	0.13	4.13	3.97	0.96	microporosity11
20	0.92	2.05	0.13	0.10	4.36	4.88	1.12	microporosity11
21	0.92	2.01	0.13	0.11	4.26	4.64	1.09	microporosity2
22	0.92	2.14	0.13	0.09	4.63	5.21	1.12	microporosity2
23	0.90	1.96	0.17	0.19	3.83	3.68	0.96	microporosity3
24	0.92	2.08	0.14	0.12	4.34	4.67	1.08	microporosity3
25	0.92	2.00	0.14	0.14	4.22	4.16	0.99	microporosity4
26	0.92	2.08	0.14	0.13	4.38	4.54	1.04	microporosity4
27	0.93	2.61	0.11	0.09	6.11	6.60	1.08	microporosity5
28	0.91	2.06	0.16	0.13	4.15	4.52	1.09	microporosity5
29	0.92	2.60	0.11	0.08	6.05	6.72	1.11	microporosity6
30	0.89	2.02	0.19	0.13	3.87	4.50	1.16	microporosity6
31	0.94	1.77	0.12	0.11	3.77	3.87	1.03	microporosity7
32	0.88	1.87	0.22	0.14	3.35	4.06	1.21	microporosity7

CO_2 Liquid-Saturated Frame Flexibility Factors								
Sample	**Φk**	**Fk**	**Frame stiffness (f)**	**Frame stiffness (fμ)**	**Frame flexibility (γ)**	**Frame flexibility (γμ)**	**Ratio of (γμ/γ)**	**Pore type**
33	0.93	1.76	0.13	0.13	3.67	3.66	1.00	microporosity8
34	0.87	1.86	0.23	0.15	3.31	4.00	1.21	microporosity8
35	0.93	1.92	0.13	0.10	4.04	4.52	1.12	microporosity9
36	0.90	1.91	0.18	0.13	3.66	4.27	1.17	microporosity9
37	0.55	1.72	0.66	0.47	2.07	2.95	1.42	moldic1
38	0.64	1.72	0.57	0.46	2.21	2.70	1.22	moldic1
39	0.79	1.77	0.38	0.33	2.66	2.87	1.08	moldic2
40	0.65	1.67	0.57	0.57	2.14	2.14	1.00	moldic2
41	0.79	1.78	0.37	0.34	2.68	2.84	1.06	moldic3
42	0.79	1.84	0.36	0.31	2.79	3.08	1.10	moldic3
43	0.75	1.87	0.42	0.40	2.71	2.77	1.02	moldic4
44	0.71	1.93	0.45	0.35	2.72	3.27	1.20	moldic4
45	0.73	1.98	0.42	0.35	2.88	3.24	1.12	moldic5
46	0.61	1.53	0.65	0.44	1.85	2.63	1.42	moldic5

APPENDIX G

Table shows newly calculated elastic properties with pore types identified for waterflooded rocks. Samples used for seismic monitoring were selected.

Water-saturated								
Sample	**Porosity (%)**	**Vp (m/s)**	**Vs (m/s)**	**K (GPa)**	**μ (GPa)**	**Z ((m/s)*(g/cc))**	**Density (g/cc)**	**Pore type**
1	14	5818	2930	56.006	21.462	14545	2.5	cement1
2	8	6200	3300	62.048	28.249	16083	2.60	cement1
3	14	5953	3187	54.739	25.392	14883	2.5	cement2
4	14	5953	3187	56.929	26.408	15478	2.6	cement2
5	10	5775	3208	52.009	27.278	15304	2.65	cement3
6	10	5775	3208	52.009	27.278	15304	2.65	cement3
7	48.2	2670	1700	6.289	5.549	5126	1.92	intercrystalline1
8	46	2900	1400	11.535	3.900	5771	1.99	intercrystalline1
9	48.2	2610	1300	8.753	3.245	5011	1.92	intercrystalline2
10	47	3000	1364	12.973	3.702	5970	1.99	intercrystalline2
11	40	2450	1220	8.237	3.051	5023	2.05	Intercrystalline3
12	40	2900	1408	11.420	3.924	5742	1.98	Intercrystalline3
13	42	3645	1695	18.718	5.691	7217	1.98	Intercrystalline4
14	42	3100	1500	13.418	4.5675	6293	2.03	Intercrystalline4
15	46	2000	1000	5.200	1.950	3900	1.95	microporosity1
16	44	2100	942	6.391	1.756	4158	1.98	microporosity1
17	50	2000	1000	5.067	1.900	3800	1.9	microporosity10
18	38	2100	942	6.713	1.845	4368	2.08	microporosity10
19	50	2010	1050	4.883	2.095	3819	1.90	microporosity11
20	45	2100	950	6.253	1.760	4095	1.95	microporosity11
21	46	2100	971	6.149	1.838	4095	1.95	microporosity2
22	43	2100	950	6.445	1.814	4221	2.01	microporosity2
23	46	2475	1289	7.820	3.323	4950	2.00	microporosity3
24	44	2200	1050	6.706	2.194	4378	1.99	microporosity3
25	46	2200	1146	6.117	2.600	4356	1.98	microporosity4
26	44	2219	1077	6.686	2.297	4394	1.98	microporosity4
27	35.5	2000	935	6.010	1.852	4240	2.12	microporosity5
28	44	2289	1099	7.186	2.391	4532	1.98	microporosity5
29	35.5	2000	910	6.139	1.756	4240	2.12	microporosity6
30	44	2310	1137	7.189	2.573	4597	1.99	microporosity6
31	53	2000	990	4.955	1.803	3680	1.84	microporosity7
32	47	2390	1178	7.608	2.734	4708	1.97	microporosity7
33	53	2100	1055	5.384	2.048	3864	1.84	microporosity8

Water-saturated								
Sample	**Porosity (%)**	**Vp (m/s)**	**Vs (m/s)**	**K (GPa)**	**μ (GPa)**	**Z ((m/s)*(g/cc))**	**Density (g/cc)**	**Pore type**
34	47	2515	1154	8.965	2.622	4955	1.97	microporosity8
35	48.3	2100	950	6.157	1.733	4032	1.92	microporosity9
36	47	2400	1079	8.037	2.224	4584	1.91	microporosity9
37	32	4755	2186	34.913	10.274	10223	2.15	moldic1
38	37	4334	2121	26.594	9.357	9015	2.08	moldic1
39	44.5	3692	1871	17.479	6.826	7199	1.95	moldic2
40	39	4436	2323	26.838	11.602	9537	2.15	moldic2
41	44.5	3692	1871	17.927	7.001	7384	2.00	moldic3
42	43	3459	1704	16.187	5.807	6918	2.00	moldic3
43	40	4110	2163	23.226	10.199	8960	2.18	moldic4
44	37	3900	1850	22.252	7.153	8151	2.09	moldic4
45	37	3750	1849	20.434	7.350	8063	2.15	moldic5
46	40	4373	1987	30.490	8.686	9621	2.20	moldic5

APPENDIX H

Table shows newly calculated elastic properties with pore types identified for oil-saturated rocks. Samples used for seismic monitoring were selected.

Oil-saturated								
Sample	**Porosity (%)**	**Vp (m/s)**	**Vs (m/s)**	**K (GPa)**	**μ (GPa)**	**Z ((m/s)*(g/cc))**	**Density (g/cc)**	**Pore type**
1	14	5848	3089	56.891	21.462	13150.99	2.249	cement1
2	8	6214	3385	62.506	28.249	15318.52	2.465	cement1
3	14	5986	3360	55.731	25.392	13461.10	2.249	cement2
4	14	5979	3427	57.738	26.408	13445.08	2.249	cement2
5	10	5830	3385	53.716	27.278	13879.38	2.380	cement3
6	10	5830	3385	53.716	27.278	13879.38	2.380	cement3
7	48.2	2947	2177	9.273	5.549	3450.27	1.171	intercrystalline1
8	46	3107	1780	14.004	3.900	3826.23	1.232	intercrystalline1
9	48.2	2875	1661	11.542	3.245	3381.77	1.176	intercrystalline2
10	47	3198	1765	15.419	3.702	3801.92	1.189	intercrystalline2
11	40	2774	1432	11.703	3.051	4127.04	1.488	Intercrystalline3
12	40	3161	1644	14.548	3.924	4587.40	1.451	Intercrystalline3
13	42	3819	2003	21.287	5.691	5418.22	1.419	Intercrystalline4
14	42	3317	1817	16.250	4.568	4589.55	1.384	Intercrystalline4
15	46	2369	1278	8.343	1.950	2828.99	1.194	microporosity1
16	44	2428	1149	9.331	1.756	3228.32	1.330	microporosity1
17	50	2353	1329	7.988	1.900	2532.44	1.076	microporosity10
18	38	2480	1123	10.338	1.845	3628.06	1.463	microporosity10
19	50	2361	1398	7.802	2.095	2530.02	1.071	microporosity11
20	45	2451	1195	9.368	1.760	3019.59	1.232	microporosity11
21	46	2445	1240	9.211	1.838	2920.42	1.194	microporosity2
22	43	2455	1177	9.698	1.814	3213.29	1.309	microporosity2
23	46	2754	1668	10.742	3.323	3289.38	1.194	microporosity3
24	44	2533	1314	9.841	2.194	3217.11	1.270	microporosity3
25	46	2525	1464	9.161	2.600	3064.99	1.214	microporosity4
26	44	2552	1350	9.834	2.297	3216.09	1.260	microporosity4
27	35.5	2419	1091	9.937	1.852	3766.29	1.557	microporosity5
28	44	2606	1370	10.253	2.391	3317.53	1.273	microporosity5
29	35.5	2418	1062	10.052	1.756	3764.17	1.557	microporosity6
30	44	2611	1402	10.132	2.573	3414.45	1.308	microporosity6
31	53	2345	1360	7.714	1.803	2288.07	0.976	microporosity7
32	47	2660	1497	10.295	2.734	3245.72	1.220	microporosity7
33	53	2428	1455	8.118	2.048	2348.61	0.967	microporosity8

Oil-saturated								
Sample	**Porosity (%)**	**Vp (m/s)**	**Vs (m/s)**	**K (GPa)**	**µ (GPa)**	**Z ((m/s)*(g/cc))**	**Density (g/cc)**	**Pore type**
34	47	2773	1489	11.647	2.622	3279.58	1.183	microporosity8
35	48.3	2438	1236	9.101	1.733	2766.12	1.135	microporosity9
36	47	2692	1376	10.877	2.224	3162.98	1.175	microporosity9
37	32	4831	2491	36.476	10.274	7997.69	1.656	moldic1
38	37	4434	2495	28.416	9.357	6666.79	1.504	moldic1
39	44.5	3850	2305	19.798	6.826	4944.27	1.284	moldic2
40	39	4530	2838	28.648	11.602	6525.85	1.441	moldic2
41	44.5	3847	2336	20.264	7.001	4935.69	1.283	moldic3
42	43	3628	2111	18.586	5.807	4728.74	1.303	moldic3
43	40	4238	2636	25.548	10.200	6222.00	1.468	moldic4
44	37	4037	2186	24.520	7.153	6040.10	1.496	moldic4
45	37	3896	2212	22.830	7.350	5851.86	1.502	moldic5
46	40	4453	2488	32.043	8.686	6250.84	1.404	moldic5

APPENDIX I

Table shows newly calculated elastic properties with pore types identified for CO_2 gas-saturated rocks. Samples used for seismic monitoring were selected.

CO_2 Gas-saturated								
Sample	**Porosity (%)**	**Vp (m/s)**	**Vs (m/s)**	**K (GPa)**	**µ (GPa)**	**Z ((m/s)*(g/cc))**	**Density (g/cc)**	**Pore type**
1	14	5818	3035	56.019	21.462	13558.900	2.330338	cement1
2	8	6200	3354	62.055	28.249	15573.290	2.511741	cement1
3	14	5953	3301	54.753	25.392	13873.590	2.330338	cement2
4	14	5953	3366	56.940	26.408	13873.350	2.330338	cement2
5	10	5776	3344	52.034	27.278	14086.100	2.438813	cement3
6	10	5776	3344	52.034	27.278	14086.100	2.438813	cement3
7	48.2	2674	1955	6.331	5.549	3882.810	1.452033	intercrystalline1
8	46	2903	1613	11.570	3.900	4354.423	1.499981	intercrystalline1
9	48.2	2614	1492	8.792	3.245	3809.623	1.457464	intercrystalline2
10	47	3003	1591	13.008	3.702	4392.821	1.462884	intercrystalline2
11	40	2455	1331	8.285	3.051	4225.371	1.721252	Intercrystalline3
12	40	2904	1526	11.464	3.924	4892.053	1.684701	Intercrystalline3
13	42	3647	1849	18.754	5.691	6068.720	1.663815	Intercrystalline4
14	42	3103	1675	13.458	4.568	5053.404	1.628482	Intercrystalline4
15	46	2006	1155	5.244	1.950	2933.313	1.46254	microporosity1
16	44	2105	1052	6.432	1.756	3339.081	1.586277	microporosity1
17	50	2005	1179	5.107	1.900	2742.961	1.367821	microporosity10
18	38	2106	1046	6.764	1.845	3546.907	1.684318	microporosity10
19	50	2015	1240	4.924	2.095	2746.972	1.363043	microporosity11
20	45	2105	1085	6.297	1.760	3146.310	1.494459	microporosity11
21	46	2105	1121	6.192	1.838	3078.970	1.46254	microporosity2
22	43	2105	1078	6.491	1.814	3283.524	1.559577	microporosity2
23	46	2479	1507	7.861	3.323	3625.812	1.46254	microporosity3
24	44	2205	1199	6.750	2.194	3366.679	1.526832	microporosity3
25	46	2205	1324	6.160	2.600	3267.620	1.481992	microporosity4
26	44	2224	1231	6.730	2.297	3373.330	1.516777	microporosity4
27	35.5	2007	1025	6.066	1.852	3539.395	1.763922	microporosity5
28	44	2294	1250	7.229	2.391	3509.211	1.529909	microporosity5
29	35.5	2007	998	6.195	1.756	3539.352	1.763922	microporosity6
30	44	2314	1282	7.230	2.573	3621.182	1.564566	microporosity6
31	53	2005	1185	4.994	1.803	2576.355	1.284831	microporosity7
32	47	2394	1353	7.646	2.734	3577.380	1.494313	microporosity7
33	53	2105	1267	5.422	2.048	2686.649	1.276369	microporosity8

CO$_2$ Gas-saturated								
Sample	**Porosity (%)**	**Vp (m/s)**	**Vs (m/s)**	**K (GPa)**	**μ (GPa)**	**Z ((m/s)*(g/cc))**	**Density (g/cc)**	**Pore type**
34	47	2519	1341	9.002	2.622	3669.940	1.457031	microporosity8
35	48.3	2105	1106	6.198	1.733	2981.513	1.416338	microporosity9
36	47	2404	1239	8.076	2.224	3484.077	1.449091	microporosity9
37	32	4756	2362	34.935	10.274	8761.625	1.842202	moldic1
38	37	4335	2333	26.619	9.357	7454.326	1.719407	moldic1
39	44.5	3694	2103	17.511	6.826	5703.474	1.543883	moldic2
40	39	4437	2637	26.864	11.602	7401.904	1.668103	moldic2
41	44.5	3694	2130	17.959	7.001	5698.484	1.542549	moldic3
42	43	3461	1933	16.220	5.807	5379.490	1.55413	moldic3
43	40	4112	2448	23.258	10.199	6996.656	1.701604	moldic4
44	37	3902	2044	22.283	7.153	6680.541	1.712107	moldic4
45	37	3752	2068	20.467	7.350	6445.767	1.71792	moldic5
46	40	4374	2303	30.511	8.686	7160.666	1.637054	moldic5

APPENDIX J

Table shows newly calculated elastic properties with pore types identified for CO_2 liquid-saturated rocks. Samples used for seismic monitoring were selected.

CO_2 Liquid-saturated								
Sample	**Porosity (%)**	**Vp (m/s)**	**Vs (m/s)**	**K (GPa)**	**μ (GPa)**	**Z ((m/s)*(g/cc))**	**Density (g/cc)**	**Pore type**
1	14	5824	3133	56.172	21.462	12731.26	2.19	cement1
2	8	6203	3410	62.134	28.249	15068.30	2.43	cement1
3	14	5959	3408	54.925	25.392	13027.61	2.19	cement2
4	14	5958	3476	57.080	26.408	13024.64	2.19	cement2
5	10	5786	3417	52.335	27.278	13514.12	2.34	cement3
6	10	5786	3417	52.335	27.278	13514.12	2.34	cement3
7	48.2	2724	2410	6.846	5.549	2602.56	0.96	intercrystalline1
8	46	2940	1950	12.000	3.900	3016.48	1.03	intercrystalline1
9	48.2	2661	1838	9.273	3.245	2557.41	0.96	intercrystalline2
10	47	3038	1945	13.429	3.702	2973.29	0.98	intercrystalline2
11	40	2514	1527	8.886	3.051	3291.03	1.31	Intercrystalline3
12	40	2951	1756	12.006	3.924	3755.03	1.27	Intercrystalline3
13	42	3678	2150	19.197	5.691	4528.19	1.23	Intercrystalline4
14	42	3142	1954	13.947	4.568	3756.97	1.20	Intercrystalline4
15	46	2074	1404	5.788	1.950	2050.56	0.99	microporosity1
16	44	2166	1245	6.945	1.756	2453.65	1.13	microporosity1
17	50	2070	1493	5.612	1.900	1765.62	0.85	microporosity10
18	38	2177	1194	7.396	1.845	2814.25	1.29	microporosity10
19	50	2080	1572	5.428	2.095	1763.90	0.85	microporosity11
20	45	2170	1307	6.836	1.760	2237.10	1.03	microporosity11
21	46	2169	1363	6.722	1.838	2144.26	0.99	microporosity2
22	43	2171	1275	7.055	1.814	2424.20	1.12	microporosity2
23	46	2530	1833	8.366	3.323	2500.94	0.99	microporosity3
24	44	2266	1430	7.294	2.194	2432.81	1.07	microporosity3
25	46	2264	1606	6.687	2.600	2282.88	1.01	microporosity4
26	44	2285	1470	7.276	2.297	2430.27	1.06	microporosity4
27	35.5	2086	1151	6.753	1.852	2916.31	1.40	microporosity5
28	44	2352	1490	7.761	2.391	2531.83	1.08	microporosity5
29	35.5	2085	1121	6.879	1.756	2915.88	1.40	microporosity6
30	44	2369	1521	7.742	2.573	2633.13	1.11	microporosity6
31	53	2069	1562	5.470	1.803	1528.46	0.74	microporosity7
32	47	2443	1645	8.111	2.734	2467.69	1.01	microporosity7
33	53	2165	1674	5.893	2.045	1581.24	0.73	microporosity8

CO₂ Liquid-saturated								
Sample	**Porosity (%)**	**Vp (m/s)**	**Vs (m/s)**	**K (GPa)**	**μ (GPa)**	**Z ((m/s)*(g/cc))**	**Density (g/cc)**	**Pore type**
34	47	2565	1642	9.466	2.622	2495.51	0.97	microporosity8
35	48.3	2167	1373	6.706	1.733	1991.09	0.92	microporosity9
36	47	2457	1518	8.567	2.224	2371.01	0.96	microporosity9
37	32	4769	2606	35.204	10.274	7213.71	1.51	moldic1
38	37	4353	2644	26.933	9.357	5825.15	1.34	moldic1
39	44.5	3722	2508	17.910	6.826	4040.00	1.09	moldic2
40	39	4454	3027	27.175	11.602	5639.84	1.27	moldic2
41	44.5	3721	2541	18.362	7.001	4034.46	1.08	moldic3
42	43	3491	2286	16.634	5.807	3879.33	1.11	moldic3
43	40	4134	2812	23.658	10.200	5331.08	1.29	moldic4
44	37	3926	2318	22.675	7.153	5225.22	1.33	moldic4
45	37	3778	2345	20.882	7.350	5049.92	1.34	moldic5
46	40	4388	2663	30.778	8.686	5375.25	1.23	moldic5

APPENDIX K

Table shows fluid substitution values with differences in P-wave velocity and density. Impedance is the product of Vp and density. The highlighted rows are the samples that underwent fluid substitution (A to I with increasing depth).

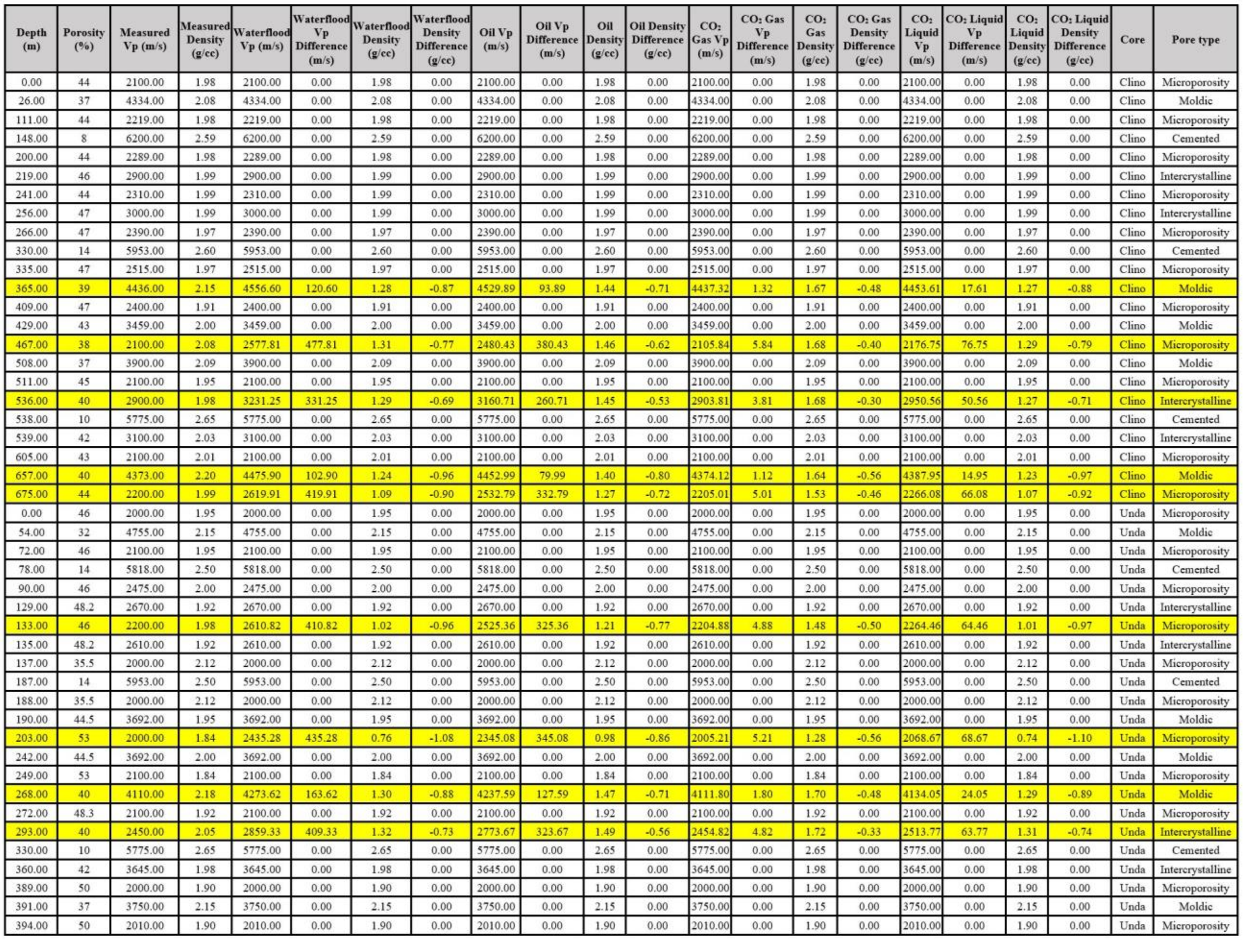

Depth (m)	Porosity (%)	Measured Vp (m/s)	Measured Density (g/cc)	Waterflood Vp (m/s)	Waterflood Vp Difference (m/s)	Waterflood Density (g/cc)	Waterflood Density Difference (g/cc)	Oil Vp (m/s)	Oil Vp Difference (m/s)	Oil Density (g/cc)	Oil Density Difference (g/cc)	CO_2 Gas Vp (m/s)	CO_2 Gas Vp Difference (m/s)	CO_2 Gas Density (g/cc)	CO_2 Gas Density Difference (g/cc)	CO_2 Liquid Vp (m/s)	CO_2 Liquid Vp Difference (m/s)	CO_2 Liquid Density (g/cc)	CO_2 Liquid Density Difference (g/cc)	Core	Pore type
0.00	44	2100.00	1.98	2100.00	0.00	1.98	0.00	2100.00	0.00	1.98	0.00	2100.00	0.00	1.98	0.00	2100.00	0.00	1.98	0.00	Clino	Microporosity
26.00	37	4334.00	2.08	4334.00	0.00	2.08	0.00	4334.00	0.00	2.08	0.00	4334.00	0.00	2.08	0.00	4334.00	0.00	2.08	0.00	Clino	Moldic
111.00	44	2219.00	1.98	2219.00	0.00	1.98	0.00	2219.00	0.00	1.98	0.00	2219.00	0.00	1.98	0.00	2219.00	0.00	1.98	0.00	Clino	Microporosity
148.00	8	6200.00	2.59	6200.00	0.00	2.59	0.00	6200.00	0.00	2.59	0.00	6200.00	0.00	2.59	0.00	6200.00	0.00	2.59	0.00	Clino	Cemented
200.00	44	2289.00	1.98	2289.00	0.00	1.98	0.00	2289.00	0.00	1.98	0.00	2289.00	0.00	1.98	0.00	2289.00	0.00	1.98	0.00	Clino	Microporosity
219.00	46	2900.00	1.99	2900.00	0.00	1.99	0.00	2900.00	0.00	1.99	0.00	2900.00	0.00	1.99	0.00	2900.00	0.00	1.99	0.00	Clino	Intercrystalline
241.00	44	2310.00	1.99	2310.00	0.00	1.99	0.00	2310.00	0.00	1.99	0.00	2310.00	0.00	1.99	0.00	2310.00	0.00	1.99	0.00	Clino	Microporosity
256.00	47	3000.00	1.99	3000.00	0.00	1.99	0.00	3000.00	0.00	1.99	0.00	3000.00	0.00	1.99	0.00	3000.00	0.00	1.99	0.00	Clino	Intercrystalline
266.00	47	2390.00	1.97	2390.00	0.00	1.97	0.00	2390.00	0.00	1.97	0.00	2390.00	0.00	1.97	0.00	2390.00	0.00	1.97	0.00	Clino	Microporosity
330.00	14	5953.00	2.60	5953.00	0.00	2.60	0.00	5953.00	0.00	2.60	0.00	5953.00	0.00	2.60	0.00	5953.00	0.00	2.60	0.00	Clino	Cemented
335.00	47	2515.00	1.97	2515.00	0.00	1.97	0.00	2515.00	0.00	1.97	0.00	2515.00	0.00	1.97	0.00	2515.00	0.00	1.97	0.00	Clino	Microporosity
365.00	39	4436.00	2.15	4556.60	120.60	1.28	-0.87	4529.89	93.89	1.44	-0.71	4437.32	1.32	1.67	-0.48	4453.61	17.61	1.27	-0.88	Clino	Moldic
409.00	47	2400.00	1.91	2400.00	0.00	1.91	0.00	2400.00	0.00	1.91	0.00	2400.00	0.00	1.91	0.00	2400.00	0.00	1.91	0.00	Clino	Microporosity
429.00	43	3459.00	2.00	3459.00	0.00	2.00	0.00	3459.00	0.00	2.00	0.00	3459.00	0.00	2.00	0.00	3459.00	0.00	2.00	0.00	Clino	Moldic
467.00	38	2100.00	2.08	2577.81	477.81	1.31	-0.77	2480.43	380.43	1.46	-0.62	2105.84	5.84	1.68	-0.40	2176.75	76.75	1.29	-0.79	Clino	Microporosity
508.00	37	3900.00	2.09	3900.00	0.00	2.09	0.00	3900.00	0.00	2.09	0.00	3900.00	0.00	2.09	0.00	3900.00	0.00	2.09	0.00	Clino	Moldic
511.00	45	2100.00	1.95	2100.00	0.00	1.95	0.00	2100.00	0.00	1.95	0.00	2100.00	0.00	1.95	0.00	2100.00	0.00	1.95	0.00	Clino	Microporosity
536.00	40	2900.00	1.98	3231.25	331.25	1.29	-0.69	3160.71	260.71	1.45	-0.53	2903.81	3.81	1.68	-0.30	2950.56	50.56	1.27	-0.71	Clino	Intercrystalline
538.00	10	5775.00	2.65	5775.00	0.00	2.65	0.00	5775.00	0.00	2.65	0.00	5775.00	0.00	2.65	0.00	5775.00	0.00	2.65	0.00	Clino	Cemented
539.00	42	3100.00	2.03	3100.00	0.00	2.03	0.00	3100.00	0.00	2.03	0.00	3100.00	0.00	2.03	0.00	3100.00	0.00	2.03	0.00	Clino	Intercrystalline
605.00	43	2100.00	2.01	2100.00	0.00	2.01	0.00	2100.00	0.00	2.01	0.00	2100.00	0.00	2.01	0.00	2100.00	0.00	2.01	0.00	Clino	Microporosity
657.00	40	4373.00	2.20	4475.90	102.90	1.24	-0.96	4452.99	79.99	1.40	-0.80	4374.12	1.12	1.64	-0.56	4387.95	14.95	1.23	-0.97	Clino	Moldic
675.00	44	2200.00	1.99	2619.91	419.91	1.09	-0.90	2532.79	332.79	1.27	-0.72	2205.01	5.01	1.53	-0.46	2266.08	66.08	1.07	-0.92	Clino	Microporosity
0.00	46	2000.00	1.95	2000.00	0.00	1.95	0.00	2000.00	0.00	1.95	0.00	2000.00	0.00	1.95	0.00	2000.00	0.00	1.95	0.00	Unda	Microporosity
54.00	32	4755.00	2.15	4755.00	0.00	2.15	0.00	4755.00	0.00	2.15	0.00	4755.00	0.00	2.15	0.00	4755.00	0.00	2.15	0.00	Unda	Moldic
72.00	46	2100.00	1.95	2100.00	0.00	1.95	0.00	2100.00	0.00	1.95	0.00	2100.00	0.00	1.95	0.00	2100.00	0.00	1.95	0.00	Unda	Microporosity
78.00	14	5818.00	2.50	5818.00	0.00	2.50	0.00	5818.00	0.00	2.50	0.00	5818.00	0.00	2.50	0.00	5818.00	0.00	2.50	0.00	Unda	Cemented
90.00	46	2475.00	2.00	2475.00	0.00	2.00	0.00	2475.00	0.00	2.00	0.00	2475.00	0.00	2.00	0.00	2475.00	0.00	2.00	0.00	Unda	Microporosity
129.00	48.2	2670.00	1.92	2670.00	0.00	1.92	0.00	2670.00	0.00	1.92	0.00	2670.00	0.00	1.92	0.00	2670.00	0.00	1.92	0.00	Unda	Intercrystalline
133.00	46	2200.00	1.98	2610.82	410.82	1.02	-0.96	2525.36	325.36	1.21	-0.77	2204.88	4.88	1.48	-0.50	2264.46	64.46	1.01	-0.97	Unda	Microporosity
135.00	48.2	2610.00	1.92	2610.00	0.00	1.92	0.00	2610.00	0.00	1.92	0.00	2610.00	0.00	1.92	0.00	2610.00	0.00	1.92	0.00	Unda	Intercrystalline
137.00	35.5	2000.00	2.12	2000.00	0.00	2.12	0.00	2000.00	0.00	2.12	0.00	2000.00	0.00	2.12	0.00	2000.00	0.00	2.12	0.00	Unda	Microporosity
187.00	14	5953.00	2.50	5953.00	0.00	2.50	0.00	5953.00	0.00	2.50	0.00	5953.00	0.00	2.50	0.00	5953.00	0.00	2.50	0.00	Unda	Cemented
188.00	35.5	2000.00	2.12	2000.00	0.00	2.12	0.00	2000.00	0.00	2.12	0.00	2000.00	0.00	2.12	0.00	2000.00	0.00	2.12	0.00	Unda	Microporosity
190.00	44.5	3692.00	1.95	3692.00	0.00	1.95	0.00	3692.00	0.00	1.95	0.00	3692.00	0.00	1.95	0.00	3692.00	0.00	1.95	0.00	Unda	Moldic
203.00	53	2000.00	1.84	2435.28	435.28	0.76	-1.08	2345.08	345.08	0.98	-0.86	2005.21	5.21	1.28	-0.56	2068.67	68.67	0.74	-1.10	Unda	Microporosity
242.00	44.5	3692.00	2.00	3692.00	0.00	2.00	0.00	3692.00	0.00	2.00	0.00	3692.00	0.00	2.00	0.00	3692.00	0.00	2.00	0.00	Unda	Moldic
249.00	53	2100.00	1.84	2100.00	0.00	1.84	0.00	2100.00	0.00	1.84	0.00	2100.00	0.00	1.84	0.00	2100.00	0.00	1.84	0.00	Unda	Microporosity
268.00	40	4110.00	2.18	4273.62	163.62	1.30	-0.88	4237.59	127.59	1.47	-0.71	4111.80	1.80	1.70	-0.48	4134.05	24.05	1.29	-0.89	Unda	Moldic
272.00	48.3	2100.00	1.92	2100.00	0.00	1.92	0.00	2100.00	0.00	1.92	0.00	2100.00	0.00	1.92	0.00	2100.00	0.00	1.92	0.00	Unda	Microporosity
293.00	40	2450.00	2.05	2859.33	409.33	1.32	-0.73	2773.67	323.67	1.49	-0.56	2454.82	4.82	1.72	-0.33	2513.77	63.77	1.31	-0.74	Unda	Intercrystalline
330.00	10	5775.00	2.65	5775.00	0.00	2.65	0.00	5775.00	0.00	2.65	0.00	5775.00	0.00	2.65	0.00	5775.00	0.00	2.65	0.00	Unda	Cemented
360.00	42	3645.00	1.98	3645.00	0.00	1.98	0.00	3645.00	0.00	1.98	0.00	3645.00	0.00	1.98	0.00	3645.00	0.00	1.98	0.00	Unda	Intercrystalline
389.00	50	2000.00	1.90	2000.00	0.00	1.90	0.00	2000.00	0.00	1.90	0.00	2000.00	0.00	1.90	0.00	2000.00	0.00	1.90	0.00	Unda	Microporosity
391.00	37	3750.00	2.15	3750.00	0.00	2.15	0.00	3750.00	0.00	2.15	0.00	3750.00	0.00	2.15	0.00	3750.00	0.00	2.15	0.00	Unda	Moldic
394.00	50	2010.00	1.90	2010.00	0.00	1.90	0.00	2010.00	0.00	1.90	0.00	2010.00	0.00	1.90	0.00	2010.00	0.00	1.90	0.00	Unda	Microporosity